

UTILIZATION OF $(\text{La}_{1-x}\text{Sr}_x)\text{CoO}_{3-\delta}/(\text{La}_{1-y}\text{Sr}_y)_2\text{CoO}_{4\pm\delta}$ HETEROSTRUCTURES
AS CATHODE FOR IT-SOFCs

A THESIS SUBMITTED TO
THE GRADUATE SCHOOL OF NATURAL AND APPLIED SCIENCES
OF
MIDDLE EAST TECHNICAL UNIVERSITY

BY

ZİYA ÇAĞRI TORUNOĞLU

IN PARTIAL FULFILLMENT OF THE REQUIREMENTS
FOR
THE DEGREE OF MASTER OF SCIENCE
IN
METALLURGICAL AND MATERIALS ENGINEERING

JUNE 2017

Approval of the thesis:

**UTILIZATION OF $(La_{1-x}Sr_x)CoO_{3-\delta}/(La_{1-y}Sr_y)_2CoO_{4+\delta}$
HETEROSTRUCTURES AS CATHODE FOR IT-SOFCs**

Submitted by **ZİYA ÇAĞRI TORUNOĞLU** in partial fulfillment of the requirements for the degree of **Master of Science in Metallurgical and Materials Engineering Department, Middle East Technical University** by,

Prof. Dr. Gülbin Dural Ünver _____
Dean, Graduate School of **Natural and Applied Sciences**

Prof. Dr. Cemil Hakan Gür _____
Head of Department, **Metallurgical and Materials Eng., METU**

Assoc. Prof. Dr. Yener Kuru _____ DECEASED _____
Supervisor, **Metallurgical and Materials Eng. Dept., METU**

Prof. Dr. Tayfur Öztürk _____
Acting Supervisor, **Metallurgical and Materials Eng., METU**

Assoc. Prof. Dr. Yunus Eren Kalay _____
Co-Supervisor, **Metallurgical and Materials Eng. Dept., METU**

Examining Committee Members:

Prof. Dr. Mehmet Kadri Aydınol _____
Metallurgical and Materials Eng. Dept., METU

Prof. Dr. Tayfur Öztürk _____
Metallurgical and Materials Eng. Dept., METU

Prof. Dr. İnci Eroğlu _____
Chemical Engineering. Dept., METU

Assoc. Prof. Dr. Yunus Eren Kalay _____
Metallurgical and Materials Eng. Dept., METU

Assist. Prof. Dr. Gülhan Çakmak _____
Metallurgical and Materials Eng., Muğla Sıtkı Koçman University

Date: 23.06.2017

I hereby declare that all information in this document has been obtained and presented in accordance with academic rules and ethical conduct. I also declare that, as required by these rules and conduct, I have fully cited and referenced all material and results that are not original to this work.

Name, Last Name : Ziya Çađrı Torunođlu

Signature :

ABSTRACT

UTILIZATION OF $(La_{1-x}Sr_x)CoO_{3-\delta}/(La_{1-y}Sr_y)_2CoO_{4\pm\delta}$ HETEROSTRUCTURES AS CATHODE FOR IT-SOFCs

Torunoğlu, Ziya Çağrı
M.Sc., Department of Metallurgical and Materials Engineering
Supervisor: Prof. Dr. Tayfur Öztürk
Co-Supervisor: Assoc. Prof. Dr. Y. Eren Kalay

June 2017, 151 pages

Perovskite type ABO_3 oxides have been studied as one of the promising candidates for the cathode of intermediate temperature (500-700 °C) solid oxide fuel cells (SOFCs). The one of the best one among them is $(La_{1-x}Sr_x)CoO_{3-\delta}$ (LSC_{113}) in terms of SOFC cathode performance. However, LSC drastically suffers from strong chemical instability problem manifested as surface Strontium segregation, triggered by increasing operation temperature. Lowering temperature, on the other hand, blocks oxygen reduction performance of cathode, constituting a contradiction.

Recently, a thousand times greater oxygen reduction reaction coefficient, k (cm/s), around the $(La_{1-x}Sr_x)CoO_{3-\delta}/(La_{1-y}Sr_y)_2CoO_{4\pm\delta}$ interface than LSC_{113} has been reported in recent years. This hetero-interface can decrease operation temperature of SOFC cathode to reasonable levels by facilitating oxygen reduction. The aim of this study is to utilize this hetero-interface for cathode by integrating different interface construction approaches and examine their results in terms of their compatibility at desired low temperatures. Simultaneous-sputtering of $(La_{1-x}Sr_x)CoO_{3-\delta}$ and $(La_{1-$

$y\text{Sr}_y)_2\text{CoO}_{4\pm\delta}$ as thin film cathode and dual phase synthesis from one solution as route-oriented conventional thick cathode has been adopted as the progressive ways to maximize interfaces, the former of which yielded positive results in terms of increasing hetero-interface and reducing cathode resistance. On the other hand, although dual phase syntheses of powders were successful, were not composed of agglomerates of two phases and did result in finely dispersed nano-particles, it yet resulted in poor performance improvement and temperature reduction in form of conventional thick film cathode application.

Keywords: SOFC cathode, $\text{LSC}_{113}/\text{LSC}_{214}$ hetero interface, one-pot synthesis, magnetron co-sputtering, in situ EIS

ÖZ

ORTA SICAKLIK KATI OKSİT YAKIT PİLLERİ İÇİN (La_{1-x}Sr_x)CoO_{3-δ}/(La_{1-y}Sr_y)₂CoO_{4±δ} ÇOKLU YAPILARIN KATOT OLARAK KULLANIMI

Torunoğlu, Ziya Çağrı
Yüksek Lisans, Metalurji ve Malzeme Mühendisliği Bölümü
Tez Yöneticisi: Prof. Dr. Tayfur Öztürk
Ortak Tez Yöneticisi: Doç. Dr. Y. Eren Kalay

Haziran 2017, 151 sayfa

Perovskit tipi ABO₃ oksitleri orta sıcaklık (500-700 °C) katı oksit yakıt pilleri (KOYP) katotları için gelecek vaat eden adaylardan biri olarak çalışılmaktadır. (La_{1-x}Sr_x)CoO_{3-δ} (LSC₁₁₃) bileşiği, bu oksitler arasında KOYP katot performansı bakımından en iyilerinden biridir. Ancak LSC₁₁₃ artan çalışma sıcaklığı tarafından tetiklenen yüzeye Sr ayrışması olarak zuhur eden yüksek kimyasal kararsızlıktan muzdariptir. Öte yandan çalışma sıcaklığını düşürmek katodun oksijen indirgenme performansını azaltır ve bir çelişki teşkil eder.

Son yıllarda (La_{1-x}Sr_x)CoO_{3-δ}/(La_{1-y}Sr_y)₂CoO_{4±δ} çoklu arayüzü çevresinde LSC₁₁₃'ten bin kat yüksek bir oksijen indirgenme tepkime sabiti, k (cm/s) rapor edilmiştir. Bu çoklu arayüz oksijen indirgenme kinetiğini arttırarak KOYP çalışma sıcaklığını makul düzeylere düşürebilir. Bu çalışmanın amacı farklı arayüz inşa yaklaşımlarını benimseyip bu çoklu arayüzden istifade etmek ve istenen düşük sıcaklıktaki uyumluluğunu incelemektir. İnce film katot olarak (La_{1-x}Sr_x)CoO_{3-δ} ve (La_{1-y}Sr_y)₂CoO_{4±δ} fazlarının eş zamanlı sıçratma çöktürmesi ve üretim odaklı olarak tek bir

çözeltiden iki fazlı yapının sentezi, çoklu arayüzün azamileştirilmesinin yenilikçi yöntemleri olarak benimsenmiştir. Bunlardan ilki çoklu arayüzü arttırmak ve katot direncini düşürmek bakımından müspet sonuçlar vermiştir. Öte yandan çift faz sentezleri, her ne kadar başarılı olmuş, iki fazın büyük topaklarından oluşmamış ve nano parçaların ince ölçekte dağılımı sonucunu vermişse de, bunlar beraber tozların geleneksel kalın film katot biçimindeki uygulaması zayıf bir performans artışı ve sıcaklık düşüşüyle sonuçlanmıştır.

Anahtar Kelimeler: KOYP katodu, LSC_{113}/LSC_{214} çoklu arayüz, tek pota sentezi, eş zamanlı sıçratma çöktürme, yerinde EIS

In Memory of Yener Kuru

PREFACE

This work has been conducted under extraordinarily unfortunate conditions leading that considerable portion of our faculty members had contributions from giving helpful discussions to supplementing lab equipment. Hence, this study owes appreciations, making this preface longer than customary ones.

Prior to my appreciations, I must highlight that I wanted this thesis to constitute a review for reader since this thesis is the first solid oxide fuel cell study in my department and I wish this study to ease things more or less for new researchers. Furthermore, this study is based on more efficient use of existing energy sources. I know that the fundamental problem making energy so crucial is organized but unplanned, irrational production favored by capitalism. I hope our days in which productive activity of mankind will be rational and planned are close.

During my studies, my advisor Assoc. Prof. Dr. Yener Kuru was deceased on 03.04.2016. I have so many things to tell about him. But I am forced to briefly say that he had always been a special and distinguished researcher having an appreciable insight. He was keen on essence rather, not in appearance in our degenerated age in which everything is judged and evaluated more or less with its appearance and/or form regardless of what fills it. He never evaluated me (and his other students) with formal so-called suitability parameters in this sense. When I was senior in undergraduate, he opened the research path for me. I can definitely state that any other faculty member in my department would never insist on me like him to direct me to research path. I will miss him.

Work reported in this thesis was carried out in conjunction with “Interface Engineering in Metal Hydride Coupled Solid Oxide Fuel Cell”, a part of an ERAfrica Project, supported by TÜBİTAK with project number 114M128. Due to their great support during this project both mentally and intellectually, I am very grateful to my supervisors Prof. Dr. Tayfur Öztürk and Assoc. Prof. Dr. Yunus Eren Kalay.

In an extremely critical time interval in which I must learn and conduct a part of my experiments, Assist. Prof. Dr. Oktay Demircan, who has significant contribution to impedance experiments, did lead me. Likewise, I am grateful to Prof. Dr. Meltem Asiltürk not only because of her academic assistance but also her sincere friendship. During my research, I earned noticeable vision thanks to Prof. Dr. Mehmet Kadri Aydınol and Prof. Dr. Tarık Ömer Oğurtanı.

Mehmet Hazar Şeren was my only laboratory colleague during this period. In the absence of our advisor, we helped and supported each other, making us more than two laboratory colleagues. I will remember that. I also owe an appreciation to my project colleague Doğancan Sarı, thanks to whom and with his supports, aim in this project has been achieved. I was also lucky in this period thanks to existence of my friends İbrahim Yıldırım, Yunus Özdener, Mete Batuhan Durukan and Mustafacan Kutsal. A good start up has always been a great luck; I am grateful to my unique teachers from Açılım Dershanesi.

These unfortunate years of my research now are identified with my prospective wife Gizem Ucuz and my dearest, my mother Sabiha Torunoğlu. They are my mind, my eyes, and my feels. They are my fortune.

Goethe says in Faust that “human being knows her/himself only at human being”. All those people are more or less the ones by whom I figure out myself.

TABLE OF CONTENTS

ABSTRACT.....	v
ÖZ.....	vii
PREFACE.....	x
LIST OF TABLES.....	xv
LIST OF FIGURES.....	xvii
NOMENCLATURE.....	xxi
CHAPTERS	
1-INTRODUCTION.....	1
2-OVERVIEW TO SOFC CATHODES.....	5
2.1. Solid Oxide Fuel Cells.....	5
2.1.1. SOFC Operation.....	6
2.1.1.1. Anode Requirements.....	9
2.1.1.2. Electrolyte Requirements.....	10
2.1.1.3. Cathode Requirements.....	11
2.2. MIEC Perovskites.....	12
2.2.1. Structural Stability.....	20
2.2.2. Chemical Stability.....	21
2.2.2.1. Surface Strontium Segregation.....	23
2.2.3. Coefficient of Thermal Expansion.....	25
2.3. An Overview to State-of-The Art Cathodes.....	28
2.3.1. $(La_{1-x}Sr_x)MnO_{3\pm\delta}$ (LSM).....	28
2.3.2. $(La_{1-x}Sr_x)CoO_{3-\delta}$ (LSC).....	30
2.3.3. $(La_{1-x}Sr_x)FeO_{3-\delta}$ (LSF).....	35
2.3.4. $(La_{1-x}Sr_x)(Co_{1-y}Fe_y)O_{3-\delta}$ (LSCF).....	36
2.3.5. $(Ba_{1-x}Sr_x)(Co_{1-y}Fe_y)O_{3-\delta}$ (BSCF).....	38
2.3.6. Ruddlesden-Popper (A_2BO_4) Type LSC_{214}	40

2.3.7. Final Remarks Regarding State-of-The Art Cathodes.....	42
2.4. LSC ₁₁₃ /LSC ₂₁₄ Hetero Interface	43
2.5. Motivation of The Work.....	50
3-IN SITU ELECTROCHEMICAL IMPEDANCE ANALYSIS	53
3.1. <i>In situ</i> Electrochemical Impedance Spectroscopy.....	53
3.2. Considerations Regarding Solid State Analysis	55
4-SYNTHESIS AND PERFORMANCE OF THICK LSC CATHODES	61
4.1. Synthesis of Powders.....	61
4.1.1. Synthesis of Single Phase LSC ₁₁₃ and LSC ₂₁₄	63
4.1.2. In situ EIS Analysis of Porous Cathodes of Physical Mixture	68
4.1.2.1. Symmetric Cell Preparation via Powders	68
4.1.2.2. Electrolyte Synthesis and Fabrication.....	69
4.1.2.3. Slurry Preparation	71
4.1.2.4. Cell Fabrication.....	72
4.1.2.5. EIS Measurements	72
4.2. One Pot Synthesis of Dual Phase of (La _{1-x} Sr _x)CoO ₃ /(La _{1-y} Sr _y) ₂ CoO ₄	75
4.2.1. Rietveld Refinement Evaluation of Dual Phase Powders.....	77
4.2.2. In Situ EIS Cell Responses	87
4.3. Conclusions	108
5-FABRICATION AND PERFORMANCE OF THIN FILM LSC CATHODES .	109
5.1. Introduction	109
5.2. Preparation of Oxide Sputtering Targets.....	109
5.3. Fabrication of LSC Cathodes via Magnetron Co-Sputtering	110
5.3.1. Fabrication of Symmetric Cell with Thin Film Cathode	110
5.4. In situ Electrochemical Impedance Analysis	111
5.4.1. EIS Responses of Cell-10% LSC ₁₁₃	112
5.4.2. EIS Responses of Cell-25% LSC ₁₁₃	118
5.4.3. Stability of Cathodes.....	124
5.5. Comparative Evaluation of EIS responses	125
5.6. Conclusions	130
6-CONCLUSIONS	131

REFERENCES 135

LIST OF TABLES

TABLES

Table 2-1 An overview to CTE of cobaltite, ferrite and manganite cathodes of SOFC	26
Table 2-2 An overview to CTE of state-of-the art electrolyte materials for SOFC ..	26
Table 2-3 Ionic radii of Co^{+3} , Mn^{+3} and Fe^{+3} at different spin states [98]	32
Table 2-4 CTE, electrical and ionic conductivities of various LSCF cathodes	36
Table 4-1 Precursors stoichiometry calculation for $\text{La}_{0.8}\text{Sr}_{0.2}\text{CoO}_3$ powder	63
Table 4-2 Rietveld refinement results for standard Silicon powder sample	65
Table 4-3 XRD analysis results of single phase $(\text{La}_{0.8}\text{Sr}_{0.2})\text{CoO}_{3-\delta}$ and $\text{LaSrCoO}_{4+\delta}$ powders	67
Table 4-4 XRD analysis results of $(\text{Ce}_{0.9}\text{Gd}_{0.1})\text{O}_{2-\delta}$ powders	69
Table 4-5 Chemicals used to prepare cathode slurry	71
Table 4-6 Abbreviations of solutions and corresponding phase fraction expectations	76
Table 4-7 Stoichiometric calculation for precursors of DP-3 powders as an instance	77
Table 4-8 Lattice parameters of phases with accompanying fitting parameters	81
Table 4-9 Weight and phase fractions of phases in each dual phase synthesis	85
Table 4-10 Refined cation stoichiometry of phases	85
Table 4-11 $n_{\text{La}}/n_{\text{Sr}}$ ratio in beaker used as reference for checksum of site occupancies set	86
Table 5-1 Calculated area specific resistances of cell-10% LSC_{113} and its electrolyte in the light of equivalent circuit models	117
Table 5-2 Calculated area specific resistances of cell-25% LSC_{113} and its electrolyte in the light of equivalent circuit models	121
Table 5-3 Critical utilization length (l_δ) of $(\text{La}_{0.8}\text{Sr}_{0.2})\text{CoO}_3$ at different temperatures [43]	123

Table 5-4 Modified Arrhenius equations derived from data, corresponding slopes, activation energies and goodness of fit depicted as R^2 127

LIST OF FIGURES

FIGURES

Figure 2-1 SOFC Operation	7
Figure 2-2 ASR as a function of temperature for a SOFC consisting LSM as cathode, YSZ as electrolyte and Ni-YSZ as anode and operating with hydrogen as fuel [30].....	8
Figure 2-3 Temperature-thickness-conductivity diagram for state-of-the art electrolytes [14]	10
Figure 2-4 Perovskite Structure showing atom/vacancy coordination (left) and path for oxygen ionic transport (right) [52]	13
Figure 2-5 Intrinsic and extrinsic intervals in substituted ionic crystals.....	16
Figure 2-6 Paths regarding the types of SOFC cathode [52]	19
Figure 2-7 Drastic ASR change as a function of time at different temperatures. Green represents stoichiometric bulk LSC, orange denotes Sr enriched regions and red boxes symbolize segregated and separated SrO-rich phase [18]	24
Figure 2-8 Cross sectional image of Siemens/Westinghouse SOFC in which LSM is used as cathode (air electrode) [3]	29
Figure 2-9 Illustration of Co-O-Co bond angle change effects on electronic structure (adapted from [103])	31
Figure 2-10 ASR of LSC in different studies (retrieved from [14,122])	34
Figure 2-11 ASR values of various LSCF dense thin films. Figure is retrieved from ref [134]. Data in the box is from ref [134] . Data from Baumann et al. [133] and Xiong et al. [135]	37
Figure 2-12 Ruddlesden-Popper (K_2NiF_4 type) LSC_{214} Structure [21]	40
Figure 2-13 FIB milling at grazing incidence angle [169].....	45
Figure 2-14 Illustration of proposed ORR mechanism for LSC_{113}/LSC_{214} by Chen et al. [169].....	46
Figure 3-1 $ Z $ corresponds to certain value of impedance at unique perturbation frequency [172].....	54

Figure 3-2 Nyquist Plot of Fe doped SrTiO ₃ and corresponding equivalent circuit [173].....	54
Figure 3-3 Dense thin film cathode where L represents critical utilization length (adapted from [178]).....	56
Figure 3-4 Resultant proposed impedance response from cathode having $L > 3l_{\delta}$ according to S. B. Adler [180,182].....	58
Figure 3-5 Impedance spectra for 70 μm thick LSC ₂₁₄ cathode at 650 °C and 0.1 atm P_{O_2} . Red ones are any probable arcs and black dots are original data. Arcs are convoluted.....	59
Figure 4-1 Typical flowsheet of Pechini synthesis process	62
Figure 4-2 Refined profile of standard Silicon powder sample Nist640d	65
Figure 4-3 Refined XRD pattern of (La _{0.8} Sr _{0.2})CoO _{3-δ}	66
Figure 4-4 Refined XRD pattern of LaSrCoO _{4+δ}	66
Figure 4-5 SEM images of (La _{0.8} Sr _{0.2})CoO _{3-δ} and LaSrCoO _{4+δ} with 20k and 30k magnifications, respectively	68
Figure 4-6 Refined XRD pattern of (Ce _{0.9} Gd _{0.1})O _{1.95}	69
Figure 4-7 SEM image of (Ce _{0.9} Gd _{0.1})O _{2-δ} with 40k magnification	70
Figure 4-8 (a) Top view and (b) cross section of half cells accommodating thick porous cathodes.....	71
Figure 4-9 EIS responses of physically mixed powder (denoted as PM) at differential temperatures and ambient air	73
Figure 4-10 EDS mapping of physically mixed powder at 400 magnification	74
Figure 4-11 Refined pattern of DP-5	78
Figure 4-12 Refined pattern of DP-1	79
Figure 4-13 Refined pattern of DP-3	80
Figure 4-14 Change in lattice parameter a with respect to Sr doping in LSC ₂₁₄ [149,186].....	82
Figure 4-15 Change in lattice parameter c with respect to Sr doping in LSC ₂₁₄ [149,186].....	83
Figure 4-16 Change in lattice parameter a with respect to Sr doping in LSC ₁₁₃ [191,192].....	83

Figure 4-17 Change in lattice parameter c with respect to Sr doping in LSC_{113} [185,193,194]	84
Figure 4-18 Particle penetration scenarios schematic illustrations (a) Extreme maximization, (b) intermediate penetration and (c) as if physical mixture	88
Figure 4-19 400 °C EIS responses of symmetric cells of DP-5, DP-1, DP-3 and PM with respect to differential P_{O_2}	90
Figure 4-20 Comparison of all EIS spectra (left) and that of single phase cathodes at 400 °C and 0.21 atm P_{O_2}	92
Figure 4-21 Comparison of all cells at 500 °C with varying oxygen.....	93
Figure 4-22 500 °C EIS responses of symmetric cells of DP-5, DP-1, DP-3 and PM with respect to differential P_{O_2}	93
Figure 4-23 550 °C EIS responses of symmetric cells of DP-5, DP-1, DP-3 and PM with respect to differential P_{O_2}	94
Figure 4-24 Comparison of all cells at 550 °C with varying oxygen.....	95
Figure 4-25 600 °C EIS responses of symmetric cells of DP-5, DP-1, DP-3 and PM with respect to differential P_{O_2}	96
Figure 4-26 Comparison of all cells at 600 °C with varying oxygen.....	97
Figure 4-27 650 °C EIS responses of symmetric cells of DP-5, DP-1, DP-3 and PM with respect to differential P_{O_2}	97
Figure 4-28 Comparison of all cells at 650 °C with varying oxygen.....	98
Figure 4-29 LSC_{214} response at 650 °C with varying P_{O_2}	99
Figure 4-30 Comparison of all cells at 700 °C with varying oxygen.....	100
Figure 4-31 700 °C EIS responses of symmetric cells of DP-5, DP-1, DP-3 and PM with respect to differential P_{O_2}	100
Figure 4-32 A summary of electrochemical behaviors of symmetric cells	102
Figure 4-33 EDS mapping of physically mixed powder at 45000 magnification...	103
Figure 4-34 Cross sectional SEM images of symmetric cells showing cathode thicknesses (a) DP-1, (b) DP-3 (c) LSC_{214} (d) LSC_{113} (e) PM and (f) DP-5	106
Figure 5-1 Schematic illustration of symmetric cells. (a) Cross section of cell and (b) Top/bottom view. Lateral size of air exposed surface (depicted by black) is seen in (b).....	110

Figure 5-2 EIS Spectra of cell-10% LSC ₁₁₃ at 650 and 700 °C	112
Figure 5-3 Equivalent circuit model #1 for cell-10% LSC ₁₁₃ at 650 and 700 °C ...	113
Figure 5-4 EIS Spectra of cell-10% LSC ₁₁₃ at 600 and 550 °C	113
Figure 5-5 Equivalent circuit model #2 pertaining to 600, 550, 500 and 450 °C [133,138].....	114
Figure 5-6 EIS Spectra of cell-10% LSC ₁₁₃ at 500 and 450 °C	114
Figure 5-7 EIS Spectra of cell-10% LSC ₁₁₃ at 400 and 380 °C	115
Figure 5-8 EIS Spectra of cell-10% LSC ₁₁₃ at 360 and 340 °C	116
Figure 5-9 EIS Spectra of cell-10% LSC ₁₁₃ at 320 and 300 °C	116
Figure 5-10 SEM image of cathode of cell-10% LSC ₁₁₃ . (a) dense microstructure of cathode free surface, (b) surface of Gold current collector and (c) lateral thickness of cathode free surface	118
Figure 5-11 EIS Spectra of cell-25% LSC ₁₁₃ at 700 and 650 °C	119
Figure 5-12 EIS Spectra of cell-25% LSC ₁₁₃ at 600 and 550 °C	120
Figure 5-13 EIS Spectra of cell-25% LSC ₁₁₃ at 500 and 450 °C	120
Figure 5-14 EIS Spectra of cell-25% LSC ₁₁₃ at 400 and 380 °C	121
Figure 5-15 EIS spectra of cell-25% LSC ₁₁₃ from 360 to 300 °C.....	122
Figure 5-16 Cross section of cell-10% LSC ₁₁₃ manifesting the μm level thickness	123
Figure 5-17 Cell resistances at 700 °C as function of time.....	124
Figure 5-18 Temperature dependence of area specific resistance (ASR) pertaining to electrolytes and differential cathodes.....	126

NOMENCLATURE

APT	: Atom Probe Tomography
ASR	: Area Specific Resistance
BBP	: Benzyl Butyl Phthalate
BSCF	: $(\text{Ba}_{1-x}\text{Sr}_x)(\text{Co}_{1-y}\text{Fe}_y)\text{O}_{3-\delta}$
CTE	: Coefficient of Thermal Expansion
D	: Diffusivity
DWSB	: $(\text{Dy}_x\text{W}_y\text{Bi}_{1-x-y})\text{O}_{2-\delta}$
EDS	: Energy Dispersive X-rays Spectroscopy
EIS	: Electrochemical Impedance Spectroscopy
ESB	: $(\text{Er}_{1-x}\text{Bi}_x)\text{O}_{3-\delta}$
FIB	: Focused Ion Beam
GDC, CGO	: Gadolinium Doped Ceria- $(\text{Ce}_{1-x}\text{Gd}_x)\text{O}_{2-\delta}$
k^*	: Tracer Oxygen-Surface Exchange Coefficient
k^q	: Electrical Oxygen-Surface Exchange Coefficient
l_δ	: Critical Utilization Length
LSC ₁₁₃	: $(\text{La}_{1-x}\text{Sr}_x)\text{CoO}_{3-\delta}$ -Perovskite
LSC ₂₁₄	: $(\text{La}_{1-y}\text{Sr}_y)_2\text{CoO}_{4\pm\delta}$ -Ruddlesden Popper
LSCF	: $(\text{La}_{1-x}\text{Sr}_x)(\text{Co}_{1-y}\text{Fe}_y)\text{O}_{3-\delta}$
LSF	: $(\text{La}_{1-x}\text{Sr}_x)\text{FeO}_{3-\delta}$
LSGM	: $(\text{La}_{1-x}\text{Sr}_x)(\text{Ga}_{1-y}\text{Mg}_y)\text{O}_{3-\delta}$

LSM	: $(\text{La}_{1-x}\text{Sr}_x)\text{MnO}_{3\pm\delta}$
MIEC	: Mixed Ionic and Electronic Conductive
MHz, mHz	: 10^6 Hz, 10^{-3} Hz
ORR	: Oxygen Reduction Reaction
PEG	: Polyethylene Glycol
PLD	: Pulse Laser Deposition
PVB	: Poly(vinyl butyral-co-vinyl alcohol-co-vinyl acetate)
S/cm	: Siemens Per Centimeter
ScSZ	: $(\text{Zr}_{1-x}\text{Sc}_x)\text{O}_{2-\delta}$ -Scandia Stabilized Zirconia
SEM	: Scanning Electron Microscopy
SOFC	: Solid Oxide Fuel Cell
TEM	: Transmission Electron Microscopy
TPB	: Three (Triple) Phase Boundary
XRD	: X-Ray Diffraction
YSZ	: $(\text{Zr}_{1-x}\text{Y}_x)\text{O}_{2-\delta}$ -Yittria Stabilized Zirconia
σ_e	: Electrical Conductivity
σ_i	: Ionic Conductivity
δ	: Oxygen Vacancy

CHAPTER 1

INTRODUCTION

SOFCS are energy conversion devices capable of converting chemical energy of fuels directly to electricity without the limitations of Carnot cycles [1]. Hence as opposed to internal combustion engines, SOFCs yield significantly higher energy conversion efficiencies namely 40-50% [2,3] which can be improved to higher values with the assistance of cogenerations systems [4] as stationary applications.

It is, no doubt, very easy to combust a fuel, which is process of anode part in a fuel cell. But the key is the oxygen reduction process occurring on the cathode part and having high activation energy. This situation makes oxygen reduction reaction (ORR) at the cathode rate-limiting step of SOFC operation [5]. In other words, high activation energy requirement for ORR, constituting the main utilization problem of SOFCs, is the cost of high energy conversion efficiency of SOFCs.

Fortunately, this cost has been satisfied by mixed ionic and electronic conductive (MIEC) oxides at temperatures around and above 800 °C [3,6]. It is known that electrochemical redox reactions are catalyzed at triple phase boundaries (TPB) at which gas phase, electrically conductive phase and ionic conductive phase meet [7]. These doped oxides (MIEC oxides) involve both type of conductivities within their crystals, extending the TPB to complete material. That's why introduction of these oxides have accelerated the researches on SOFCs in a consequence of catalytic effect of them on oxygen reduction process [6]. These oxides, in most of the time, are in the form of ABO_3 compound named as perovskite where A site is shared by both rare earth and alkaline earth elements (i.e. La and Sr) and B represents reducible transition

metal such as Fe, Co, Mn, Ni. Thanks to their mixed electronic and ionic conduction (MIEC) and resulting catalytic effect, overall ORR have been facilitated significantly.

However, reduction of molecular oxygen gas is not an easy process, still demanding elevated temperatures in spite of positive effect of MIEC oxides. Thus, rendering a SOFC feasible alternative to internal combustion systems by yielding a commercial SOFC still requires further improvements of cathode materials capable of catalyzing ORR well through the cathode not only at elevated temperatures but also at lower temperatures since high operation temperatures, namely 800 °C, is responsible for short-term degradation [8,9]. Hence operation temperature should be reduced to 500 °C or even to 400 °C for micro devices [10–12].

Among all types of ABO_3 complex oxides, LSC has always been the best in terms of both ionic and electronic conductivity [13] and outstanding regarding surface oxygen exchange properties [14,15]. This superiority is valid for all Cobalt containing perovskites in fact. However, both its very high CTE with respect to state-of-the art electrolyte materials causing crack formation or delamination [16,17] and chemical instability problem [18,19] have always been the main causes limiting their utilization. Especially in order to completely get rid of chemical stability problem, namely in most cases insulating SrO_x segregation through cathode surface, satisfactorily reduced resistances should be achieved from cell at or below 400°C, which is critical threshold for SrO_x segregation [18]. Low temperature regime is also safe for probable crack/delamination failures regarding cobalt containing complex oxides. On the other hand, lower temperatures require higher activation energy for oxygen reduction [20] deteriorating SOFC application by enhancing cell resistance.

Nonetheless, anomalously enhanced oxygen reduction kinetic around the $(La_{1-x}Sr_x)CoO_{3-\delta}/(La_{1-y}Sr_y)_2CoO_{4+\delta}$ interface has been reported in recent years, yielding a thousand time greater surface oxygen exchange coefficient, k , with respect to the single phases [15,21]. Exploiting this interface induced ORR promotion can decrease operating temperature of SOFC cathode, extending the chemical stability of it. Extreme maximization of this hetero interface especially through a thin film cathode can drastically reduce ASR since in case of thin film where bulk ionic transport is facile, the only source of resistance becomes hetero-interfacial electrochemical kinetic

with surface adsorption [5,22], which has already been facilitated by enhancement on surface oxygen exchange coefficient [15]. Aside from sophisticated thin film applications, maximization of this hetero interface regarding conventional thick porous cathodes has a great potential to commercialize SOFC, too. This is certainly possible if ease of fabrication is satisfied.

This study, in this way, focuses on examination of these abovementioned two approaches. As conventional thick porous cathode fabrication approach, maximization of hetero interfaces by synthesizing two phases combination from one unique solution by means of Pechini method [23] as well as physically mixing of them are adopted. Success of hetero interface maximization with this improving approach may have drastically positive consequences in applicability of cathode regarding fabrication. On the other hand, magnetron co-sputtering of each phase from different single phase oxide sputtering targets is adopted as thin film application approach. Achieving necessitated area specific resistance (ASR) by hetero interface maximization at temperatures converging to 400 °C is the main objective regardless of fabrication costs and/or difficulties.

CHAPTER 2

OVERVIEW TO SOFC CATHODES

2.1. Solid Oxide Fuel Cells

The fossil fuel based systems, on which our current technological level of development is established, are falling in such a situation that their legitimacy is getting more and more questionable due to the increasing demand of energy and limited existence of fossil fuels as well as their emissions. This case has directed many researchers to find out new and novel routes for alternative energy conversion systems. While significant portion of them makes use of converting solar energy, which is considered as ‘countable infinite’ energy when the life time of human being is taken into account, in reasonably economic and efficient means, the rest is rather interested in converting existing fossil fuels in highly efficient ways. The researches of this latter group in this way are situated in range of short term aims. Solid oxide fuel cells (SOFCs) fall into this latter category in a consequence of their ability to convert chemical bond energy of fossil fuels directly into electrical energy in highly efficient way namely 40-50% practically [2] and 60% theoretically [24]. This can be extended to 80% by some cogeneration systems [4]. This is because SOFCs can convert chemical energy directly to electricity without limitations of Carnot cycle as opposed to internal combustion system [1].

All the possible energy conversion systems are governed by thermodynamics. Internal combustion engines and SOFCs are not free from this. The known first law of thermodynamics governs all the energy conversion processes; in a closed system, internal energy of systems increases with heat supplied to the system and decreases as this system does work on surroundings. On condition that U is internal energy, Q is

heat supplied and W represents work done by the system, the first law of thermodynamics is expressed as;

$$dU = \delta Q - \delta W$$

While in most cases work term (W) represents P-V type mechanical work, equivalently the work done by compression or expansion of a gas, W is in fact non-homogeneous and it involves many kinds of works even in heat engines such as chemical, electrical, mechanical and so on. These work types except for mechanical work are neglected since they are not exploited.

$$\delta W = \delta W_{electrical} + \delta W_{mechanical} + \delta W_{chemical} + \dots$$

Internal combustion engines convert the energy released as a consequence of breaking chemical bond in fuel into mechanical work. Thus, they are restricted to Carnot efficiency (Eff_c) which can be 100% if and only if temperature of cold reservoir is absolute zero and cooling process takes place *reversibly* [25]. Even if compressing a hot pressurized gas into conditions such that its final temperature would be absolute zero is possible, reversibility of process entails extreme slowness which practically corresponds to infinite time. In this case, work efficiency is 100% but power output is zero. So, the practical maximum efficiency of internal combustion based systems governed by Carnot cycle is at most 25-35% when they yield desired power output due to inevitable process irreversibility and losses, as well [26].

$$Eff_c = 1 - \frac{T_{cold\ reservoir}}{T_{hot\ reservoir}}$$

However, SOFC does not make mechanical work, they are not governed by Carnot cycle and they yield more efficiency whereas their energy conversion process is also governed by the first law thermodynamics. In SOFC, work type is not mechanical it is electrical work.

2.1.1. SOFC Operation

Fuel (or H_2) is provided to anode in SOFCs and here it is oxidized via already reduced oxygen supplied from cathode part, generating water eventually. Reduced oxygen in

cathode should migrate through electrolyte of SOFC to allow the oxidation of fuel. Hence, electrolyte should be very good oxygen ionic conductor and it must be preferentially as thin as possible [27,28]. When it is thin, CTE of electrolyte restricts cathode material. When it is thick on the other hand, both its ionic conduction and chemical compatibility with other components become crucial. So electrolyte has a deterministic effect on SOFC construction [13]. The working principle is illustrated in Figure 2-1.

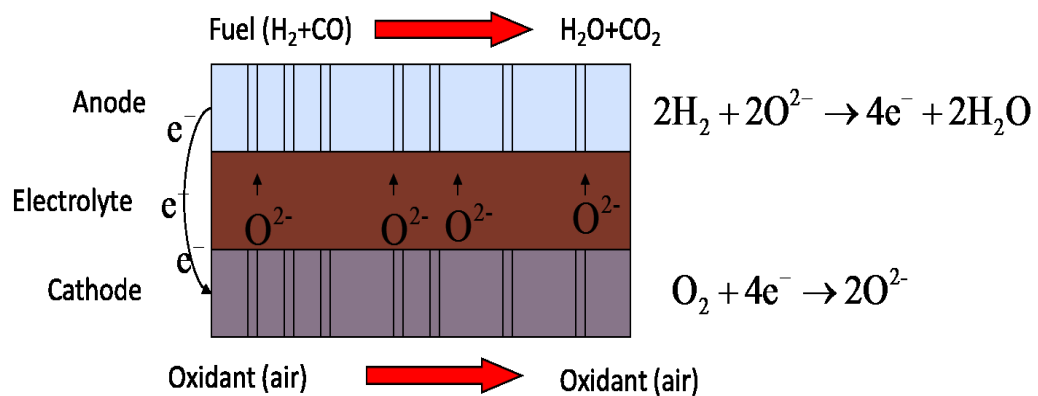


Figure 2-1 SOFC Operation

It is, as expected, very easy to combust a fuel on anode part. Here supplied heat (Q) is same for both internal combustion engines and solid oxide fuel cells. But the key is the oxygen reduction process occurring on the cathode part, expressing work term. This oxygen reduction occurring at the cathode has significantly high activation energy making oxygen reduction on cathode the main rate limiting step in overall SOFC operation [5,27,29]. Low temperatures make this rate limitation more crucial and so the greatest portion of cell resistance is originated from cathode in SOFC [6,30]. That's why SOFC researches are significantly reduced to SOFC cathode researches. What's happening at cathode is that O₂ undergoes direct electrochemical reduction. In other words, cathode of SOFC *catalyzes* electrochemical oxygen reduction, bringing about superior efficiency. This is the main capability of SOFC cathode and the SOFC itself.

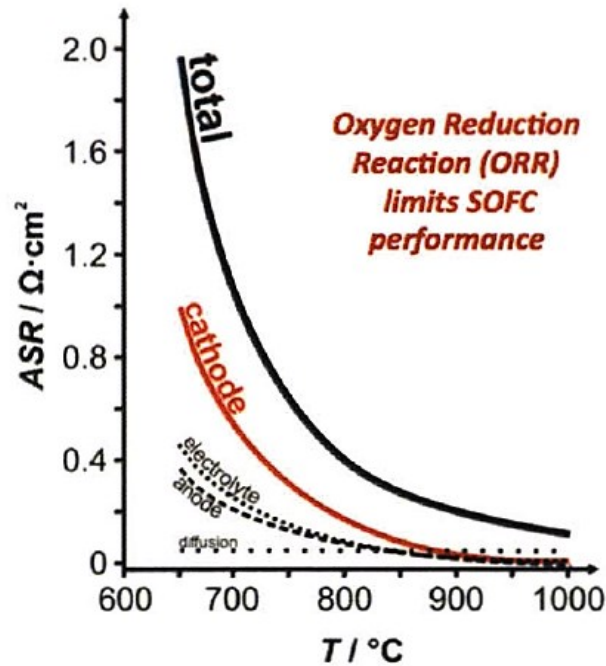


Figure 2-2 ASR as a function of temperature for a SOFC consisting LSM as cathode, YSZ as electrolyte and Ni-YSZ as anode and operating with hydrogen as fuel [30]

It is most of the time neglected but energy has always been extremely expensive such that the ‘easily’ obtained fossil fuels are results of millions of years of accumulation. Formation of those fuels has not been favored by natural processes of earth just like direct electrochemical reduction of oxygen in the air. Everything has a cost to be paid. This cost was millions of years for the formation fossil fuels while it is catalysis of electrochemical reduction of O_2 for utilizing superior SOFC efficiency. So to say, what is done by SOFC cathode researchers is to reduce this cost into capability of mankind to pay, which is expressed by the terms commercialization, feasibility, cost reduction and so on.

In this way, there released some necessities for each component of SOFC. While cathode is the most crucial one among them in terms of its contribution to overall cell polarization resistance, the other component qualifications should also be comprehended, too.

2.1.1.1. Anode Requirements

The principal necessity for anode part of SOFC is high electrical conductivity. Since what happens at anode is electro-oxidation process [31], easy flow of electrons is helpful for better anode performance. Because fuels do not have oxidative characteristics, metals as good electrical conductors can be used for anode. In addition, for more efficient penetration and access of fuel into anode as well as the gas output, high and stable porosity is required [3]. Furthermore, anode is the place at which reduced oxygen meet with fuel provided and forms resultant gases. However, metals are prone to sintering even at intermediate temperatures. In order to sustain porosity, these metals are used to make composite anodes involving an additional ionic conductor [17]. This ionic conductor is commonly the electrolyte material for a successful compatibility, which is to specify CTE and chemical match with electrolyte. Addition of ionic conductor provides TPB at which electrochemical processes are favored [6]. Furthermore, not only with electrolyte but also compatibility with interconnect material should be concerned.

Whereas it is modest, there an is activation energy for fuel oxidation process, which constitutes relatively well smaller part of overall resistance of SOFC as illustrated in Figure 2-2. For further reduction of this resistance, anode should be able to catalyze fuel oxidation process, which can be handled partly by introduction of TPB [7]. If possible, flexibility for fuel type is also sought in anodes. Since in most cases cell is anode supported, anode is expected to be sufficiently strong to withstand the weight of cell.

Nonetheless, fuel oxidation process is relatively complex which makes *a priori* evaluation of a prospective material for anode common. In this way, Ni/YSZ composite is the most widely used one for SOFC due to its capability to more or less satisfy almost all requirements for anode application except for fuel flexibility since Ni/YSZ is susceptible to carbon deposition and sulphur poisoning [32–34]. With the all improving efforts, Ni/YSZ composite is by far the best choice for anode.

2.1.1.2. Electrolyte Requirements

SOFC electrolyte is responsible for transport of reduced oxygen ions and hence should have oxygen ionic conductivity as high as possible with the lowest possible electrical conductivity since electrical conductivity has a reverse effect on ion migration from cathode through anode part [35,36].

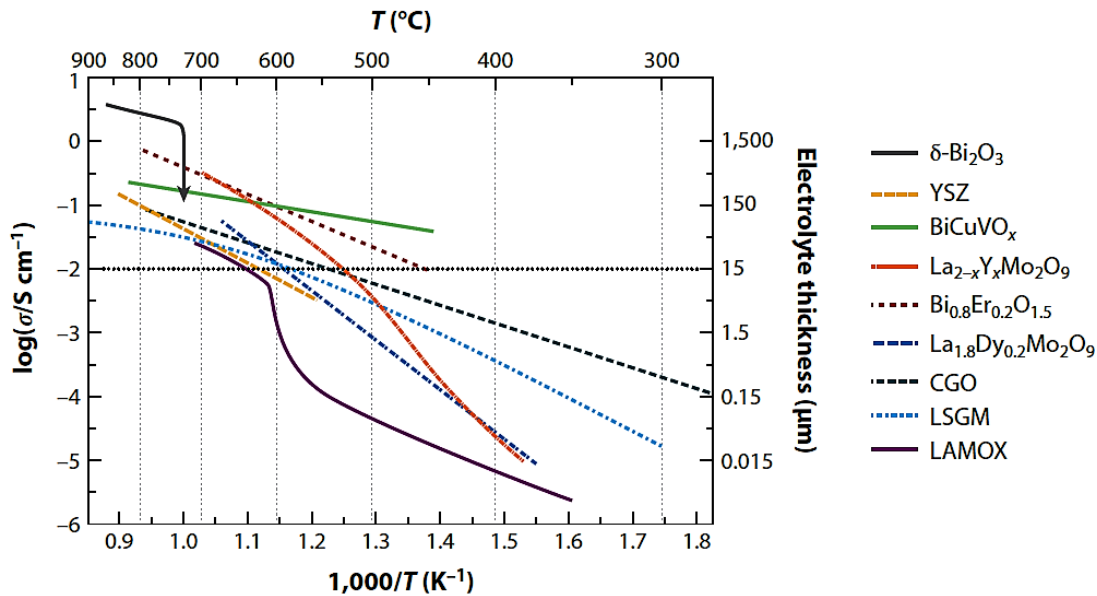


Figure 2-3 Temperature-thickness-conductivity diagram for state-of-the art electrolytes [14]

Generally, 0.01 S/cm at current operation temperature is accepted to be the sufficient ionic conductivity for SOFC electrolyte [14,37]. Since porosity is a scattering factor for ion transport, electrolyte should also be dense and as thin as possible along with stability under both reducing and oxidizing environments [38]. However, this thin electrolyte necessitates very high thermo-mechanical compatibility with other components, that is to say that CTE matching of electrolyte with both anode and cathode is crucial. Relationship among temperature, thickness and conductivity is summarized in Figure 2-3.

Electrolyte should be stable both at anode and at cathode. Since it is principal component in SOFC stack [39], it should be low cost material. Cubic structure should also be satisfied in order for isotropic diffusion properties. Since this criterion is

already achieved in many electrolyte options, it is not mentioned in literature but it is still a criterion [40]. Consequently, the most suitable material for electrolyte is YSZ [17,41].

2.1.1.3. Cathode Requirements

The first and the most important parameter is the catalytic effect of it in terms of oxygen reduction. In initial investigations on SOFC, it was (and is still) believed that this electrochemical reduction takes place at three phase boundaries (TPB) where gas phase (air), electrical conductor and ionic conductor meet [6]. So a good cathode must have extended three phase boundaries for favored electrochemical reduction of oxygen. But there is more. Cathode should also be stable under oxidizing environment, which is termed as chemical stability. This chemical stability with respect to interconnects and electrolyte must also be taken into account [5].

The other important parameter is structural stability characterized by CTE mismatch between cathodes, electrolytes and interconnects. CTE mismatch must be in tolerable limits for them in order for avoiding delamination or crack formation [16,17]. Moreover, cathode should have sufficient ionic and electronic conductivities. Sun *et al.* [13] states 100 S/cm as threshold for electrical conductivity. Ionic conductivity is mostly characterized by oxygen ion (D) and oxygen vacancy diffusivity (D_v) [42] and if intermediate temperature range (500-700 °C) is taken into consideration, 10^{-9} cm²/s ionic and 10^{-7} cm²/s vacancy diffusivities are considerable [42,43]. Apart from Co containing cathodes, which could have even better ionic conductivities than electrolytes [44], typical ionic conductivity of cathodes is on the order of 10^{-3} S/cm at intermediate temperature range [13,45]. Since the crucial role of ionic conductivity is extension of active regions for oxygen reduction from TBP to whole air exposed surface, rather than ionic conductivity solely, care must be on combined effect of vacancy and oxygen ion diffusivities which *together* determine rate of oxygen reduction by facilitating surface oxygen exchange [27,46,47]. So ionic conductivity is indicator of cathode activity.

For cathodes which are not in thin film form, enhanced porosity becomes another crucial parameter since it promotes oxygen gas phase diffusion through cathode and

cathode/electrolyte interface [48,49]. This provides excess oxygen penetration into cathode [4]. Finally, for successful commercialization, cathode should have low cost.

In order to achieve commercial SOFC, at least in terms of transport applications, overall cell resistance should not exceed $0.5 \Omega\text{cm}^2$ [1,32]. If one considers the greatest portion of cell resistance is originated from cathode processes, $0.2 \Omega\text{cm}^2$ cathode resistance could be tolerable. If equal contribution from each component is assumed, then $0.15 \Omega\text{cm}^2$ would be the aimed ASR value for cathode. In either case, the cathode offering the desired ASR as well as aforementioned requirements depending on cell conditions becomes a candidate for a commercial SOFC.

In the initial SOFC studies, cathodes were composites of noble metals for electrical conduction and ionic conductor oxides as well as they were porous to meet maximization of triple phase boundaries [6,50,51]. However, introduction of MIEC perovskites have changed this case very drastically. Both ionic and electrical conduction as well as extension of TPB has been satisfied by one single component thanks to introduction of MIEC oxide.

2.2. MIEC Perovskites

Perovskite oxides are characterized by their ABO_3 anion-cation stoichiometry. A and B can be any kinds of cations and anion does not have to be oxygen only in principle. N and S are other common anions regarding perovskite ceramics. But concerning SOFC cathodes, anion is oxygen, A site cation combines rare earth (La, Pr, Ce) and alkaline earth (Ba, Sr) cations and B site is transition metals namely Co, Fe, Ni, Mn, Cr. B-site substitution is also possible.

In perovskite structure, A-site cation is greater than B-site cation in terms of ionic radius. There is 12-fold oxygen ion coordination for A-site cation and 6-fold oxygen ion coordination for B-site cation in perovskite structure. This is illustrated in Figure 2-4 given below.

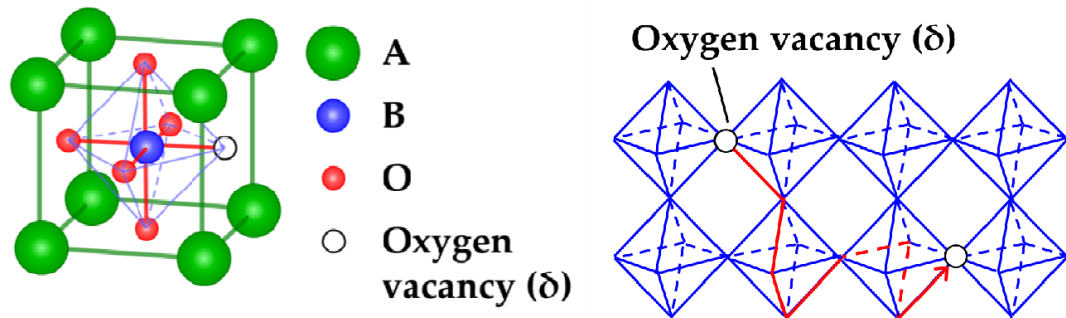


Figure 2-4 Perovskite Structure showing atom/vacancy coordination (left) and path for oxygen ionic transport (right) [52]

The fact that A site is shared by both rare earth and alkaline earth cations is important as it brings about mixed ionic and electronic conduction (MIEC) in perovskite structure. Sharing A and/or B site by at least two cations is characteristic leading to mixed ionic and electronic conduction of perovskite oxides [53].

Perovskite oxides are, one way or another, ionic materials in which charge neutrality must be preserved. Strict stoichiometry between anions and cations is either prerequisite or consequence in ionic materials when anions and cations through crystal have certain unique valence. This is the point at which conventional ceramics and MIEC perovskite oxides differ from each other. Whenever one of the constituent cations is aliovalent, that is, sites are substituted by cations having different valences, the typical conventional oxides transform to non-stoichiometric oxides.

In MIEC perovskites, A-site in crystal is doped by a cation having different valence than host atom. Host atom is generally rare earth having +3 valence and dopant is alkaline earth having +2 valence. This process deteriorates the charge neutrality within crystal structure. Substituting cation having +2 valence in place of host atom having +3 valence makes crystal structure more negative. In this case, charge imbalance creates polarization inside the crystal structure. This charge polarization becomes cumulative through subsequent lattices. At this point one must keep in mind that electrons are not free in ionic materials and they are carried by nucleus. So, movement of an electron, i.e. charge, dictates the movement of an atom itself. If it is considered

that charge polarization is cumulative and extended through subsequent lattices, i.e. all the material, all the positively charged atoms should be strictly separated from all the negatively charged atoms. Movement of so many atoms requires immense energy. This energy is called Madelung energy in literature [54]. The crystal structure ‘prefers’ to satisfy charge balance by releasing oxygen, making crystal more positive in aforementioned case where lattice becomes more negative as a consequence of lower valence cation doping. A-site is doped with a higher order positively charged cation, this would result in accepting excess oxygen atom to make crystal more negative. So oxygen non-stoichiometry is here introduced as the way to satisfy charge neutrality in oxides. This oxygen non-stoichiometry, whether in the form of deficiency or excessiveness, facilitates oxygen migration through oxide. In most of the cases, it is the oxygen deficiency in SOFC perovskites. Empty oxygen sites promote kinetics of bulk ionic transport [6] as well as surface oxygen exchange properties by providing empty available sites for molecular oxygen [55] to get reduced. In this way, oxygen deficiency reduces energy barrier for electrochemical reduction of oxygen gas in air [56].

Nevertheless, oxygen non-stoichiometry is not the only way of charge compensation. For the cases where B-site cation is multivalent, i.e. it can have different valence states, charge compensation can be derived by changing valence of B-site ‘reducible’ transition metal. This is the basis of electrical charge compensation and electrical conductivity. In this compensation process, electrical conduction by hopping mechanism is observed in MIEC perovskite [57].

In this case, B-site transition metal partially undergoes valence change in order to establish charge balance. As a consequence, there releases hopping sites for electrons/holes transition yielding n-type or p-type conductivity. Increasing number of these available hopping sites promotes electrical conductivity. Maximum electrical conductivity, in this sense, is obtained where the ratio of host cation to dopant cation is 1 in A-site [58]. This is valid of course when the dominant charge compensation mechanism is B-site cation valence transition. A good example to this is $(\text{La}_{1-x}\text{Sr}_x)\text{MnO}_{3-\delta}$ (LSM) in which almost all charge balance is achieved by electronic compensation, i.e. valence transition of $\text{Mn}^{3+}/\text{Mn}^{4+}$ [59]. Regarding cathode materials,

for all cases in which trivalent A-site cation is doped with divalent cation, electrical charge compensation mechanism becomes operative. That's why for instance BSCF has low electrical conduction since both host and dopant atoms have the same valence states. Depending mainly on B-site cation, degree of electrical conduction varies [13].

Here, prior to going further, there is a need for further elaboration. Extent of oxygen deficiency is a strong function of temperature, i.e. oxygen deficiency is triggered at increasing temperatures. This is to say that oxygen deficiency mechanism for charge compensation becomes dominant mechanism at high temperatures [60,61] by virtue of more ability to overcome vacancy formation activation energy at increasing temperatures. This is also explained by extrinsic and intrinsic conductivities in ionic crystals.

It is apparent that cation substitution triggers anion vacancy formation even in the low temperatures due to the need to maintain charge neutrality. In the absence of impurity, vacancy formation energy could not be surmounted at such low temperatures. These are impurity induced vacancies and their number is dominant over thermally induced ones at lower temperatures. But as temperature increases, formation of thermally induced vacancies becomes more favorable than formation of impurity induced vacancies (vacancies for charge compensation), resulting dominance of thermally induced vacancies. Absolutely, if there is a transition metal, valence state change is much easier than accommodating impurity induced vacancies likewise MIEC perovskites.

Since the dominant one is expected to govern the overall ionic movement, from low to high temperatures, there releases different conduction regimes separated by certain critical temperature named as 'knee'. Dominance of thermally induced vacancies is such that ionic conductivity of oxide is what it would be if there were no substitution. So, this high temperature conductivity is called as intrinsic while the one at low temperatures dictated by substitution is called as extrinsic. Above knee temperature, $\ln D$ vs $1/T$ graph is seen to be linear, implying that this is activated behavior dictated by vacancy formation energy barrier. But at lower temperature the activation energy barrier is not caused by vacancy formation and thus temperature change is less

effective. So the same linearity is achieved with a smaller slope as illustrated in Figure 2-5.

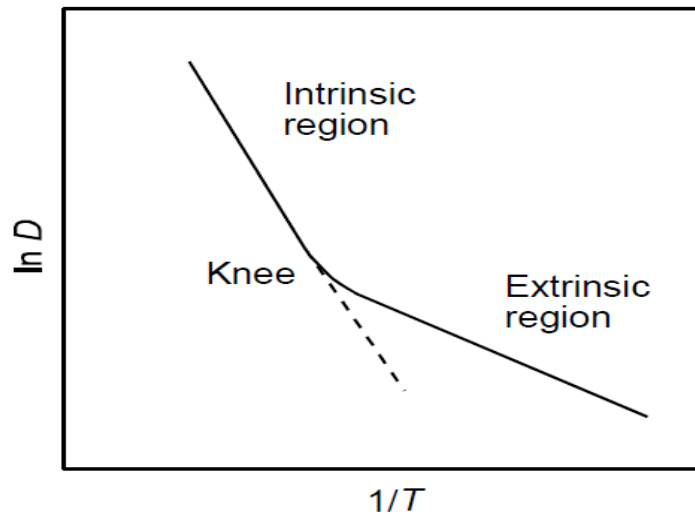


Figure 2-5 Intrinsic and extrinsic intervals in substituted ionic crystals

This phenomenon is expected to reduce electrical conduction at increasing temperatures since in this case, charge neutrality is achieved mainly by vacancy mechanism instead of electrical charge compensation of B-site transition metal. But of course this is just a generalized case valid especially for ionic crystals comprising high anion vacancies like LSC_{113} . Otherwise many cathode perovskites like LSF exhibit semiconductor behavior in which increasing temperatures (up to certain degree [62]) lead to enhancement in conductivity. But this is possible only when higher temperatures do not *significantly* affect oxygen non-stoichiometry and band gap properties. Cobalt containing perovskites have high oxygen vacancies and particularly exhibit metallic like conduction behavior [6]. But for instance, dominance of oxygen defects can only be possible after $800\text{ }^\circ\text{C}$ [62].

When LSC_{113} is heavily doped, an ongoing decrease in electrical conductivity is observed. When $x \leq 0.2$, raising regime with respect to increasing temperature turns out to be stationary after intermediate temperature range is surpassed [63,64].

On the other hand, LSM shows reverse behavior; higher temperatures bring about increase in electrical conduction [65]. This is because LSM accommodates excess oxygen dictating further B-site (Mn) charge disproportionation resulting in higher electrical conduction [59].

When both of the charge compensation mechanisms are effective within perovskite structure, it becomes a satisfactorily *mixed* ionic and electronic conductor. It should be kept in mind that all oxides are MIEC in principle. It is important to state that whether the oxide is MIEC is dependent upon sensitivity expectation from material, i.e. application requirements. Electronic mobility is around 10^4 to 10^8 times greater than ionic mobility [66]. Thus, for competent conduction among these two requires 10^4 to 10^8 times greater number of ionic charge carrier than electronic carriers, which is in fact only possible, theoretically, with ceramics already by virtue of their ability to form excess vacancies. But this is not realistic. For instance, $(\text{La}_{0.6}\text{Sr}_{0.4})(\text{Co}_{0.8}\text{Fe}_{0.2})\text{O}_{3-\delta}$ is known to be a “good” MIEC perovskite having electronic conductivity of 269 S/cm and ionic conductivity of 0.058 S/cm at 800 °C [67]. In many other perovskites, difference between ionic and electronic conduction is even more drastic [13].

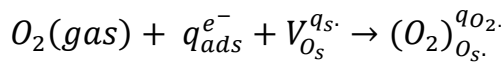
So it should be remembered that electronic conduction is far more than ionic conduction in mixed conductors. Nonetheless, which mechanism will be, in this relativity, dominant over another is strong function of several variables namely dopant degree (value of x), temperature, crystal/electrical structure (band gap properties) and P_{O_2} . So, it is not easy to sum up with some certain conclusions. Resulting combinational properties exhibit wide variations.

But the case is different for electrolyte materials where pure ionic conduction is observed. In these oxides, electrical conduction is not required; the only charge compensation mechanism is vacancy formation. When cations are fixed in terms of valence state, this necessity can be achieved. Nevertheless, depending upon the conditions, electrolyte may also show some slight electrical conduction.

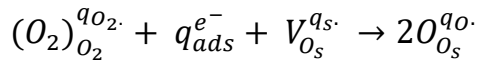
Exceptions are for confirmation of general rules. This general rule is that, introduction of mixed ionic and electrical conduction as well as superior exchange properties bring about thermodynamic instabilities manifested as structural and chemical instabilities. So, what creates superior properties in MIEC perovskites are also the fundamental reasons for instability of them which can only be solved by significantly reducing temperature.

Importance of mixed ionic and electronic conduction is originated not only from extension of TPB through bulk but also from enhanced oxygen ionic transport through bulk and electro catalytic effect on surface oxygen exchange which is also a strong or weak function of electrical conductivity, too. It is apparent that excess existence of electrons on cathode surface will favor reduction of oxygen gas. So, electrical conduction is desired. Non-stoichiometry is also effective in this reduction by virtue of providing available sites for eventual incorporation of oxygen [27,55] and oxygen transport. Steps of electrochemical reduction on surface are as follows;

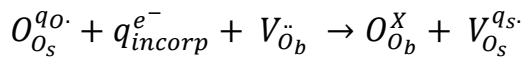
Adsorption;



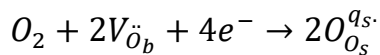
Dissociation;



Incorporation;



Overall;



What are meant by O_2 , V and O are diatomic oxygen, oxygen vacancy, oxygen atom respectively. O_b and O_s as subscripts correspond to location of species at bulk and surface oxygen sites. Dots and minus as superscripts refer to positive and negative charges and q is simply transferred charge. Superscript x denotes the neutral charge of species.

Oxygen reduction through cathode is non-homogeneous process; it has many steps. Even only surface processes are divided into different steps and existence of vacancy, which can also be correlated by ionic diffusivity, is crucial for more facile process. Surface/bulk diffusions, charge transfer at different interfaces are other ones as [15].

Elaboration of surface process is mainly because of the fact that introduction of MIEC brings about converting double phase boundary (DPB) surface into TPB, which is point at which ionic, electronic conductors and gas phase meet. Thus surface/air contact becomes TPB. When cathode is in thin film form, all the electrochemical reduction steps given above take place at surface and surface comprises great importance. This is illustrated in Figure 2-6.

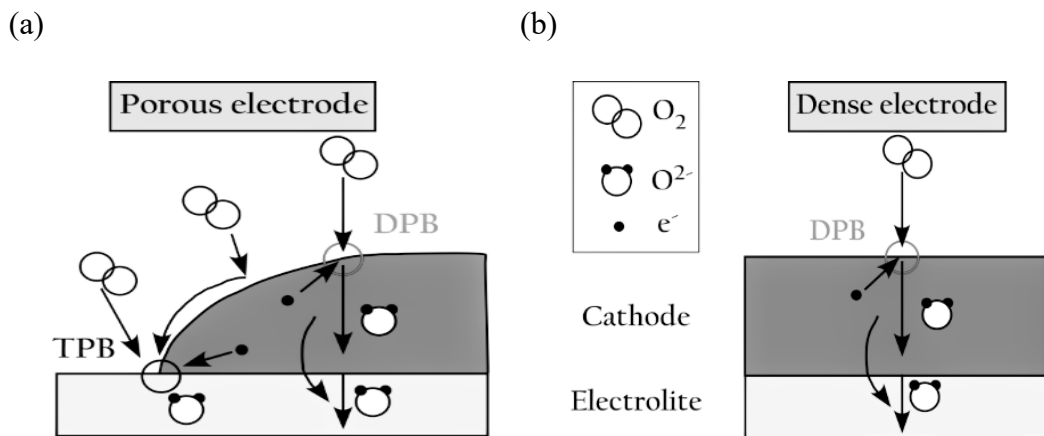


Figure 2-6 Paths regarding the types of SOFC cathode [52]

Different conduction types (ionic or electronic) have catalytic effect on different parts of overall electrochemical reduction process. Electrical conduction catalyzes adsorption process while non-stoichiometry facilitates incorporation by giving oxygen vacancies [55]. Once it is incorporated on surface, reduced oxygen should diffuse through cathode/electrolyte interface in facile manner. Non-stoichiometry is also functional in this respect.

Aforementioned surface electrochemical steps as well as bulk are characterized by surface oxygen exchange constant (k) and oxygen ion diffusivity (D) [68]. Importance

of these parameters will be comprehensively evaluated in upcoming section under the title of EIS Analysis.

Whereas mixed ionic and electrical conduction is the principle requirement in SOFC cathodes, it is not the only one; various other parameters, as stated in previous pages, should also be involved and evaluated in eventual selection. These are chemical/structural stability and CTE compatibility with electrolyte.

2.2.1. Structural Stability

Structural stability is frequently correlated with the term Goldschmidt tolerance, denoted as t , defined below. When $0.77 \leq t \leq 1$, perovskite is said to be stable according to this relation;

$$t = \frac{r_A + r_O}{\sqrt{2} (r_B + r_O)}$$

r_A, r_O and r_B are radii of A, oxygen and B in ABO_3 structure respectively. When perovskite structure is cubic, Goldschmidt tolerance is equal to unity. Approaching unity brings about more closely packed structure whether it is slightly higher or slightly lower. On the other hand, $t=1$ corresponds to the same ionic radii for both A-site atom and oxygen [69]. However, due to A-site substitution, BO_6 octahedron gets distorted and cubic perovskite transforms to other crystal systems such as rhombohedral, orthorhombic and hexagonal [70]. Transformation from cubic to other systems brings about anisotropy in properties through cathode. This distortion as well as Goldschmidt tolerance change as a function of dopant degree for some state-of-the-art perovskites can be found in ref [71].

A correlation between cation valences and eventual crystal system can be established. When $A^{3+}B^{3+}O_3$, cubic symmetry is not allowed while cubic symmetry is favored in $A^{2+}B^{4+}O_3$ and $A^{1+}B^{5+}O_3$ [71].

Any probable crystal structure change during heating or cooling of SOFC must also be of concern in evaluating structural stability. Change in crystal structure during heating is rare but still it should be taken into account. For example, ScSZ has been reported to change crystal structure at around 600 °C when dopant degree, x , is more than 0.15 [35]. BSCF on the other hand is considered to be very good candidate for SOFC cathode with its enhanced surface exchange properties and the vacancy content but its main limitation is lattice instability [27]. Alteration of its crystal structure with increasing temperature makes BSCF prone to cracks or residual stress formation.

It must be noted that, structural stability is very important and it has a deterministic effect in overall stability of cathode. Inevitable result of cation size differential brings about less closely packed structures leading thermodynamic instability as well as anisotropic properties manifesting themselves as chemical instability eventually. So, thermodynamic (or chemical) stability becomes a function of structural stability and structural stability is expressed as Goldschmidt tolerance. Its importance is such that, for example, deviation from cubic symmetry causes a decrease in ionic conductivity [72]. Or, since electrical conduction occurs via electron-hole hopping through B-O-B chains, structural changes drastically affect electrical conduction.

High oxygen reduction activities have been reported till now between $(\text{La}_{0.8}\text{Sr}_{0.2})\text{CoO}_{3-\delta}/(\text{La}_{0.5}\text{Sr}_{0.5})_2\text{CoO}_{4\pm\delta}$ or $(\text{La}_{0.6}\text{Sr}_{0.4})\text{CoO}_{3-\delta}/(\text{La}_{0.5}\text{Sr}_{0.5})_2\text{CoO}_{4\pm\delta}$. In both cases crystal structures are rhombohedral and tetragonal for LSC₁₁₃ and LSC₂₁₄ respectively. Therefore, tuning structural stability is not possible in the present work.

2.2.2. Chemical Stability

While chemical stability is important concerning all component of SOFC [73], in this text it will be evaluated only regarding cathode part. Chemical stability of cathode in most of the cases is associated with both elemental reactivity of cathode with electrolyte and dopant cation segregation through cathode surface [74,75]. But stability under various operation environments should also be concerned as well as microstructural degradation and poisoning of components [76,77]. All these chemical stability problems constitute the main underlying reason and makes it necessary to decrease operation temperatures of SOFCs.

Elemental reactivity with cathode is very significant problem especially regarding cobaltite perovskites constituting the subgroup of perovskites having the best electrical conductivity properties. The most popular and commercially most favorable electrolyte in terms of performance and ionic conduction is YSZ. However, YSZ is reactive with cobalt containing perovskites at intermediate temperatures to form insulating $\text{La}_2\text{Sr}_2\text{O}_7$ [78] and SrZrO_3 [74]. On the other hand, LSM is a very good state-of-the-art cathode in this aspect. Only the temperatures above $1000\text{ }^\circ\text{C}$, formation of $\text{La}_2\text{Sr}_2\text{O}_7$ was observed between LSM and YSZ [59]. Thus, utilization of LSM at around $900\text{ }^\circ\text{C}$ is possible in terms of reactivity with electrolyte. The main strategy to solve this problem is to make coating on YSZ surface by GDC as a barrier layer at the cost of reducing ionic conductivity slightly since there is no reactivity between Ceria based electrolytes and cobaltite [21]. While there are various and better alternatives for electrolyte in terms of ionic conductivity such as ScSZ, LSGM, DWSB and ESB, YSZ represents the optimum choice. Here it can be stated that desired ionic conductivity for electrolyte is 10^{-2} S/cm [14], which is strongly promoted by cubic structure and so type of dopants is preferred accordingly.

Other concern regarding the chemical stability is microstructural stability namely particle coarsening [73]. But this is relevant only in case of porous cathodes, which is beyond the scope of this study. But in terms of anode, this should be regarded since when cathode and electrolyte are thin, then cell should be anode supported, dictating anode to be relatively porous and thick.

A SOFC stack inevitably involves interconnect materials which are generally metals due to their strength as well as very high electrical conductivity [79]. The most popular and successful interconnect material is the doped LaCrO_3 as well as electrically conductive metals, both including Cr and at high temperatures Cr poisoning is observed [80]. The most drastic effect of high temperature emerges regarding this interconnection [79]. So, the greatest portion of driving force for temperature reduction is caused by interconnect material problems [17]. Significantly reduced temperature is expected to make steels useful for application.

Aforementioned aspects must be of great concern regarding SOFCs in general. But elaborating them all is beyond the scope of this work. So, the main focus, here, is LSC,

i.e. the material under study in this thesis. In this way, aside from thermo-mechanical compatibility and reactivity with YSZ, the most critical issue regarding LSC cathodes is Sr segregation towards surface, i.e. phase instability [81].

2.2.2.1. Surface Strontium Segregation

Surface Sr segregation is quite severe problem regarding LSC [9,82,83] such that ASR of cell becomes 10 times higher within only first three days [9,18]. The same surface Sr segregation problem is valid for LSM, too [8,59,81,84]. Observation of such problem even in the most stable cathode (LSM) is remarkable. But kinetic of surface Sr segregation in LSC is extremely fast.

At this point it should be pointed out that Sr migration to surface is not a problem. Contrary, in some cases, Sr migration has been proven to be functional in stabilizing some interfaces [11,85]. However, after a threshold, migrated Sr is suspected to be beyond the solubility limit of structure and this has been demonstrated to lead to phase separation as SrO_x on surface [84]. This is the scenario that should be avoided since this SrO_x blocks ORR [75,86]. However, phase separation and resulting blockage of ORR seem to be inevitable for long term. This 'long time' is very short for LSC namely several days [9] .

The driving force for Sr to segregate through cathode surface has been found to be reduction in elastic energy originated from cation size mismatch [84]. Sr has higher ionic radius and this higher radius reduces compressive strains arisen on the surface when it is excess there [87]. The other key mechanism in segregation is that excess oxygen vacancies on surface causes net positive charge there. This creates driving force for negatively charged dopant to migrate to surface [20], which constitutes the electro-static aspect of origin of Sr segregation problem.

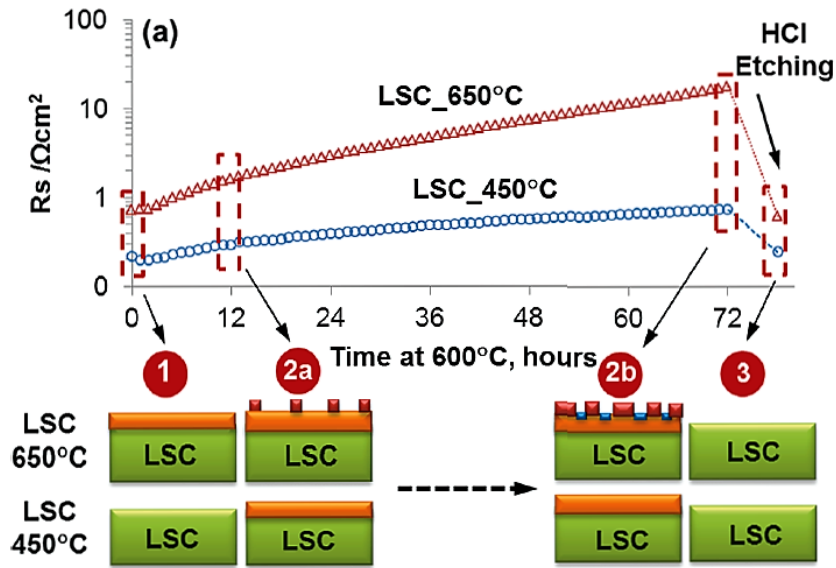


Figure 2-7 Drastic ASR change as a function of time at different temperatures.

Green represents stoichiometric bulk LSC, orange denotes Sr enriched regions and red boxes symbolize segregated and separated SrO-rich phase [18]

Now it can be again observed that cation segregation, one of the most important chemical stability problems, is directly relevant to structural stability phenomena; it is directly originated from structural instability determined from cation size differential.

It has been found that temperatures at above 400 °C, surface Sr segregation is unavoidable whether fast or slow [11,18,75]. Thus, in order for successful utilization of LSC, reducing temperature to 400 °C, seems to be necessary. This requires extreme maximization of highly active interfaces on the surface. That constitutes the basis on which this thesis has been constructed. Further insight on this segregation phenomenon has been gained by simulation studies, too [68,85,88].

At this point it is meaningful to emphasize the very promising approach having potential to get rid of surface chemical instability problem regarding perovskites, which is simply doping perovskites surfaces with various cations. Tsvetkov *et al.* [19] dipped LSC thin films into $TiCl_4$ solution, which resulted in Ti deposition on the surface, and it has been found that Ti modification of the surface has significantly reduced Sr segregation phenomenon, enhancing cell stability significantly. The

starting point is the fact that surface Sr segregation is caused by elastic energy differential between surface-bulk and electrostatic equilibrium [84]. Accordingly, types of cations by which perovskites surfaces are modified in order to reduce driving force of Sr to segregate can and will be extended. However, this approach is highly new in literature and there is, for now, lack of comprehensive understanding [19].

To sum up, it can be seen that state-of-the art cathode materials are prone to rapid degradation by various mechanisms. No matter from exactly what source the instability is originated, it is drastically affected by temperature. This can be elemental reactivity, poisoning of components, segregation and/or coarsening. The net result is that temperature reduction is the main objective of SOFC researchers.

2.2.3. Coefficient of Thermal Expansion

On one hand, decreasing the thickness of components of SOFC is dictated by the reduction of cell resistance, on the other, as thickness of cathode decreases, any probable CTE mismatch between cathode and electrolyte becomes more and more crucial. Such a mismatch can lead to easily cause cracks and delamination on the cathode [89,90].

Among state-of-the art cathode materials, Co is responsible for high CTE (see Table 2-1). Ferrites follow cobalt containing perovskites and the lowest CTE is found in manganite perovskites. But the key is matching of CTE between cathode and electrolyte. Cobalt containing perovskites generally give twice as much as electrolyte materials (see Table 2-1 and Table 2-2). The best matching is observed between state-of-the art electrolytes and manganese containing perovskites.

At this point, it is remarkable to point out that lattice expansion can be originated from two reasons; linear thermal expansion characterized by CTE and chemical expansion [45,97]. Linear CTE is determined by electrostatic forces within lattice in ionic crystals. If attraction force between atoms is reduced and/or interatomic distance is raised, then CTE gets bigger. In case of Co, this interatomic distance is more since Co has relatively lower ionic radius [45,98] (see Table 2-3) causing higher linear CTE. On the other hand, as a strong function of oxygen non-stoichiometry (δ), chemical

expansion part releases at elevated temperatures, resulting from excess reduction of B-site cation and corresponding excess anion vacancy formation [97,99].

Table 2-1 An overview to CTE of cobaltite, ferrite and manganite cathodes of SOFC

	CTE ($\times 10^{-6} \text{ K}^{-1}$)	T ($^{\circ}\text{C}$)	Ref
(La_{0.6}Sr_{0.4})CoO₃	20.5	800	[45]
(La_{0.8}Sr_{0.2})CoO₃	19.1	800	[91]
(La_{0.8}Sr_{0.2})(Co_{0.2}Fe_{0.8})O₃	15.4	600	[92]
(La_{0.8}Sr_{0.2})(Co_{0.8}Fe_{0.2})O₃	20.1	600	[71]
(Ba_{0.5}Sr_{0.5})(Co_{0.8}Fe_{0.2})O₃	20	500	[16]
(Sm_{0.5}Sr_{0.5})CoO₃	20.5	700-900	[93]
(La_{0.7}Sr_{0.3})(Co_{0.8}Fe_{0.2})O₃	21	800	[61]
(La_{0.8}Sr_{0.2})FeO₃	12	750	[94]
(Pr_{0.5}Sr_{0.5})FeO₃	13.2	550	[44]
(Pr_{0.8}Sr_{0.2})FeO₃	12.1	800	[44]
(La_{0.8}Sr_{0.2})MnO₃	11.8	900	[95]
(La_{0.6}Sr_{0.4})MnO₃	12.7	800	[96]
(La_{0.7}Sr_{0.3})MnO₃	11.7	800	[59]
(Pr_{0.7}Sr_{0.3})(Co_{0.2}Mn_{0.8})O₃	11.1	800	[45]

It should be emphasized that CTE is an indirect function of electrical conductivity. Ullmann *et al.* [45] has been manifested this. When B-site cation in perovskites is easily reducible one, which is the main reason for improved electrical conductivity, a further increase in oxygen non-stoichiometry takes place at increasing temperatures since B-site has easily been reduced to lower valence states at this condition [92].

Table 2-2 An overview to CTE of state-of-the art electrolyte materials for SOFC

	CTE ($\times 10^{-6} \text{ K}^{-1}$)	σ_i (S/cm)	T ($^{\circ}\text{C}$)	Ref
(Ce_{0.8}Gd_{0.2})O_{1.9}	13.5	0.053	800	[5]
(Ce_{0.8}Sm_{0.2})O_{1.9}	12.2	0.095	800	[13]
(La_{0.9}Sr_{0.1})(Ga_{0.8}Mg_{0.2})O₃	10.7	0.1	800	[100]
(Zr_{0.85}Y_{0.15})O_{1.9}	10.5	0.03	800	[38]
(Zr_{0.85}Sc_{0.15})O_{1.9}	10.7	0.13	800	[38]

Since Co is more easily reducible than for instance Fe [67,101], LSC has higher CTE and higher oxygen non-stoichiometry than LSF and/or LSCF as well as it has higher electrical conductivity. Manganites, in this way, are poor ionic conductors since stable valence state of Mn is +4 in wide intermediate range of T and P_{O_2} but are very good in CTE match [102,103]. The negative CTE effect of Co, the one giving the best mixed conduction, nevertheless, has been tried to be limited by B-site substitution by Fe. But this inversely affects the electrical conduction [71]. Consequently, use of LSC and LSCF have been restricted in spite of their extraordinary electrical and ionic conductivity.

So, it is understood that if high electrical conduction from MIEC cathode is preferred, which is necessary to catalyze O_2 reduction, it is necessary to consent high CTE. This rule is valid also for ionic conductivity in MIEC perovskites (not purely ionic conductors). As Ullmann *et al.* [45] manifested, pure ionic conductors deteriorate the common correlation among CTE and ionic conductivity.

In electrolyte perovskites in which there is almost no electrical conduction, excess loss of oxygen is already a reason for higher CTE [104]. In case of MIEC perovskites, additional CTE enhancement is brought about by easy reducibility of B-site cation manifested also as electrical conductivity. This is because electrolyte materials are not perovskite in which there is a competition between charge compensation mechanism with respect to T and P_{O_2} such that higher T and lower P_{O_2} mean ionic charge compensation rather than electrical. In electrolyte material, this charge compensation regime differentiation is not observed in mentionable manner as a result of different T and P_{O_2} regimes since they are not MIEC oxides and viable charge compensation mechanism is ionic compensation [35].

Despite of this restriction of LSC and LSCF (cobalt containing perovskites in general), they have always been the focus of researches because of their unprecedented ionic and electronic conductivities such that their ionic conductivity (LSC- 0.22 Scm^{-1} at 800°C [105]) for example even more than some of electrolyte materials (YSZ- 0.03 Scm^{-1} at 800°C [38]). In this way, high CTE is inevitable for LSC/LSCF but its tremendous effects can be eliminated by making it operative at low temperature applications, which has been the main focus of investigations regarding LSC/LSCF and many other

MIEC perovskites. If utilization of LSC₁₁₃/LSC₂₁₄ hetero-interface in this study, for instance, enables operation of SOFC at 400-500 °C interval, CTE mismatch between GDC electrolyte and LSC may not lead crack formation or delamination on cathode [90,106]. In terms of CTE, that is the main motivation.

2.3. An Overview to State-of-The Art Cathodes

There is no doubt that almost all properties of MIEC perovskites are result of B-site cation type and they can only be tailored through A-site. In this way, the most popular MIEC perovskites can be classified into three group namely manganites, cobaltites and ferrites or mixing of them in terms of their B-site cations, that determine eventual properties of cathodes. A-site is generally rather a matter of adjusting Goldschmidt tolerance along with deteriorating charge balance. Prior to going further into LSC_{113/214}, it would be helpful to briefly review these materials.

2.3.1. (La_{1-x}Sr_x)MnO_{3+δ} (LSM)

The most exceptional property of LSM is its good electrical conductivity (depending upon Sr doping degree) having to 300 S/cm at 900 °C well higher than 100 S/cm threshold. Even in the case of LaMnO₃ where no divalent cation (Sr for example) substitution takes place, electrical conduction is observed. This is because of instability of Mn³⁺ resulting in disproportionation of it into Mn²⁺ and Mn⁴⁺ [107]. This provides available sites for electron/hole hopping mechanism [108]. Not only disproportionation but also intrinsic electronic structure properties resulting from crystal structure is effective in creation of electrical conduction [109].

The key here is not this electrical conductivity, rather it is the fact that such good electrical conductivity is accompanying its very low CTE (~11x10⁻⁶ K⁻¹ [13]) matching well with the optimum electrolyte material YSZ. LSM is also compatible with GDC and LSGM as well as YSZ electrolytes in terms of elemental reactivity and it is relatively much more stable than other cathode materials [59].

Behavior of LSM is interesting; almost all charge balance is achieved by electrical compensation in LSM. Hence, LSM is poor ionic conductor (~6x10⁻⁷ S/cm even at

900 °C [110]) and as opposed to other perovskites for cathode, electrical conductivity increases at increasing temperatures with the p-type conductivity [59]. This is due to its different defect structure; LSM can accommodate both oxygen deficient and oxygen excess regimes depending on oxygen partial pressure. In normal working media of SOFCs, oxygen excess regime prevails [109,111,112]. Since excess oxygen cannot reside interstitially due to the fact that LSM has a close-packed structure, cation vacancies are formed to satisfy charge neutrality destroyed by the existence of Sr at A-site [59]. Thus, in fact, there is no any other oxygen apart from the ones residing normal oxygen sites of perovskite. What makes $\delta > 0$ in $(La_{1-x}Sr_x)MnO_{3+\delta}$ is the deficiency in cations. Vacancies of which cations are dominant is still debatable [8].

If it is considered that electrochemical reduction of oxygen takes place at TPB, it is seen that LSM is poor in enhancing TPB as single phase material. That is, for extension of TPB and reducing cell resistance, an additional ionic conductivity is required which is not the case for LSM alone. Hence it is generally used as composite form with additional ionic conductor such as YSZ [50].

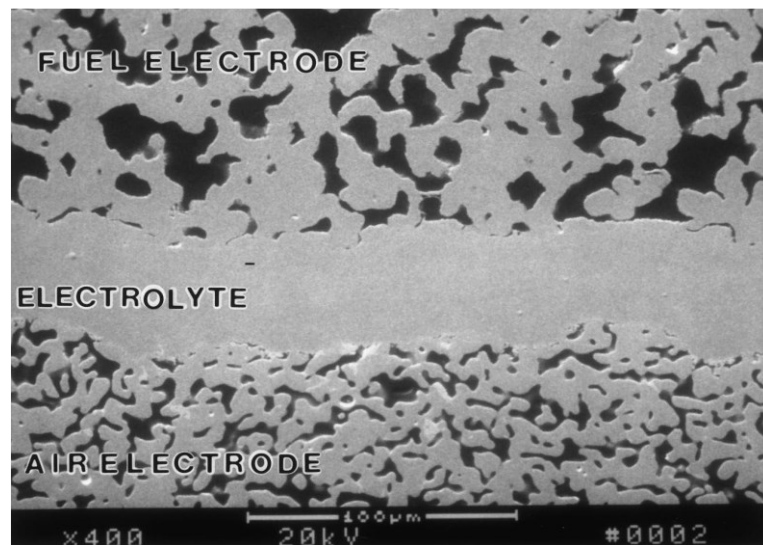


Figure 2-8 Cross sectional image of Siemens/Westinghouse SOFC in which LSM is used as cathode (air electrode) [3]

Simultaneous existence of performance stability, low CTE and good electrical conductivity as well as catalytic activity have made LSM only *conventional* cathode material for SOFCs which has been first utilized by Siemens in 1997 [113,114]. In experience of Siemens/Westinghouse, they used YSZ as electrolyte, LSM as cathode and Ni-YSZ cermet as anode. This cell operating at 1000 °C yielded 46% conversion efficiency, 0.1% performance degradation per 1000 hours over successful operation for 16600 hours [17,114] and no delamination up to 100 times thermal cycles [3].

These statistics are excellent and represent a successful SOFC operation. But still very high cost has been problem. Lowering temperature will enhance lifetime of SOFC, commercializing SOFC by virtue of making it cheaper. However, decreasing temperature drastically restricts electrical conductivity and increases ASR of LSM cathode whereas temperature reduction is a must to overcome short term degradation problems. Thus, LSM is not a suitable candidate for *intermediate* temperature SOFCs dictating the use of different alternatives. For further information about LSM, reader can refer to highly comprehensive review on LSM given by Jiang [59].

2.3.2. (La_{1-x}Sr_x)CoO_{3-δ} (LSC)

Sr doped lanthanum cobaltite (and cobalt containing perovskites in general) is the best material in terms of electrical and ionic conductivities among all alternatives and it has the highest oxygen exchange coefficient after BSCF and Sr(Co_{1-y}Fe_y)O_{3-δ} [6,42,46]; Sase *et al.* [15] reported $2.1 \times 10^{-8} \text{ cm/s}$ at 500 °C at ambient P_{O_2} for (La_{0.6}Sr_{0.4})CoO_{3-δ}, which is very remarkable among state-of-the art SOFC cathode materials. However, existence of Co as B-site cation yields more than $21.3 \times 10^{-6} \text{ K}^{-1}$ CTE, which is twice as much higher than common electrolyte materials (see Table 2-2). Moreover, use of LSC necessitates use of for instance GDC as electrolyte since LSC has reactivity problem with YSZ as explained previous section [78].

As explained previously, electrical properties are originated from the type of B-site cation, crystal structure of perovskite (O-B-O bond angle) and interaction of atoms and their orbitals (electronic structure) within this crystal structure, which is in turn a function of ionic radii. If it is considered that cobalt containing perovskites are

definitely the best ones amongst all in terms of both ionic and electrical conductivities and the worst one in terms of CTE compatibility [74], underlying reasons should be sought in these relations.

CTE is strong function of A-O and B-O bond strength [12,104]. Many of the studies state that high CTE of LSC is due to its high ability of it to create oxygen vacancies originated from promotion of the reduction from Co^{+4} to Co^{+3} . Since Co^{+3} has higher ionic radii, B-O bond strength is reduced, increasing eventual CTE [98,105]. However, asserting the reverse relationship may be possible also; since the most unstable abnormal valence (+4 state) is found in Co among Co, Fe and Mn, it has the highest tendency towards achieving its normal valence state which is +3 [101]. For instance, +4 valence state of Mn has been found to be stable till 850 °C [101] explaining the reason why Mn is oxygen excess rather than oxygen deficient in wide range of T and P_{O_2} . Teraoka *et al.* [101] have reported that Fe is superior in oxidizing, i.e. changing its trivalent state to tetravalent state. Eventually, since Co has the highest tendency towards reduction to trivalent state, it has the lowest activation energy for vacancy formation, resulting in CTE enhancement indirectly [12].

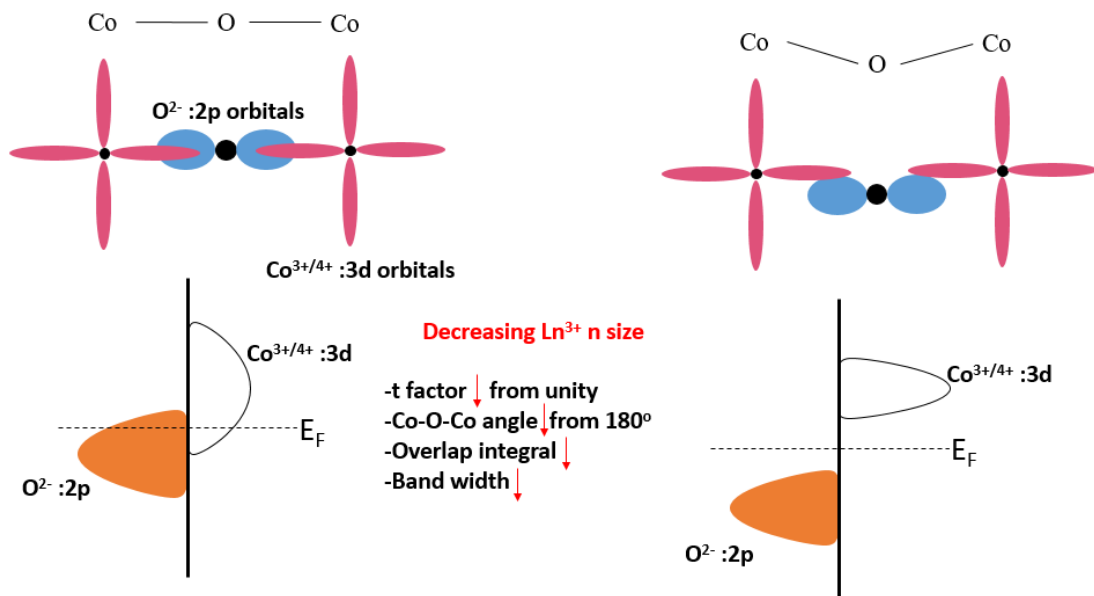


Figure 2-9 Illustration of Co-O-Co bond angle change effects on electronic structure (adapted from [103])

So, as well as high CTE, this relationship also explains the extraordinary ionic conductivity providing that crystal structure effect is not considered; higher reducibility means higher capability to create oxygen vacancies [115,116]. If structural stability (crystal structure) is considered, higher MIEC is brought about by higher symmetry and/or limited distortion on BO₆ octahedron due to its effect of diffusing jump [71]. One should also note that surface oxygen exchange properties are also a function of adsorption desorption properties of materials which is in turn related with the capability of creating oxygen vacancy [27]. So this also explains the high exchange constant of LSC by part.

However, extraordinary electrical conductivity still needs further explanation. What happens in LSC is simply overlapping of 3d orbitals of Co and 2p orbitals of oxygen. When it takes place, band width is reduced and electrical conductivity via “itinerant” (delocalized) electrons is promoted as illustrated in Figure 2-9. This brings about metallic conduction behavior surely depending upon Sr doping degree [6]. Metallic conduction behavior is something uncommon among perovskite oxides. This overlap is definitely very strong function of Co-O distance and hence crystal structure as Mineshige *et al.* [64] pointed out. Different structures mean different degree of overlap and Co-O-Co bending, latter of which is functional in hopping conduction while former is important for releasing of itinerant electrons and metallic conduction. For various A-site cations, crystal structure of perovskite is orthorhombic if Sr doping degree, x, is small but when it is La, structure is rhombohedral at low x and cubic at high x, making LSC superior in electrical conductivity [12,103]. Thus, the crystal symmetry as well as inter-atomic distance within crystal are the main variables determining the eventual electrical conduction.

Table 2-3 Ionic radii of Co⁺³, Mn⁺³ and Fe⁺³ at different spin states [98]

Ionic Radius in BO₆ Coordination and +3 Valence (Å)			
Atom	Mn	Fe	Co
Low Spin	0.58	0.55	0.545
High Spin	0.645	0.645	0.61

But at this point, it should be highlighted that those variables are also functions of ionic radii, or equivalently atom types that determine covalency of B-O bonds considered to be crucial electronic conduction through BO_6 chains [71]. Higher covalency is expected in case of smaller cation, higher anion size and more positively charged cation. These characterize covalency by virtue of their ability to determine polarizing power of cation. In this way, Goldschmidt asserts a way to measure polarizing power by Coulomb potential denoted as Ze^2/r_B where Z is formal valence of cation, e is elementary charge and r_B is ionic radius of B cation [70]. Higher charge on B-site cation with a small radius as well as lower Z_A/r_A promote polarizing power and so covalency [71]. For the same valence state, Co has lower ion size and higher covalency as can be inferred from the Table 2-3 given. Now one can infer at this point that high CTE can be tuned by altering A-site cations even in the presence of Co as B-site since Z_A/r_A is also a variable. In this way it is suitable to consider A-site atoms as the way of providing ionic network stabilizing BO_6 octahedron through which conduction takes place.

At low temperatures, polarizing power of Co is higher since it has +4 valence state and lower ionic radius. However, this covalency and electrical conductivity is drastically deteriorated at higher temperatures and low P_{O_2} due to the increase in the number Co^{+3} ions resulting from domination of ionic compensation mechanism. Furthermore, as a new fact in LSC, an additional reduction in Coulomb potential is caused by spin state transition of Co^{+3} ions unlike to Mn^{+3} and Fe^{+3} which are keeping their high spin states [116,117]. For Co^{+3} ions, from low spin (t_{2g}^6, e_g^0) to intermediate (t_{2g}^5, e_g^1) or high spin (t_{2g}^4, e_g^2) is seen in cobaltites [116,118]. Extreme increase in CTE of LSC can be partly attributed to this effect, too [12]. At this point, in order to inform reader, it would be good to point out that even at low temperatures, electrical charge compensation can only dominantly be operative when $x < 0.4$ in $(\text{La}_{1-x}\text{Sr}_x)\text{CoO}_{3-\delta}$ and more Sr doping leads to vacancy formation even at low temperatures [103].

Exceptional electrical and ionic conductivities together with catalytic activity of cobalt containing perovskites necessitated relatively long explanation for formation of them. But in evaluation of cathode materials, it is better to use ASR data in the time domain,

that is its stability. In terms of ASR values, the lowest value obtained from pure LSC₁₁₃ reported to date is 0.023 Ωcm² at 600 °C [119–121]. Some other values have been summarized by Kilner *et al.* [14] as illustrated in Figure 2-10.

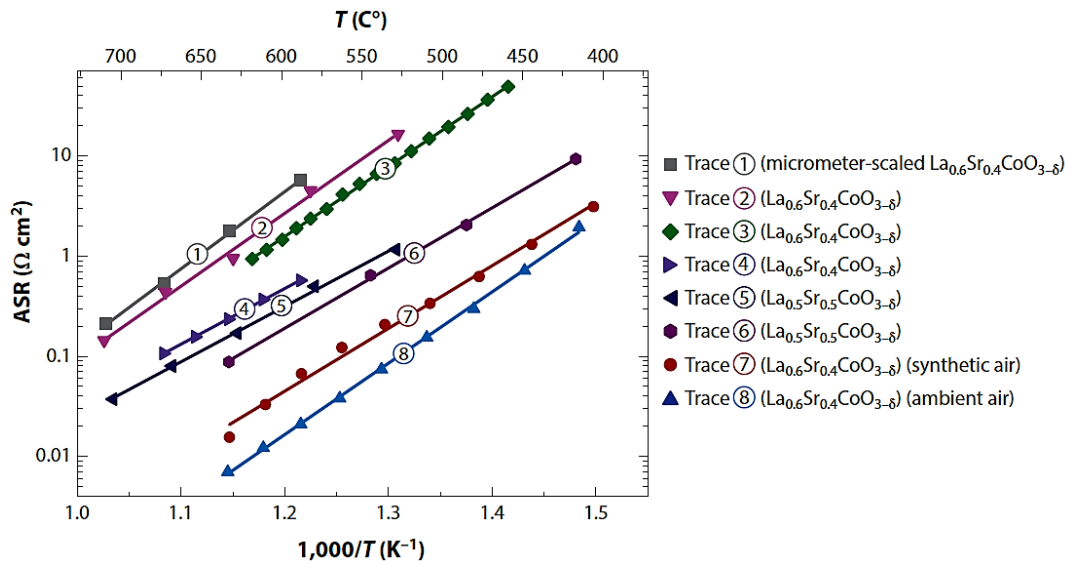


Figure 2-10 ASR of LSC in different studies (retrieved from [14,122])

Such extremely low polarization resistances are not surprising regarding extraordinary properties of LSC. However, all these properties and exceptional ASR are at the cost of instability of LSC. Unfortunately, LSC derivatives are highly susceptible to short term degradation especially by means of surface Strontium segregation [9]. Even after several days, SrO_x formation on the air exposed surface blocks ORR and this is inevitable whether slow or fast so long as temperatures above 400 °C [9,11,18]. Recently, surface modification with some metals inhibiting Sr segregation has been adopted as a way to eliminate this problem and make the use of LSC at intermediate temperatures possible for long term use [87].

Whereas high CTE and chemical instability are extremely significant obstacles for use of LSC, its extraordinary electrical and ionic conductivities are such that its ionic conduction is sometimes more than the state-of-the art electrolyte materials still attracts the attention.

2.3.3. (La_{1-x}Sr_x)FeO_{3-δ} (LSF)

The driving force for transforming B-site cation from Co to Fe is the high CTE of LSC. By replacing Co with Fe significantly reduces CTE to state-of-the art electrolyte values ($12 \times 10^{-6} \text{ }^\circ\text{K}^{-1}$ [94]) due to higher stability of +3 state of Fe [101] but it also reduces both electrical and ionic conductivities drastically because of the absence of Co. Nevertheless, electrical conductivity of various Sr compositions in LSF is still higher than 100 S/cm at intermediate temperatures converging lower limits [58] as well as its significant vacancy amounts manifested as oxygen diffusivity [60]. Electrical conduction occurs only via hopping mechanism unlike to cobaltites. What's more, LSF has almost same catalytic activity as LSC towards ORR depicted by surface exchange coefficient k^a ; both has around 10^{-6} cm/s exchange coefficient at 750 °C depending upon Sr and P_{O_2} [15,46,123] with well smaller activation energy for LSC [22].

By virtue of LSF, 0.1 Ωcm^2 at 800 °C is achieved when x was 0.2 [124,125]. This cell was operated 500 hours without any performance degradation. At this same composition of LSF, Simner *et al.* [94] reported more than 0.9 W/cm² peak power densities for 300 hours stable performance at 750 °C. The lowest possible temperature, however, seems to be 676 °C yielding 0.168 Ωcm^2 as reported in the study by Leonide *et al.* [123] in which La deficiency at A-site was adopted to facilitate the overall kinetic. Beyond all of these promising performances, the most remarkable advancement that LSF has been the efficiently matched CTE with YSZ electrolyte [126].

Even though kinetic of it is significantly reduced with Fe as B-site cation, reactivity problem with YSZ is the same as LSC. But in this case, reactivity is in the form of Zr and La inter diffusion and incorporation of Zr into B-site [125,127–129] rather than lanthanum zirconate formation [124]. In this way, LSF is not free from performance degradation over time like LSC [94]. However, this problem can be significantly overcome by the help of implementing ceria based protecting barrier onto YSZ electrolyte or direct use of them [130].

Thus, LSF seems to be a suitable candidate for intermediate temperature SOFC in terms of cathode resistance and CTE match. The best composition reported is $(\text{La}_{0.8}\text{Sr}_{0.2})\text{FeO}_{3-\delta}$ [94]. However, 700 °C seems to be the lowest possible operation temperature in its single phase utilization if it is considered that $0.15 \Omega\text{cm}^2$ is targeted ASR value and this temperature is still a source of problem regarding interconnect materials [131]. Furthermore, long term performance degradation is still a problem in LSF. There is still lack of comprehensive long term performance tests in literature.

2.3.4. $(\text{La}_{1-x}\text{Sr}_x)(\text{Co}_{1-y}\text{Fe}_y)\text{O}_{3-\delta}$ (LSCF)

Fe has been observed to be very effective in optimization CTE match with electrolytes along with preservation of conductivity thresholds. Nevertheless, operation temperature is still behind the expectations. Hence, partial substitution of B-site by Co was adopted an alternative way for further optimization. Coexistence of cobalt and iron may well converge the performance of LSF to LSC along with minimizing the drawbacks of LSC such as high CTE.

Indeed, this approach brought about superior performance with respect to LSF. LSCF shows wide variations of performances as function of both A and B-site doping degrees. Petric *et al.* [61] observed increasing CTE as well as MIEC with increasing Co content. Hence, only small extend of Sr and Co doping are acceptable in terms of conservation of reduced CTE of LSF in the acceptable ranges. Some compositions and corresponding properties are given in Table 2-4.

Table 2-4 CTE, electrical and ionic conductivities of various LSCF cathodes

	CTE (10^{-6} K^{-1})	σ_e (S/cm)	σ_i (S/cm)
$(\text{La}_{0.8}\text{Sr}_{0.2})(\text{Co}_{0.2}\text{Fe}_{0.8})\text{O}_{3-\delta}$	14.8 [45]	125 (600 °C [132]) 87 (800 °C [45])	0.0022 (800 °C [45])
$(\text{La}_{0.6}\text{Sr}_{0.4})(\text{Co}_{0.2}\text{Fe}_{0.8})\text{O}_{3-\delta}$	15.3 [132]	300-330 (500-750 °C [14])	0.008 (600 °C [13])
$(\text{La}_{0.8}\text{Sr}_{0.2})(\text{Co}_{0.8}\text{Fe}_{0.2})\text{O}_{3-\delta}$	20.7 [92]	1050 (600 °C) [92]	0.04 (800 °C) [61]
$(\text{La}_{0.8}\text{Sr}_{0.2})(\text{Co}_{0.5}\text{Fe}_{0.5})\text{O}_{3-\delta}$	17.6 [61]	354 (800 °C) [45]	-

Along with the properties given in Table 2-4, even in case of $(\text{La}_{0.6}\text{Sr}_{0.4})(\text{Co}_{0.2}\text{Fe}_{0.8})\text{O}_{3-\delta}$, in which there is high iron content, diffusivity and exchange coefficients are almost the same as LSC [71]. This overall picture suggests that LSCF can be treated like LSC but together with reduced CTE. However, the most explicit parameter for evaluation of suitability of a material is the desired ASR at given temperature and stability.

In this way, various attempts have been made for utilizing LSCF cathodes in SOFC stacks. At this point, it is remarkable that when LSCF cathodes are in thin dense film form, they show so high ASR that its use becomes impossible even at around 800 °C. Figure 2-11, belonging to the study in which cathodes are derived via PLD [133,134] and sputtering [135] is a good illustration of this. As can be seen, even at 800 °C and high Co content, targeted ASR value ($0.15 \Omega\text{cm}^2$) is not achieved, which is even worse than LSF cathodes.

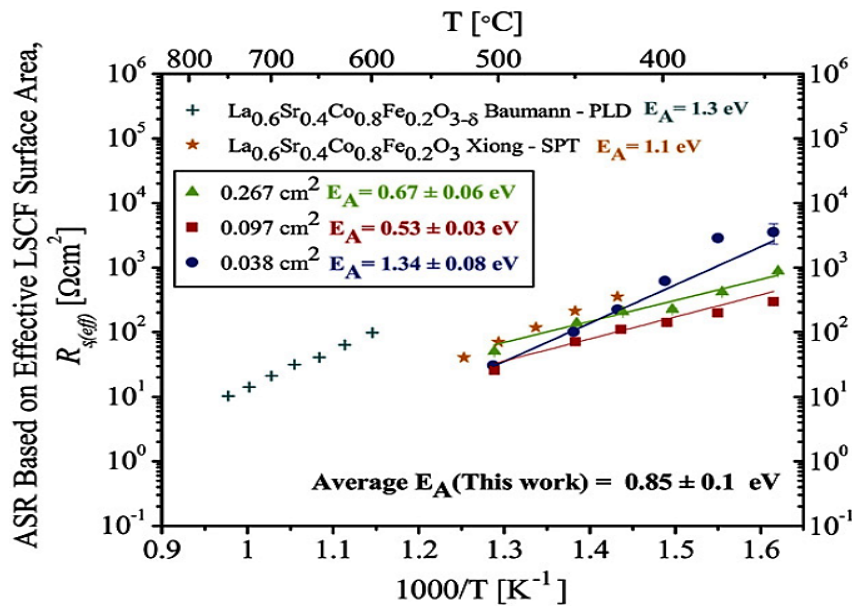


Figure 2-11 ASR values of various LSCF dense thin films. Figure is retrieved from ref [134]. Data in the box is from ref [134]. Data from Baumann *et al.* [133] and Xiong *et al.* [135]

Ralph *et al.* [124] utilized porous LSCF cathodes having approximately 200 μm thicknesses. They used Fe rich compositions and reported around $0.2 \Omega\text{cm}^2$ at 700 °C.

This is remarkable as compared to dense thin film results. As the latest, porous $(\text{La}_{0.58}\text{Sr}_{0.4})(\text{Co}_{0.2}\text{Fe}_{0.8})\text{O}_{3-\delta}$ has been found to exhibit $0.13 \Omega\text{cm}^2$ ASR at 600°C , which is the lowest reported value to date [136]. In this study, A-site La deficiency was adopted. Nevertheless, LSCF suffers from severe performance degradation over time namely 0.05% per hour [137].

Aside from existence of abovementioned parameters, mechanisms with which they occur as functions of T and P_{O_2} are quite complicated since in ferrites, n and p-type conductivities are observed while cobalt as B-site cation induces metallic conduction behavior due to itinerant electrons of it. So, it is not reasonable to sum up with certain tendencies as function of T and P_{O_2} especially in terms of conductivities.

2.3.5. $(\text{Ba}_{1-x}\text{Sr}_x)(\text{Co}_{1-y}\text{Fe}_y)\text{O}_{3-\delta}$ (BSCF)

BSCF is very recent and definitely the best choice in terms of both surface oxygen exchange rate [138,139] and bulk transport [140] manifested as k and D respectively. The most distinguishing character of BSCF is the fact that both of A-site host and dopant atoms are alkaline earth elements having +2 valence (Ba and Sr) as opposed to other types of perovskite alternatives in which A-site host atom is rare earth element namely La. In conventional perovskite complex oxides, A-site is doped with a cation having different valence state than host atom resulting electrical conduction as explained in previous pages. Due to the same valence state at A-site (Ba and Sr) electrical conductivity of BSCF is relatively low (30 S/cm at 500°C [16]) as compared to other cathode materials (as stated in page-11 previously, 100 S/cm electrical conductivity is considered to be lower threshold). However, this is compensated by extraordinary k and D values of BSCF introduced by better oxygen vacancy mobility than others [27,46,140].

The first attempt to substitute BSCF as SOFC cathode was done by Shao and Haile [139]. As consequence of its extraordinary surface exchange and transport properties found in this study, $0.055\text{-}0.071 \Omega\text{cm}^2$ and $0.51\text{-}0.60 \Omega\text{cm}^2$ cathode resistance at 600 and 500°C could be achieved, respectively. These excellent results attracted significant attention, making BSCF focus of many researches [138,141–143]. It can

be deduced from all these studies that magnificent properties of BSCF are directly proportional to Ba and Co content; Ba doping to A-site stabilizes the structure by virtue of making Goldschmidt tolerance to unity (cubic structure).

The latest and the most comprehensive study concerning BSCF has been conducted by Kuklja *et al.* [27] by help of *ab initio* simulations as well as experimental approaches. The A and B site composition combination giving the best results associating the best performance has been found to be with $(\text{Ba}_{0.5}\text{Sr}_{0.5})(\text{Co}_{0.8}\text{Fe}_{0.2})\text{O}_{3-\delta}$. This is because this x and y values combination gives the highest oxygen deficiency and resulting the highest surface exchange constants. These superiorities in terms of transport and surface exchange properties are originated from excess oxygen deficiency as well as superior vacancy *mobility* of BSCF over all other cathode materials. However, this high oxygen deficiency makes this best composition fall into immiscibility region of cubic and hexagonal structures, causing phase instability in case of superior BSCF [144].

In long term, phase decomposition will dictate itself and such a decomposition reduces both k and D. Definitely, adjusting A/B-site compositions and so converging oxygen deficiency to unity would suppress phase instability but this time advantageous properties of BSCF can't be utilized.

Another drawback of BSCF that must be concerned is carbonate formation below 900 °C not only with YSZ but also in case of GDC electrolyte [27,142]. Moreover, at temperatures exceeding 800 °C, reactivity with YSZ begins [14]. High CTE of BSCF like all Cobalt containing perovskites is also a problem even BSCF is capable of being operated at 600 °C.

To sum up, similar to other cathode materials whose eventual properties are originated from crystal structure-atom type combination, superior properties of BSCF are commonly referred to well-known size mismatch between A and B site atoms. What is new in BSCF is that it can withstand cubic structure for short period as opposed to state-of-the art cathode oxides, giving extraordinary performance whereas for long term applications, but it is well suspected to degrade by virtue of its decomposition into cubic and hexagonal structures [27,144].

2.3.6. Ruddlesden-Popper (A_2BO_4) Type LSC_{214}

The key property of $(La, Sr)_2CoO_{4+\delta}$ or A_2BO_4 type structures in general is the ability to form interstitial oxygen atoms at rock salt layer even without need to A-site doping. This is manifested as oxygen excess regime in wide range of T and P_{O_2} resulting in high diffusion coefficients [145].

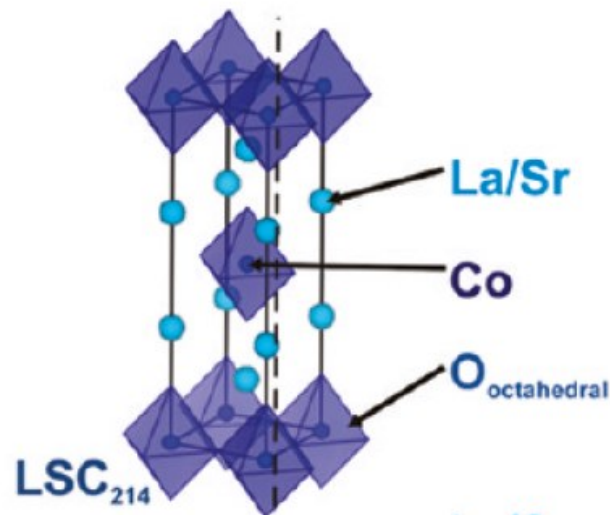


Figure 2-12 Ruddlesden-Popper (K_2NiF_4 type) LSC_{214} Structure [21]

$(La_{1-y}Sr_y)_2CoO_{4+\delta}$ belongs to this family. Its crystal structure is tetragonal for $0.3 < y < 1$, comprising a rock salt layer sandwiched between two perovskite layers [72] as illustrated in Figure 2-12. That's why it is also called layered perovskite [146].

Consequently, oxygen migration is significantly facilitated even without need for A-site substitution ($La_2CoO_{4+\delta}$ here), which is responsible for chemical and structural instability problems in conventional perovskites. Superior chemical stability of $La_2CoO_{4+\delta}$ hence makes stoichiometric Ruddlesden-Popper structure advantageous over conventional SOFC cathode materials by virtue of its ability to enhance long term stability by suppressing poisoning and cation segregation [27]. Munnings *et al.* [147] reported surface exchange coefficient around $10^{-5} - 10^{-6} \text{ cm}^2/\text{s}$ at between 500-700 °C and diffusivity around $10^{-7.5} \text{ cm}^2/\text{s}$ at 650 °C for $La_2CoO_{4+\delta}$. These values are promising but stoichiometric LSC_{214} ($La_2CoO_{4+\delta}$) is highly poor in terms of electrical conductivity such that $La_2CoO_{4+\delta}$ has reported to give less than 1 Scm^{-1} electrical

conductivity at 500 °C [148]. Electrical conductivity rapidly increases with increasing Sr doping, [149] but it reaches to at most 50 Scm⁻¹ when it is LaSrCoO_{4+δ} [150].

Considering Sr doped La₂CoO_{4+δ}, good diffusion property is accompanied with only moderate electrical conductivity, which is function of Sr doping [148,150]. However, higher Sr amount corresponds to reduction on surface exchange kinetic as recently demonstrated even more drastically than crystallographic orientation by virtue of their ability to enhance surface Sr segregation shadowing orientation effect [75].

It should be kept in mind that depending upon Sr doping degree, oxygen stoichiometry varies. To be valid at ambient P_{O_2} and intermediate T range, for relatively low Sr, LSC₂₁₄ accommodates oxygen interstitials (oxygen excess regime) while at increasing Sr degree, it transforms to be oxygen deficient making vacancy mechanism dominant [151]. The statement “low Sr doping” covers $y=0.5$ in (La_{1-y}Sr_y)₂CoO_{4±δ}, yielding oxygen excess regime in (La_{0.5}Sr_{0.5})₂CoO_{4+δ} [152]. This regime is mainly responsible for high diffusivity in Ruddlesden-Popper type structure in general.

In addition, serious anisotropy is observed in this structure especially in terms of both diffusivity and CTE [153–155]. Surface exchange kinetic has not been extensively studied till now. Along with this, high CTE is a problem for LSC₂₁₄ due to existence of Co ions as opposed to Ln₂NiO_{4+δ} (Ln denotes lanthanide elements namely La, Ce, Pr Sm Gd etc.) having relatively compatible CTE for example [155]. Similar to LSC₁₁₃, LSC₂₁₄ is also not free from surface Sr segregation [75]. So, LSC₂₁₄ brings about the problems related to existence of Co. LSC₂₁₄ is only differentiated in terms of its high and *anisotropic* D and k values and significantly reduced electrical conductivity.

In terms of ASR, as the most viable parameter in evaluating SOFC cathodes, LSC₂₁₄ as well as Ruddlesden-Popper type oxides seem to be unsuitable for intermediate temperature range as a single phase component [146,156]. The best one among Ruddlesden-Popper type oxides is Pr₂NiO_{4+δ} yielding 0.5 Ωcm² at 610 °C [157]. Nickel based Ruddlesden-Popper oxides have been widely and intensively investigated till now as opposed Cobalt based ones, especially in terms of overall SOFC cathode performance by probing ASR [36,158–160]. One of the recent study utilizing LSC₂₁₄ with different Sr dopant amount showed more than 2 Ωcm² even at

700 °C [155]. This work also exhibits ASR values obtained from sub-micron thickness LSC₂₁₄ cathodes. The probable reason for high ASR in spite of very good exchange kinetic and accompanying high diffusivity is low electrical conductivity of LSC₂₁₄, reducing TPB.

The situation for Cobalt based Ruddlesden-Popper oxide is also in a good agreement with what Laberty *et al.* [156] proposed for Ruddlesden-Popper oxides in general; they are not functional materials for SOFC cathode operation at intermediate temperatures. However, not only in composite form with different ionic conductor materials such as GDC [155], but Ruddlesden-Popper type can also be extremely functional in case of oxide hetero-structures like the case of LSC₁₁₃/LSC₂₁₄ [11,15,21]. Hence, they may not be promising candidates at intermediate temperature ranges as single phase but they might be well functionalized by use of different probable strategies. It can be stated finally that there is still lack of comprehensive investigations on K₂NiF₄ type structures as SOFC cathode materials.

2.3.7. Final Remarks Regarding State-of-The Art Cathodes

The most popular cathode materials have been introduced briefly. Although it is excluded, composite cathodes have also been an alternative. In this approach, two components, each of which has relatively high conductivity in one type and poor in the other, are combined such as LSM-YSZ cathodes [50,51,65,161]. But in this study, such an approach is treated to be contradictory to MIEC phenomena, capable of extending electrochemical reduction, to which all the high energy conversion is owed, from TBP to whole air exposed surface.

Furthermore, there are many combinations of A and B-site cations exhibiting promising performances, too [157,162–165]. These are namely Gd, Sm, Bi, Pr, Ce, Nd as A-site and Ni, Cr, Cu, Ga, Mg as B-site. But, no matter how slightly better their performance is, they also suffer from the similar drawbacks caused by their B-site cation, which is deterministic component of ABO₃ oxides. The reason why this brief review of cathode materials has been restricted to these five cathodes is because such a picture is considered to be representative to take a general look at SOFC cathodes, advantages, drawbacks and underlying reasons for their properties.

Much further tailoring is possible since all the properties are determined by the atom characteristics and their ordering type (crystallography) eventually. Much rarer elements can be replaced into these oxides but this time economic feasibility problem arises. Apart from these impractical approaches, all commercially promising possibilities per certain one kind of ABO_3 oxide seems to have been tested in terms of material properties such as exchange rate, diffusivity and conductivities. Synthesizing single phase ABO_3 oxides seem to have reached its limit in this way.

Nevertheless, various improvement routes are still open with regard to hetero structuring and surface modifications. Effect of different fabrication route and parameters for cathode as well as surface modifications are still in progress. Among them, comprehensive understanding of surface cation segregation constitutes extremely crucial task in order to get rid of surface instability problem, from which almost all A-site substituted ABO_3 oxides suffer. Likewise, ORR kinetic at around hetero interfaces is also something new in this field. Revealing the outstanding roles of such heterogeneities are still under investigation. $LSC_{113/214}$ hetero interface in this way seems to be the highly salient one among those.

2.4. LSC_{113}/LSC_{214} Hetero Interface

Extraordinary surface exchange property of LSC_{113}/LSC_{214} hetero interface has been first discovered accidentally by Sase *et al.* [15]. During this research, as a result of over sintering of $(La_{0.6}Sr_{0.4})CoO_{3-\delta}$ at elevated temperatures, LSC_{214} phase was formed accidentally. Only after the discovery of the secondary phase (LSC_{214}), hetero interface was investigated in this study by secondary ion mass spectroscopy (SIMS) and this revealed that k^* ($8 \times 10^{-6} \text{ cm/s}$) is around three orders of magnitude higher than that ($2 \times 10^{-8} \text{ cm/s}$) of $(La_{0.6}Sr_{0.4})CoO_{3-\delta}$ at the same temperature. Following studies concerning the high exchange constant of hetero interface was conducted by Yashiro *et al.* [166] and Crumlin *et al.* [21].

What Yashiro *et al.* [166] did was the examination of symmetric cells obtained via *horizontally* screen printing phases subsequently onto GDC pellet. Since in this case LSC_{113} and LSC_{214} form parallel path for electron flow, faster one in terms of

conduction will be dominating one. This is LSC₁₁₃ phase. That's why performance of cells having LSC₂₁₄ on LSC₁₁₃ (or equivalently interfacial enhancement) did have slightly better than LSC₁₁₃. Reported enhancements were around 0.5 orders of magnitude greater k^q (correlated from electrical conductivity) than LSC₁₁₃ and 1-2 orders of magnitude greater than k^q of LSC₂₁₄.

In fact, this was not the exact determination of hetero interfacial enhancement since the cell in study of Yashiro *et al.* [166] constituted parallel electron flow path. Moreover, in this study, cathodes were not in the form of thin film. Furthermore, enhancement of what Yashiro *et al.* [166] achieved was not as high as what Sase *et al.* [15] discovered. Hence, for further clarification, Crumlin *et al.* [21] obtained epitaxial thin film cathodes by PLD. They deposited LSC₂₁₄ on LSC₁₁₃ with both full coverage and partial coverage. They, accordingly, revealed active region somehow affected by TPB (LSC₁₁₃-gas-LSC₂₁₄) which was around 20 μm . When the thickness of deposited LSC₂₁₄ on LSC₁₁₃ gets increase more than only several nanometers, the ASR gets dramatically increased. In this sense, Crumlin *et al.* [21] detected 3-4 orders of magnitude enhancement in k^q which is correcting what Sase *et al.* [15] found first. Problems in measurements done by Yashiro *et al.* [166] were originated from the fact that enhancement region is very narrow as can be understood from study of Crumlin *et al.* [21] and thick cathodes were used [166]. Hence, rather than recording the enhancement just at interface, they recorded the *effect of* hetero interface in overall resistance, which was at most one order of magnitude consistently [166].

This chronology, revealing very narrow distance range [21] (1-200 nm [167]) over which enhancement was actually originated, required atomic scale characterization and understanding which is quite difficult without *ab initio* calculations. In this way, further investigations have been based on such simulations. One of the initial first principle calculations was done by Han *et al.* [151]. In their simulation, they found 400 times enhancement in oxygen reduction kinetic at 500 °C and attributed it to anisotropy in LSC₂₁₄ leading to very fast kinetic at (100) plane and lattice strain in LSC₁₁₃ phase. Nevertheless, along with underestimation of 3-4 orders of magnitude enhancement, this DFT study considers each *individual* phase rather than hetero interface as a new phenomenon as they stated [151].

First principle calculations have been accompanied by experimental studies, too. By use of grazing incidence FIB milling, which has been adopted first time by Kuru *et al.* [168], Chen *et al.* [167] probed LSC₁₁₃/LSC₂₁₄ interface and discovered electronic activation of LSC₂₁₄ by LSC₁₁₃ starting from 200-300 °C. This is illustrated in Figure 2-13.

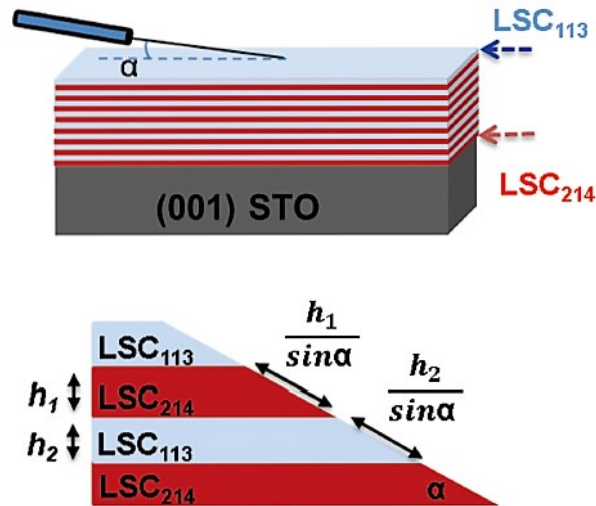


Figure 2-13 FIB milling at grazing incidence angle [169]

Wider band gap of LSC₂₁₄ is interestingly reduced when it is in contact with LSC₁₁₃ [167]. At low temperatures, charge compensation of LSC₁₁₃ phase is mainly done by partial oxidation of Co. This induces electrical conductivity and these electrons from LSC₁₁₃ phase are injected to LSC₂₁₄, which is very rich in interstitial oxygen [145] and suffering from low electrical conductivity [148,150]. Interstitial oxygen of LSC₂₁₄ can easily find electrons from LSC₁₁₃ to be more effectively reduced and adsorbed by LSC₁₁₃. But this requires empty sites for reduced oxygen to jump in LSC₁₁₃ phase. Moreover, migration of electrons through interface is supposed to bring about driving force for migration of oxygen vacancies, too. Such a migration is not however favored at lower temperatures. Increasing temperatures provides creation and mobility of oxygen vacancies for this purpose [111,147]. That's why electronic activation takes place after certain temperature range is attained, after which the combination of desirable properties of each phase results in fast oxygen reduction kinetic.

Nonetheless, whether it is capable of causing 1000 times enhancement on k at hetero interface alone or not is still question, answer of which is sought in following sections.

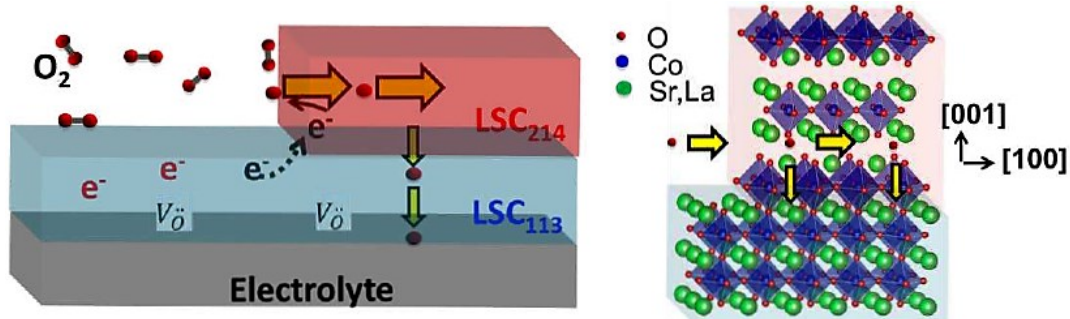


Figure 2-14 Illustration of proposed ORR mechanism for LSC₁₁₃/LSC₂₁₄ by Chen *et al.* [169]

One might at this point claim that electronic activation is observed in epitaxial film [167], LSC₂₁₄ is known to show fast oxygen reduction kinetic on (100) surfaces [158] and so electronic activation found here is plane specific [11]. However, previous studies based on both EIS [21] and SIMS [15] that are showing similar fast oxygen reduction kinetic *without* any epitaxy demonstrates that this is an intrinsic phenomenon.

Moreover, it is also notable that proposed electronic activation mechanism is deteriorated with increasing temperatures since electrical conductivity of LSC₁₁₃ phase (at least with highly Sr doped ones) is reduced with increasing temperatures [64]. However, as stated previously, fast kinetic has been reported to be at 500-600 °C, too. Whether degree of observed fast kinetic at around 200-300 °C is similar to degree of it at elevated temperature is questionable. If answer is “similar”, what triggers the same enhancement degree at the cost of lowering electrical conductivity at elevated temperatures becomes a crucial question. What happened at increasing temperatures is vacancy formation and enhanced vacancy mobility, not increase in electrical conductivity. So, activation at higher temperature should be originated from something related to vacancies if the same degree of ORR enhancement is predicted.

Gadre *et al.* [68] in this way reported strong driving force for Sr diffusion through hetero interface and corresponding La diffusion in reverse direction between $(\text{La}_{0.75}\text{Sr}_{0.25})\text{CoO}_{3-\delta}$, and $(\text{La}_{0.5}\text{Sr}_{0.5})_2\text{CoO}_{4+\delta}$ by use of DFT-based simulations. These driving forces are evaluated under different T and P_{O_2} conditions. Resultant (proposed) possible inter-diffusion across interface and Sr enrichment in LSC_{214} phase are susceptible to form excess vacancy accumulation at elevated temperature near interface in the side of LSC_{214} . However, such a vacancy accumulation near interface is only *partially* capable of reasoning the 3-4 orders of magnitude enhancement in $k^q \approx k^*$ found by Sase *et al.* [15] and Crumlin *et al.* [21] under similar experimental conditions. Nevertheless, Gadre *et al.* [68] showed that further mechanisms beyond electronic activation exist.

In study conducted by Gadre *et al.* [68], Sr enrichment in LSC_{214} is reasonably corresponds to Sr depletion in the side of LSC_{113} phase, which is supposed to significantly *decrease* oxygen vacancy concentration near interface especially in the side of LSC_{214} . Such a case (vacancy decrease in LSC_{113} side) would negatively compensate what is gained in LSC_{214} in terms of k enhancement. However, Gadre *et al.* [68] suggest that this inter-diffusion predicts slight Sr enrichment very near interface in the side of LSC_{113} , too. Consequent La accumulation is expected to occur rather at bulk of LSC_{113} , not interface. Definitely what is stated is a prediction. What is happening near this interface, especially at the side of LSC_{113} necessitates experimental and quantitative probing of this interface, which is very hard task.

Nonetheless, some of studies, which are not mainly concerned with identification of underlying reasons, qualitatively confirm the claim supporting activation mechanisms apart from electronic activation. Ma *et al.* [11] discovered that there is a significant deviation between degree of enhancement at lower temperatures; there is 3-4 orders of magnitude enhancement reported in between 500-600 °C [15,21], while this enhancement is 10 times in between 320-400 °C in their analysis [11].

This apparently means that at increasing temperatures, an additional and/or different ORR activation mechanism becomes operative, which was anticipated by Gadre *et al.* [68]. Ma *et al.* [11], however, asserts that remaining 100 times enhancement is attributed to fast oxygen incorporation kinetic along (100) plane of LSC_{214} [151],

which was parallel to cathode film surface in their experiments, consequently making utilization of its ORR superiority through [100] plane impossible. anticipate

However, it is possible to argue that even this strong explanation still underestimates the negative effect of gradually reducing electrical conductivity of LSC₁₁₃ (at higher temperatures), which is simply electron source of that composite cathode system. Attribution of this greater portion of enhancement (100 times) to anisotropy of LSC₂₁₄ phase necessitates an explanation for three orders of magnitude enhancement found in polycrystalline pellet in which no epitaxial relation probably prevails [15]. At least, the same experiment as in ref [12] based on LSC₁₁₃ pellet should be done once more prior to this assertion and nucleation-growth vs crystallography relationship of LSC₂₁₄ in LSC₁₁₃ pellet should have been clarified.

For example, owners of this assertion (Ma *et al.* [11]) did not add the information whether it nucleates-grows through certain direction during the high temperature formation of LSC₂₁₄ and enhancement is 10³ times higher, or not. Aside from this, it is already known that such giant grains [15] do not generally grow coherently with the matrix phase (LSC₁₁₃) [170] since this would extremely increase surface potential (γA). Probable incoherency at interface along with the results implying Sr migration (vacancy formation on LSC₂₁₄ part) near surface based on simulations [68] is strong indication of additional operative orientation-independent mechanisms near interface rather than plane-specific fast ORR.

Not only simulations, but also the experimental demonstration of robust Sr migration contiguous to interface and corresponding vacancy formation has been first reported by Feng *et al.* [88] on epitaxial thin film composed of LSC₂₁₄-on-LSC₁₁₃ with their coherent Bragg rod angle (COBRA) analysis by use of X-ray radiation. That has been the first implicit atomic scale and experimental characterization revealing strong Sr segregation from perovskite to Ruddlesden-Popper in this way. Not only Feng *et al.* [88] but also the same research group, having assertion based on orientation dependent k enhancement [11], has recently disclaimed by themselves in study of Chen *et al.* [75]; they ‘discovered’ orientation independent k enhancement.

To reveal underlying reasons, this interface has been aimed to be used in various studies. One of the final approach aiming interface utilization was to yield vertically

aligned epitaxial interfaces by PLD method [11]. This study yielded vertically aligned nanostructures of hetero interface in the 200-300 nm domain dimensions spatially. This corresponded to significant interface maximization. Ma *et al.* [11] in this study have found around $1000 \Omega\text{cm}^2$ ASR at 400°C in this composite cathodes including vertically aligned $\text{LSC}_{113/214}$ interfaces. This ASR value is 10 times smaller than ASR of single phase cathodes between $320\text{-}400^\circ\text{C}$ interval. Moreover, they state that 400°C is a critical threshold above which surface Sr segregation is inevitable whether fast or slow depending upon T while below this temperature surface chemical instability phenomenon is not seen. Another interesting observation that they make, hetero interface has a capability to postpone chemical degradation of surface giving a stability effect to hetero interface which was previously reported, too [85].

Crumlin *et al.* [21] also adopted epitaxial thin film cathodes of LSC_{214} -on- LSC_{113} as a function of LSC_{214} horizontal coverage of LSC_{113} surface. Their film thickness was around 50 nm, which was extremely small. What they found consequently was around $1.5 \Omega\text{cm}^2$ at 550°C and 1% oxygen. Depending on surface coverage, this ASR value was well larger.

Yashiro *et al.* [166], prior to those epitaxial thin film approaches, made use of thick cathodes where LSC_{214} was screen printed onto LSC_{113} phase. Due to high thicknesses resistances were well high with regard to requirement. No area specific resistance was analyzed but they did find 1-fold enhancement in resistance they obtained. The reason for this significantly reduced enhancement degree with respect to similar studies [11,15,21,68] is probably the horizontal alignment of constituent phases.

The another recent approach to utilize and maximize hetero interface has been adopted by Hayd *et al.* [122], giving $7 \text{ m}\Omega\text{cm}^2$ ASR at 600°C and $1.9 \Omega\text{cm}^2$ at 400°C . They constructed hetero interfaces by use of metal organic deposition (MOD) method which simply corresponds to crystallization of each phase from one solution having slight A and/or B-site deficient/excess cation stoichiometry. In other words, this was an *in situ* dual phase synthesis of $\text{LSC}_{113}/\text{LSC}_{214}$ system. In their MOD derived thin film cathodes both LSC_{113} and LSC_{214} as well as trace amount of Co_3O_4 precipitates were formed. But they reported 47 times higher k^q for dual phase cathodes than single phase perovskite as opposed to previous studies. The reason for reduced enhancement may

be deficiency of A and/or B-site cation stoichiometry of the solution, which may have led to reduced formation of secondary LSC₂₁₄ phases. Tuning these deficiencies may bring about further enhancement in ASR. Along with the promising ASR, MOD based derivation of thin film cathodes constitutes the lack of well-controllability of cathode production process especially in terms of microstructure. Definitely much of those studies probing hetero interface did exclude the chemical stability since their great concern was either revealing underlying reasons or achieving the lowest possible ASR.

As can be inferred from the literature information without giving reference to specific details, there are still debates in underlying reasons for anomalous activity of LSC₁₁₃/LSC₂₁₄ interface [11,15,68,75,85,88,151,168,169]. Assertions are generally done for lower and higher temperature regimes. Mapping this activity with underlying reasons as a function of temperature has a potential to end the debatable issues surrounding the phenomenon. However, such an attempt is not aimed in this thesis. Rather, the aim is the maximization of hetero interfaces with different compositions in order to yield the lowest possible cathode resistance with the help of different approaches.

In this study, accordingly, ASR values obtained by Crumlin *et al.* [21], Ma *et al.* [11] and Hayd *et al.* [122], all of which are corresponding to the highest degree of LSC_{113/214} dissimilar interface maximization in literature, will be success criteria together with accompanying process parameters such as cost, stability etc. In order to determine ASR for not only complete cathode but also ASR for surface oxygen exchange step, electrochemical impedance analysis is a powerful technique.

2.5. Motivation of The Work

The main starting point of this study is to maximize usable LSC_{113/214} hetero interfaces. Two methods have been adopted for this purpose. Firstly, rendering interfaces economically more feasible way has been adopted. Dual phase synthesis of LSC_{113/214} system from one solution via conventional Pechini method has been utilized with varying solution cation stoichiometry. So long as nano-crystals of each phase nucleates separately through synthesis process, their sizes are below the critical

utilization length [6,171] and their penetration to each other is highly successful, dual phase synthesis is expected to result in continuous hetero interface formation and successful ASR reduction. This is because continuous hetero interfaces are expected to spread over all the microstructure in as-synthesized powders. Such a result would correspond to quite economic way to derive quite densified hetero interfaces regarding conventional and relatively cheap SOFC cathode preparation methods.

In the second approach, due to the apparent advantages of deriving vertical hetero interfaces, these hetero-interfaces will be tried to be derived with possibly higher spatial density. In this approach, magnetron co-sputtering has been used. This is expected to make contribution to oxygen reduction activity in the hetero-structured cathode as well as varying degree of hetero-interfaces through film as a result of sputtering from differently positioned targets.

As the first time, dual phase synthesis of $\text{LSC}_{113/214}$ system via low temperature solution based method has been used. Simultaneous sputtering of phases with magnetron sputtering is also the first in literature.

CHAPTER 3

IN SITU ELECTROCHEMICAL IMPEDANCE ANALYSIS

3.1. *In situ* Electrochemical Impedance Spectroscopy

The concept of resistance is a well-known and understood phenomenon, which simply expresses the ability of material to resist electron flow formulated via Ohm's Law, $R = V/I$, where R is resistance, V is voltage and I is current. For direct current flow, each term in this equation reaches an ultimate equilibrium value and this ultimate value of resistance is denoted as R. However, under alternating current, concept of impedance releases where both V and I values becomes functions of time yielding equation $Z = V(t)/I(t)$ [36]. Application of a certain voltage amplitude, E_0 , with a certain frequency, ω , brings about current with varying amplitude, which is shifted in phase, with respect to applied potential, denoted as φ . Therefore, impedance is characterized by the fact that potential and current are not in phase; they are non-synchronized.

$$Z = \frac{E_0 \sin(\omega t)}{I_0 \sin(\omega t + \varphi)} = Z_0 \frac{\sin(\omega t)}{\sin(\omega t + \varphi)} = Z_0 (\cos(\varphi) + j \sin(\varphi))$$

Here j is $\sqrt{-1}$, resulting in typical Nyquist plot displaying both real ($Z_{real} = Z' = |Z|\cos(\varphi)$) and imaginary ($-Z_{imaginary} = Z'' = |Z|\sin(\varphi)$) as illustrated in Figure 3-1 given below.

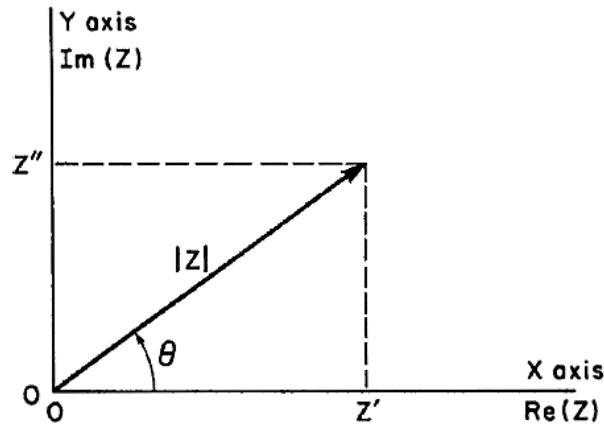


Figure 3-1 $|Z|$ corresponds to certain value of impedance at unique perturbation frequency [172]

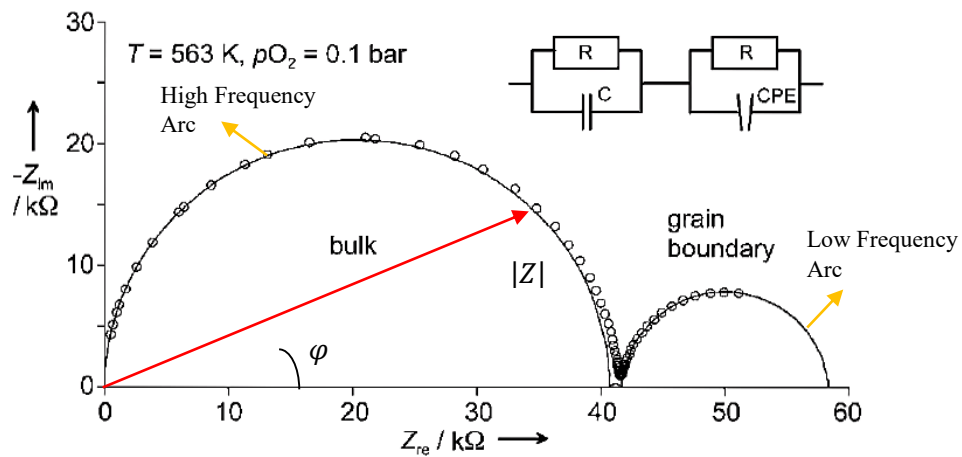


Figure 3-2 Nyquist Plot of Fe doped SrTiO₃ and corresponding equivalent circuit [173]

How fast the system responds to the applied voltage is determined by its kinetic, which inevitably forms a phase shift between voltage and current, making EIS a powerful technique for reaction kinetic investigations.

In Figure 3-2, there releases two separated and serially connected resistances, both of which are connected in parallel with an ideal capacitor of constant phase element (CPE). CPE differs from ideal capacitor behavior with its shape constituting extended

semicircle in diameter while in ideal capacitor, shape is an exact semicircle. Usually low frequencies yield constant phase element due to very long response recording time intervals of low frequencies. So, CPE is an experimental defect especially in case of solid state impedance characterizations with low frequencies [134,174,175]. There are also other circuit elements such as Gerischer and Warburg [172,176]. EIS is a broad area. So, this study is rather keen on experimental considerations.

3.2. Considerations Regarding Solid State Analysis

In cathode EIS analysis, system or material is perturbed by use certain voltage amplitude. Providing that the chemical processes triggered via current supplied (or equivalently electron flow), it must response to this flow. If the chemical process is slow, changing the direction of perturbation voltage amplitude with high frequencies, i.e. 1 MHz, results in making chemical species immobile since reaction is already slow. For this slow reaction to take place, more time should be supplied to system in order to record responses. Reverse is also true. Therefore, slow processes can be source of resistance if and only if they are perturbed with low frequencies. That's why the impedance arc associated with surface oxygen exchange process is named as 'low frequency arc' while charge transfer processes can yield impedances only when high frequency perturbation is used [133,134,177] since charge transfer is fast process. So, fast processes can be perturbed via high frequencies and slow processes can give resistance with low frequencies.

In dense thin film cathode examinations by EIS, bulk transport does not constitute a source resistance since the length over which ion migration must take place is extremely small. The remaining two processes are ion exchange at electrode/electrolyte interface and surface oxygen exchange. Between these two, surface exchange is much slower than ion exchange at electrode/electrolyte interface. So, surface exchange process can only give resistance at low perturbation frequencies; at very high frequencies oxygen gas near the surface stays immobile. That's why in EIS examinations, low frequency arc is associated with surface oxygen exchange process. This is possible only when the film thickness is below the critical utilization length denoted as $l_\delta = D^q/k^q$ [6,173]. For the film thicknesses smaller than l_δ , this

low frequency arc becomes *independently* visible. Real component of this arc is directly attributed to surface oxygen exchange process. A representative illustration in which high and low frequency arcs are well separated is seen in Figure 3-2.

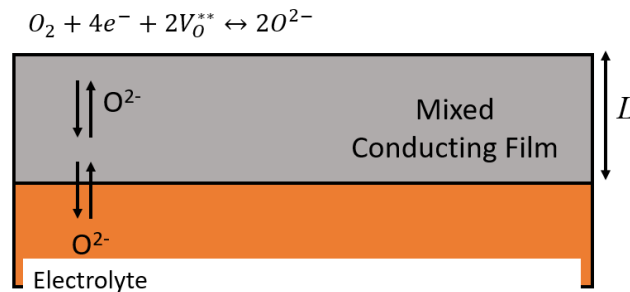


Figure 3-3 Dense thin film cathode where L represents critical utilization length
(adapted from [178])

Since oxygen exchange kinetic is a function of surface area, resistance obtained from low frequency arc (oxygen exchange) is multiplied with cathode surface area. So long as lattice oxygen content is known, surface oxygen exchange constant (k^q) can be directly calculated [133,173] follows;

$$k^q = \frac{k_B T}{4e^2 R_s C_O}$$

k_B is Boltzmann constant, T absolute temperature, e is elementary charge, C_O is lattice oxygen content [111] in given temperature characterized by oxygen non-stoichiometry and finally R_s ($Area * R$) is area specific resistance.

At first glance, this equation gives impression of linear correlation between R_s and temperature. However, C_O is also a function of temperature changes due to formation of oxygen vacancies with varying T . One must at this point be informed that surface oxygen exchange step is activation limited and expected to obey Arrhenius behavior [179]. Combining these information foresees linear relationship between ASR and $\ln(1/T)$. This is in turn a crosscheck of that whether measured resistance is originated from surface exchange or diffusion of species.

When cathode is not thin dense film, then system is said to be not well defined [133] so as to separate the responses originated from different chemical processes and/or microstructural features constituting source of resistance such as grain boundary, surface exchange, various interfaces and ion exchange. While some of these are charge transfer processes (ion-exchange at electrode/electrolyte interface), the others namely surface exchange and solid state diffusion are called non-charge transfer steps [180].

In dense thin film, one charge transfer (ion exchange) and one non-charge transfer step (surface exchange) constitute the overall cathode resistance. But thick cathodes for example involve additional grain boundaries as a new source of resistance [181]. While there are many proposed circuit models as a way for interpretation of eventual response, the most popular and accepted one is ALS (Adler-Lane-Steele) model [182,183].

This model asserts that overall oxygen reduction in cathode is mainly and simultaneously limited by surface oxygen exchange and solid state diffusion so long as mixed conducting oxide has high both ionic and electronic conductivity and without any gas phase diffusion limitation [15]. Mathematical implication of this model is as follow;

$$R_{chem} = \left(\frac{RT}{2F^2} \right) \sqrt{\frac{\tau}{(1 - \varepsilon)D_v c_v a r_0 (\alpha_f + \alpha_b)}}$$

Here R is gas constant, T is temperature, F is Faraday's constant, ε , a and τ are porosity, surface area and solid state tortuosity respectively, D_v is vacancy diffusivity, c_v is vacancy concentration, r_0 is the exchange flux density from which surface oxygen exchange constant (k) is extracted α_f and α_b constants for forward and backward reactions. R_{chem} is the resistance caused by cathode having thickness $L < 3l_\delta$ [182]. If $L > 3l_\delta$, this model predicts additional serially connected arcs arisen from charge transfer processes, denoted as "interfaces" in Figure 3-4 given below.

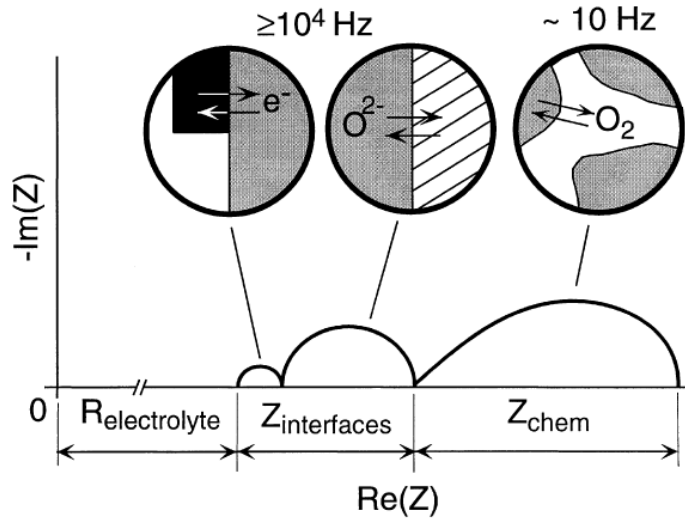


Figure 3-4 Resultant proposed impedance response from cathode having $L > 3l_\delta$ according to S. B. Adler [180,182]

If, on the other hand, $L < 3l_\delta$, these charge transfer contributions disappear and only Z_{chem} (in the form of Gerischer response [6,176]) signal is obtained [180]. Adler [182] states that this critical $L = 3l_\delta$ value below which only Z_{chem} response is visible can be up to $20 \mu\text{m}$ for MIEC perovskites depending upon T and P_{O_2} . In addition, as L significantly deviates from $3l_\delta$ to lower values, Z_{chem} response looks more like an ideal semi-circle similar to $Z_{interface}$ [182].

Both diffusivity and surface oxygen exchange coefficients can be derived from ALS model as can be inferred from equation. However, even for this indirect method, parameters like, surface microstructural area, tortuosity, porosity should be highly clarified in order for exactness of calculated D and k . This is possible with 3D tomography by expensive and indirect SEM-FIB method [48]. Moreover, for ALS model to be suitable and exact, homogeneity through microstructure is sought, which is some sort of idealization in another aspect. Such well-defined microstructure might not be derived always. Moreover, each cathode will have its own microstructural parameters such as porosity, tortuosity and surface area.

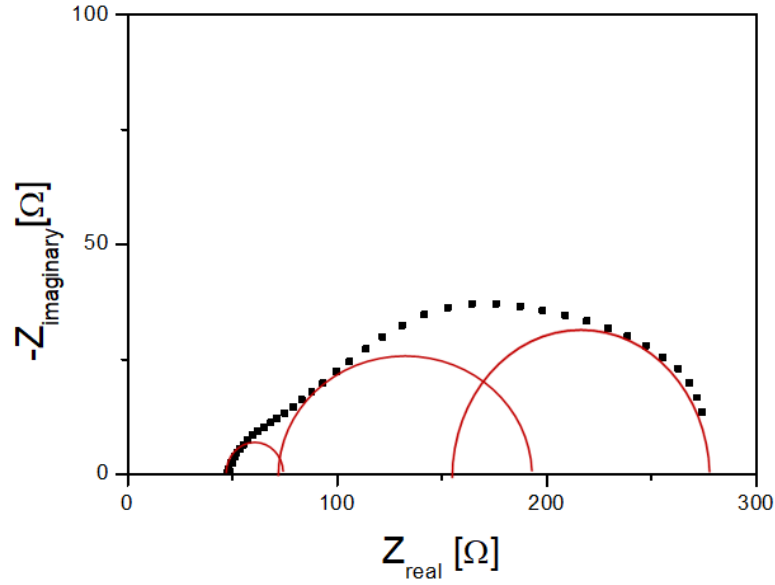


Figure 3-5 Impedance spectra for 70 μm thick LSC_{214} cathode at 650 $^{\circ}\text{C}$ and 0.1 atm P_{O_2} . Red ones are any probable arcs and black dots are original data. Arcs are convoluted.

As a result of all these abovementioned practical reasons, namely microstructural heterogeneity, in case of cathodes having thickness $L > 3l_{\delta}$, all responses are somehow convoluted as will be manifested in this study, as well. That is to say that arcs are penetrated to each other, making identification of them more and more difficult. An example to this is given in Figure 3-5, in which different impedance responses (arcs) are convoluted with each other.

At this point, it is worthwhile to note that every EIS response recorded, even the most complicated ones, can be expressed by use of an equivalent circuit model fitting well to this recorded response. Thanks to this matched model, deconvolution of arcs is possible.

However, this corresponds to some sort of mathematical fitting rather than a reasonable *physical* meaning such that any other circuit model can also be matched with recorded data. Reverse may also be true; the circuit model can be reasonable more or less. The key problem is that how representative is this matched circuit model is not exactly known in highly complicated and heterogeneous microstructures. The

general case is that as cathode thickness is reduced, equivalent circuit model is more probable to give physically reasonable deconvolution.

That is why in SOFC cathode research well defined systems are used in electrochemical characterizations. The best one among them is dense thin film cathodes in this respect. In conditions where cathode is porous due to better performance caused by for example excess air inlet, microstructure is tried to be controlled well and cathode thickness is tried to be reduced for further representative evaluation.

Apart from these, EIS is very powerful way to differentiate electrolyte response from cathode response in a SOFC stack no matter how the cathode is [184]. This is because electrolyte is purely ionic conductor inside which oxygen atom has already been completely reduced and so it cannot be further perturbed via electron flow.

CHAPTER 4

SYNTHESIS AND PERFORMANCE OF THICK LSC CATHODES

4.1. Synthesis of Powders

Examination of LSC cathodes performance begins with their synthesis. For this purpose, Pechini method, which is simply low temperature solution based method, was employed [23]. A typical flowsheet of Pechini synthesis is illustrated in Figure 4-1. As precursors, nitrates of cations are used. These are namely $\text{Co}(\text{NO}_3)_2 \cdot 6\text{H}_2\text{O}$ (Alfa Aesar 98-102%, product no: 36418), $\text{La}(\text{NO}_3)_3 \cdot 6\text{H}_2\text{O}$ (Alfa Aesar, 99.99%, product no:11267), $\text{Sr}(\text{NO}_3)_2$ (Alfa Aesar, 99.0%, product no:12232) for the syntheses of LSC_{113} and LSC_{214} powders, $\text{Ce}(\text{NO}_3)_3 \cdot 6\text{H}_2\text{O}$ (Alfa Aesar, 99.5%, product no:11329) and $\text{Gd}(\text{NO}_3)_3 \cdot 6\text{H}_2\text{O}$ (Alfa Aesar, 99.9%, product no:12917) for GDC electrolyte. These nitrates were mixed in beaker with a certain stoichiometry so that the final desired cation fractions are satisfied.

Success in attaining single phase powders by Pechini method is, in principle, dependent upon amount of chelating agent which was citric acid ($\text{C}_6\text{H}_8\text{O}_7 \cdot \text{H}_2\text{O}$, Merck 99.0%, product no:100244) in the synthesis process. Chelating agent is responsible for the formation and homogeneous distribution of metal-organic complexes [23] during which cations are covered by chelation agent and re-oxidation of individual cations are prevented. For this process to successfully take place, mole of citric acid must be at least twice as much as the total moles of cations in solution. For further

assurance, mole of citric acid was adjusted to be 3 times as much as the total cations mole in this synthesis. DI water was excess in solution.

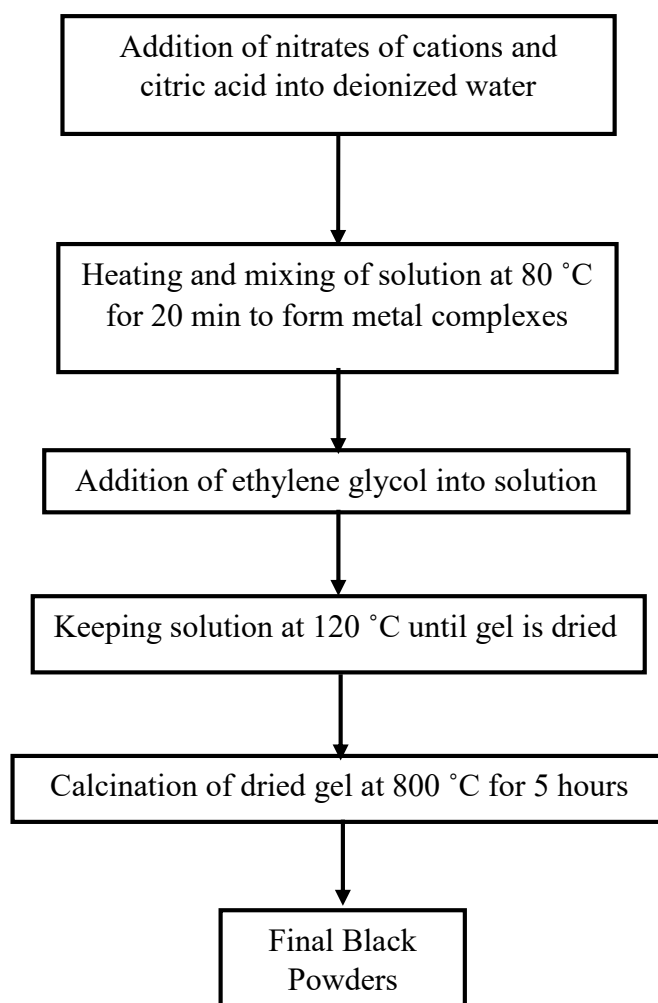


Figure 4-1 Typical flowsheet of Pechini synthesis process

After addition of citric acid to aqueous solution, magnetic stirrer was put in beaker and solution was stirred up at 80 °C for at least 20 min. This was followed by addition of ethylene glycol (Merck, C₂H₆O₂ 99.0%, product no:109621) for poly-esterification reaction. The mole of ethylene glycol was 2 times as much as the mole of citric acid. After addition of ethylene glycol, solution temperature was raised to 120 °C. Until dried gel was obtained, solution was kept at this temperature. This was followed by calcination of dried gel at 800 °C for 5 hours. Then, eventual powders were obtained.

Aforementioned procedure (Figure 4-1) is given in terms of approach that could be altered depending on powder to be synthesized. For three different powders (phases) synthesized different details could be observed.

4.1.1. Synthesis of Single Phase LSC₁₁₃ and LSC₂₁₄

Since high oxygen reduction rate reported to be up to date has been found between (La_{0.8}Sr_{0.2})CoO_{3-δ} and (La_{0.5}Sr_{0.5})₂CoO_{4±δ} [21,166], n_{Co}:n_{La}:n_{Sr} ratio was adjusted as 1:0.8:0.2 for perovskite LSC₁₁₃ and 1:1:1 for Ruddlesden-Popper LSC₂₁₄, respectively. Relative amounts of nitrate precursors were added into solution accordingly. Relative amounts of citric acid and ethylene glycol were kept constant as it was stated previously; n_{cations}:n_{citric-acid}:n_{ethylene-glycol} was 1:3:6. This is exemplified in Table 4-1.

Table 4-1 Precursors stoichiometry calculation for La_{0.8}Sr_{0.2}CoO₃ powder

La _{0.8} Sr _{0.2} CoO ₃ -(M _A =235.546 gr)	M _A (gr)	Amount (gr)	Mole
Co(NO ₃) ₂ .6H ₂ O	291.04	4.000	0.013744
La(NO ₃) ₃ .6H ₂ O	433.01	4.761	0.010995
Sr(NO ₃) ₂	211.63	0.582	0.002749
Citric Acid Monohydrate	210.14	17.329	0.082464
Ethylene Glycol	62.07	20.474	0.329856

However, there were differences in the final calcination temperature and time for each phase. Different from that illustrated in Figure 4-1, calcination temperature was found to be at least 740 °C for (La_{0.8}Sr_{0.2})CoO_{3-δ} phase. Full crystallization of (La_{0.8}Sr_{0.2})CoO_{3-δ} powder could be attained in calcination temperature-time combination of 750 °C and 5 hours.

On the other hand, subsequent calcinations at incrementally increased temperatures starting from 700 °C demonstrated that the minimum calcination temperature for LaSrCoO_{4±δ} was found to be at least 800 °C. Calcination at 775 °C even more than 30 hours did not yield fully crystalline structure. But 5-hour calcination at 800 °C was sufficient for obtaining fully crystalline LaSrCoO_{4±δ} powder. These observations

imply an earlier formation of $(\text{La}_{0.8}\text{Sr}_{0.2})\text{CoO}_{3-\delta}$ over $\text{LaSrCoO}_{4\pm\delta}$. But this statement requires verification via in situ monitoring of nucleation growth process in the synthesized powders.

Aforementioned single phase powders were synthesized in pursuit of physically blending them and maximizing $\text{LSC}_{113/214}$ hetero interface in that way. But prior to cell fabrication and performance characterization by EIS, powders were characterized structurally by use of XRD analysis.

In order to ensure the absence of any undesired second phase in as-synthesized powders, X-ray diffraction analyses were completed. For *all* of the as-synthesized powders, diffraction patterns were collected with 0.016 °/min scan rates between $2\theta=5^\circ$ and $2\theta=120^\circ$. Such small scan rate was selected in order to perform Rietveld refinement of XRD pattern.

Copper gun with Ni filter was used for X-ray generation (Rigaku) offering $\text{CuK}\alpha$ radiation and creating wavelength of $\lambda=1.54056 \text{ \AA}$. X-ray generator voltage and current were adjusted and kept constant as 40 kV and 40 mA, respectively. XRD results with accompanying Rietveld refinement quantitatively revealed the crystal structures, site occupancies as well as lattice parameters and phase fractions. GSAS-II/EXPGUI software was used for Rietveld analysis.

Instrumental flaws manifested through XRD patterns have been first revealed to exclude the effects of them on patterns. For this purpose, XRD pattern of a standard sample, about which whole crystallographic information was initially known, has been obtained. This standard sample was Silicon named as Nist640d. It is known to have face centered cubic structure with “F d $\bar{3}$ m” space group and 5.43123 Å lattice parameters. Keeping these constant, instrumental parameters, namely Cagliotti terms, have been extracted as given in Table 4-2, manifesting also the degree of fitting by virtue of χ^2 , R_p and R_{wp} values, which are indicating strong fit between calculated and observed patterns. Figure 4-2 illustrates how good the match is for standard sample refinement, making analysis confident on the values of Cagliotti terms.

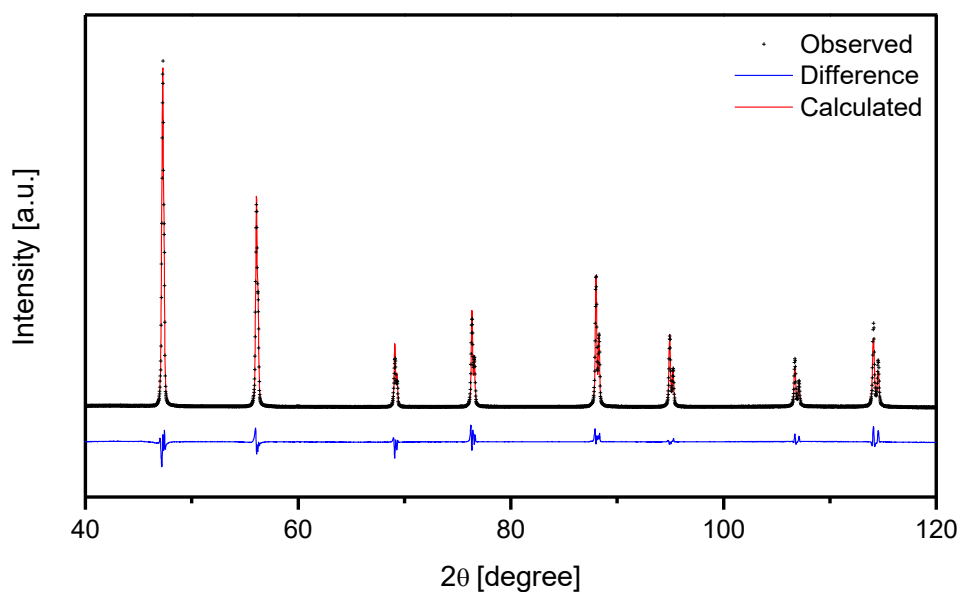


Figure 4-2 Refined profile of standard Silicon powder sample Nist640d

Table 4-2 Rietveld refinement results for standard Silicon powder sample

Silicon-Nist640d Rietveld Refinement-Space Group: (F d $\bar{3}$ m)						
Fitting Parameters			Cagliotti Terms			
χ^2	R_p	R_{wp}	GU	GV	GW	
3.875	0.0774	0.104	11.1284	-1.41135	8.22116	

Refinements were initially conducted on $(La_{0.8}Sr_{0.2})CoO_{3-\delta}$ and $(La_{0.5}Sr_{0.5})_2CoO_{4+\delta}$ single phase powders in the light of Cagliotti terms. Results apparently indicate that there is no any undesired phase and single phase powders have successfully been synthesized. Refined patterns are given in Figure 4-3 and Figure 4-4. Studies conducted by Sikolenko *et al.* [185] and Sanchez-Andujar *et al.* [186] have been referred in terms of crystallographic information data.

Refinement parameters for all single phase powders are given in Table 4-3 given below. All refinements manifested preferred orientation in powders. In case of $(La_{0.8}Sr_{0.2})CoO_{3-\delta}$ powders (300), (214) are the planes through which strong preferred orientation took place. Similarly, significant preferential orientation was

observed through (114), (303) and (215) reflection planes in $(\text{La}_{0.5}\text{Sr}_{0.5})_2\text{CoO}_{4+\delta}$ phase.

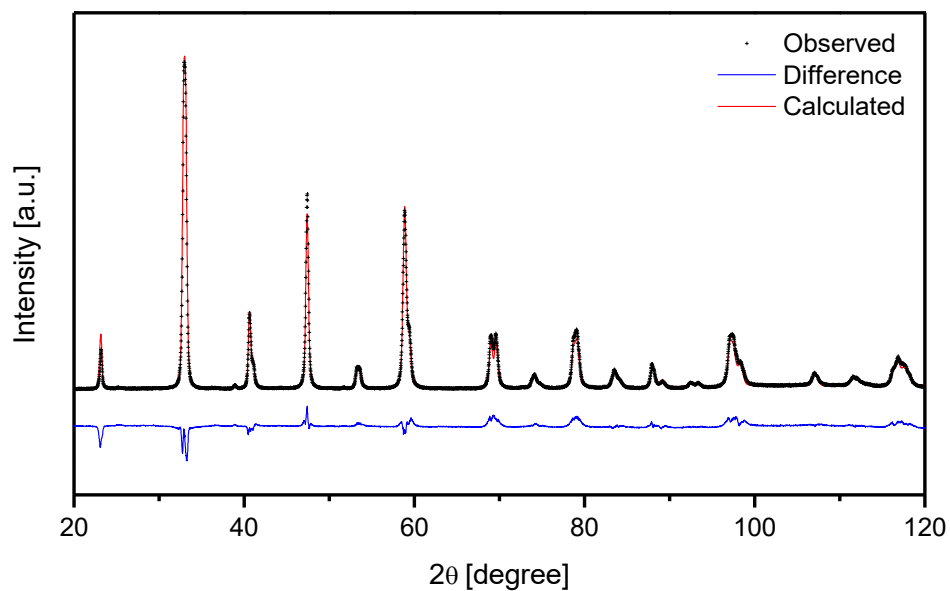


Figure 4-3 Refined XRD pattern of $(\text{La}_{0.8}\text{Sr}_{0.2})\text{CoO}_{3-\delta}$

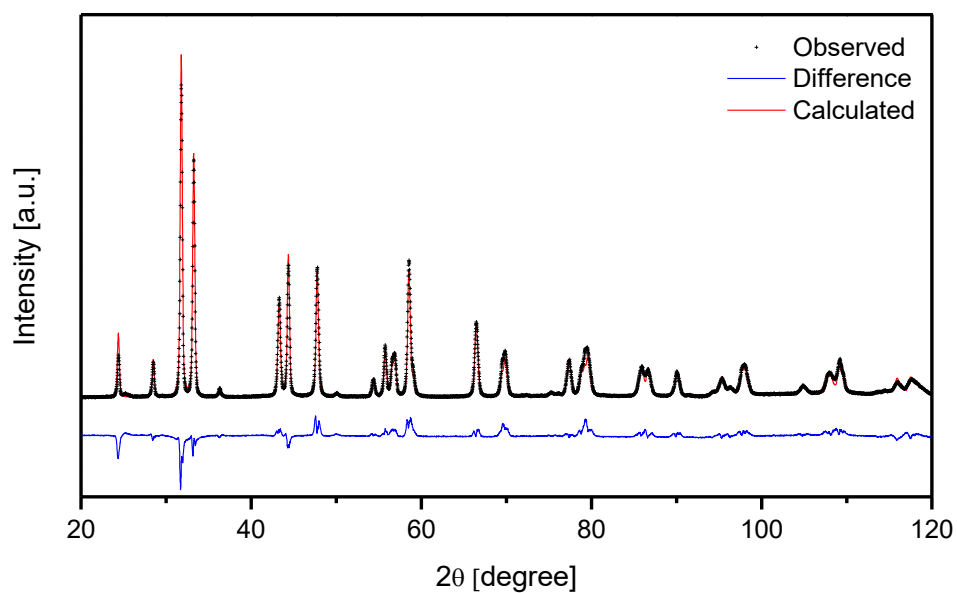


Figure 4-4 Refined XRD pattern of $\text{LaSrCoO}_{4+\delta}$

Table 4-3 XRD analysis results of single phase (La_{0.8}Sr_{0.2})CoO_{3-δ} and LaSrCoO_{4+δ} powders

	(La _{0.8} Sr _{0.2})CoO ₃	LaSrCoO ₄
Lattice Parameters (in Å)	a 5.442	a 3.805
	c 13.183	c 12.506
Fitting Parameters	χ^2 3.745	χ^2 5.112
	R _p 0.117	R _p 0.128
	R _{wp} 0.149	R _{wp} 0.162
	L _X 13.219	L _X 11.426
Scherer Crystallite Size (in nm)	60.126	69.562
Space Group	(R $\bar{3}$ c)	(I 4/m m m)

The lattice parameters in Table 4-3 are consistent with the literature values for current Sr compositions of phases [185–187]. Fitting parameters as well as degree of fit as illustrated in Figure 4-3 and Figure 4-4 make refinements confident. Based on this confidence, Lorentzian isotropic crystallite size broadening term, L_X, is extracted and by inserting it into Scherer Equation given below, average crystallite sizes have been found. P is crystallite size, K is shape factor and equal to 0.9 and λ is wavelength of X-rays

$$p = \frac{18000 * K * \lambda}{\pi * L_X}$$

If it is considered that Scherer equation can estimate sizes lower than 45 nm accurately and sizes lower than 90 nm roughly [188], current L_X values are reasonable. However, SEM images of LSC₁₁₃ and LSC₂₁₄ in Figure 4-5 show higher particle sizes than calculated ones. In this case, what is said to be crystallite is not equivalent to particle, which means that particles are not defect or strain-free. But, powders were result of solution based synthesis, which is supposed to make them non-susceptible to strain formation. In this way, this is a noticeable result.

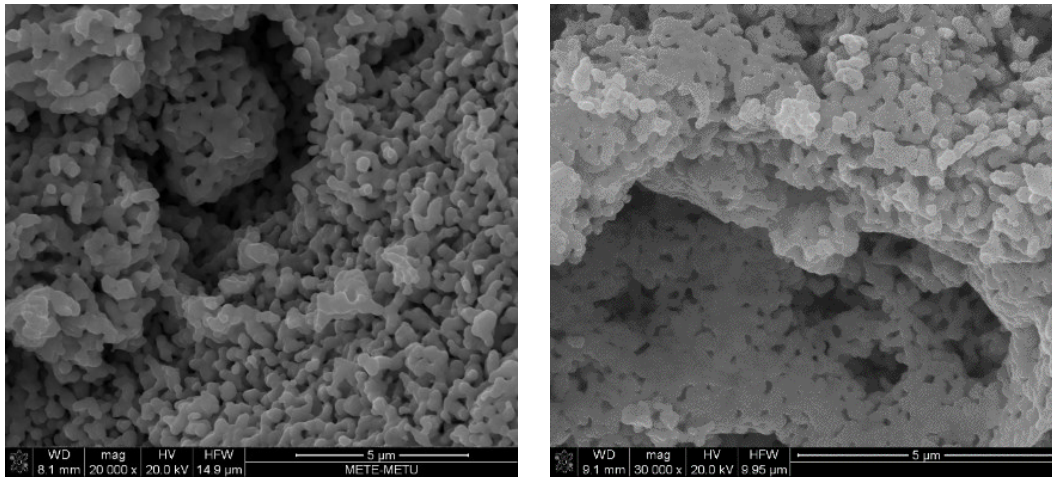


Figure 4-5 SEM images of $(\text{La}_{0.8}\text{Sr}_{0.2})\text{CoO}_{3-\delta}$ and $\text{LaSrCoO}_{4+\delta}$ with 20k and 30k magnifications, respectively

To sum up, XRD patterns accompanied by Rietveld refinement results clearly shows that single phase synthesis of $(\text{La}_{0.8}\text{Sr}_{0.2})\text{CoO}_{3-\delta}$ and $(\text{La}_{0.5}\text{Sr}_{0.5})_2\text{CoO}_{4+\delta}$ were very successful. Lattice parameters are in good agreement with literature. It is also seen that “structural” size determined based on Rietveld refinement refers to crystallite size and not to particle size. However, SEM images are obvious indicators of particle sizes.

4.1.2. In situ EIS Analysis of Porous Cathodes of Physical Mixture

Independently synthesized single phase powders of $(\text{La}_{0.8}\text{Sr}_{0.2})\text{CoO}_{3-\delta}$ and $\text{LaSrCoO}_{4+\delta}$ were mixed with 1:1 molar ratio in order to obtain physically blended $\text{LSC}_{113/214}$ two phase structure. By means of physical blending, hetero interface extension was aimed. Final mixed powders were examined by electrochemical impedance spectroscopy (EIS) concerning the degree of hetero interface formation-extension success.

4.1.2.1. Symmetric Cell Preparation via Powders

Prerequisite for analyzing performance of powders is, certainly, preparation of cell, which is comprehensively explained in following pages from slurry preparation to EIS experimental parameters.

4.1.2.2. Electrolyte Synthesis and Fabrication

The underlying reason for seeking the lowest possible temperature-time combination for calcination of LSC powders was to prevent grain growth while allowing porosity in the structure. This is because porosity is sought in cathodes. However, $(\text{Ce}_{0.9}\text{Gd}_{0.1})\text{O}_{2-\delta}$ powder was synthesized for electrolyte fabrication performed via sintering and there was no particle size concern. Therefore, flowsheet in Figure 4-1 was followed for GDC powders and calcination was carried out at 800 °C, although it was experienced that lower temperatures were also sufficient for GDC calcination.

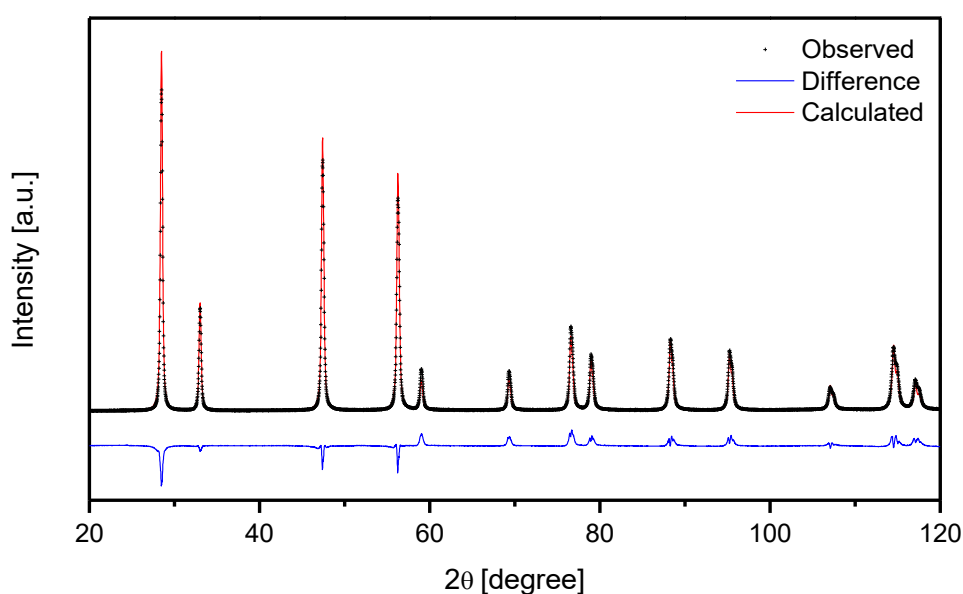


Figure 4-6 Refined XRD pattern of $(\text{Ce}_{0.9}\text{Gd}_{0.1})\text{O}_{1.95}$

Table 4-4 XRD analysis results of $(\text{Ce}_{0.9}\text{Gd}_{0.1})\text{O}_{2-\delta}$ powders

	$(\text{Ce}_{0.9}\text{Gd}_{0.1})\text{O}_{2-\delta}$
Space Group	$(F m \bar{3} m)$
Lattice Parameters	5.418 Å
Fitting Parameters	χ^2 3.405
	R_p 0.109
	R_{wp} 0.133
	L_x 18.155
Scherer Crystallite Size	43.779 nm

Following the prescribed flowsheet, single phase GDC powders were synthesized successfully as manifested by Rietveld refinement on XRD patterns in Figure 4-6. Brauer *et al.* [187] is referred in terms of crystallographic information data in pursuit of Rietveld refinements of GDC powders XRD pattern. Comprehensive resultant structural information is given in Table 4-4. Refined pattern of $(\text{Ce}_{0.9}\text{Gd}_{0.1})\text{O}_{2-\delta}$ powder indicated preferential orientation through (220) and (311) planes. Fitting parameters values are assuring the refinement. In case of GDC, there is more deviation between Scherer crystallite size and particle size as revealed by scanning electron microscope image of it (see Figure 4-7).

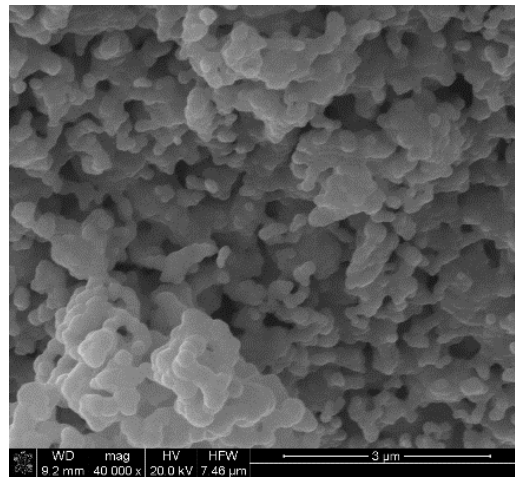


Figure 4-7 SEM image of $(\text{Ce}_{0.9}\text{Gd}_{0.1})\text{O}_{2-\delta}$ with 40k magnification

After assuring the structural characteristics of GDC powders, they were used to fabricate electrolytes of prospective symmetric cells. For this purpose, as-synthesized GDC powders were pressed into 18-mm diameter and 1 mm-thick pellets that was followed by sintering of pellets at 1350 °C for 8 hours at ambient air. Final dense GDC pellets, on which cathode slurries were applied, were used as electrolyte of the final symmetric cells.

4.1.2.3. Slurry Preparation

After testing powders structurally, slurries were prepared with the powders. These slurries were then used to fabricate porous thick cathodes of symmetric cells. Addition of each chemical was followed by 15-min ball milling (160 revolutions per minute) with 5 mm diameter ZrO₂ balls. Sequence of addition of chemicals is the same as the sequence of Table 4-5 given below. After addition of chemicals and ball milling for a good blending, slurries were ready to be a part of symmetric cells. Slurries, and so symmetric cells, were prepared both from single phase (La_{0.8}Sr_{0.2})CoO_{3-δ} and (La_{0.5}Sr_{0.5})₂CoO_{4+δ} powders and the physical mixture of them. This physical mixture is denoted as PM in EIS analyses.

Table 4-5 Chemicals used to prepare cathode slurry

Chemicals	Function	Gram per 0.5 gr powder
Fish Oil	Dispersant	0.0117
Toluene	Solvent	0.2350
PEG	Plasticizer	0.0365
BBP	Releasing agent	0.0475
PVB	Binder	0.0265

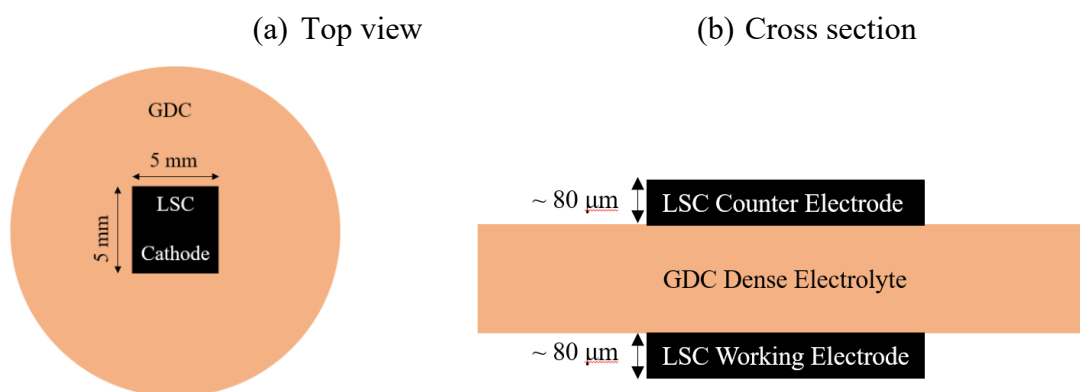


Figure 4-8 (a) Top view and (b) cross section of half cells accommodating thick porous cathodes

4.1.2.4. Cell Fabrication

After the final ball milling, slurries were applied onto GDC pellets over the plasters having apertures with $5 \times 5 \text{ mm}^2$ area. The thickness of plaster was $80 \text{ }\mu\text{m}$, which makes final cathode thickness expectations around $80 \text{ }\mu\text{m}$, too. Application of slurries were followed by firing cell at $400 \text{ }^\circ\text{C}$ for 5 hours in order to completely remove organics from cathode. This same process was applied onto each face of the pellet. One of the sides acted as counter electrode while the other acted as working electrode (see Figure 4-8).

Once the symmetric cells were made, gold wires (0.1 mm in diameter) were contacted via gold paste just onto cathode surfaces. This was followed by firing this contact point at $400 \text{ }^\circ\text{C}$ for 2 hours for good adhesion to cathode surface. Same procedure was applied for each face of cells. Then, these cells were placed on one edge of hollow shaped alumina pipes. The rest was indifferent from the procedure comprehensively explained in previous pages of this section.

4.1.2.5. EIS Measurements

Final symmetric cell (see illustration in Figure 4-8) fabricated via physically mixed powders was examined in terms of its cathode performance. The temperatures of EIS analysis was selected to be $400, 500, 550, 600, 650$ and $700 \text{ }^\circ\text{C}$. Lower temperatures highly reduce critical utilization length (namely up to 40 nm) and expecting to attain such reduced particle size is not realistic. However, at increasing temperatures critical utilization length can even reach several tens of microns [43,146]. So, alteration in temperatures is functional in terms of tuning critical utilization length. P_{O_2} were selected to be $0.01, 0.1$ and 0.21 atm .

Importance of P_{O_2} is originated from the fact that if overall ORR is limited by surface/interface processes purely, then impedance response must exhibit inversely P_{O_2} dependent behavior; higher partial pressure of oxygen facilitates ORR while in case of bulk diffusion limited behavior, lower P_{O_2} means promoted oxygen vacant sites within bulk, which significantly enhances oxygen diffusion and since ORR is limited by diffusion process, lower P_{O_2} lowers ASR in this case.

Perturbation amplitude was selected to be 10 mV with 5 points per decade and frequency range was 1MHz-10mHz. The reason for selection of 10 mV is not to perturb any other possible parallel reaction and attaining signals from one unique process during this multistep non-homogeneous oxygen reduction process. Higher perturbation amplitudes such as 50 mV could well perturb reactions more rapidly by providing more driving force but in this case additional chemical steps can also be agitated. In this case, final signals can't be confidently attributed to certain reaction step. Higher frequency ranges are always preferred but this brings about so much analysis time that even during measurement, properties of system changes. When it is considered that LSC cathodes are very sensitive to surface Sr segregation above 400 °C, it was best to keep analysis time possibly the minimum period. 1MHz-10mHz range is determined in this way.

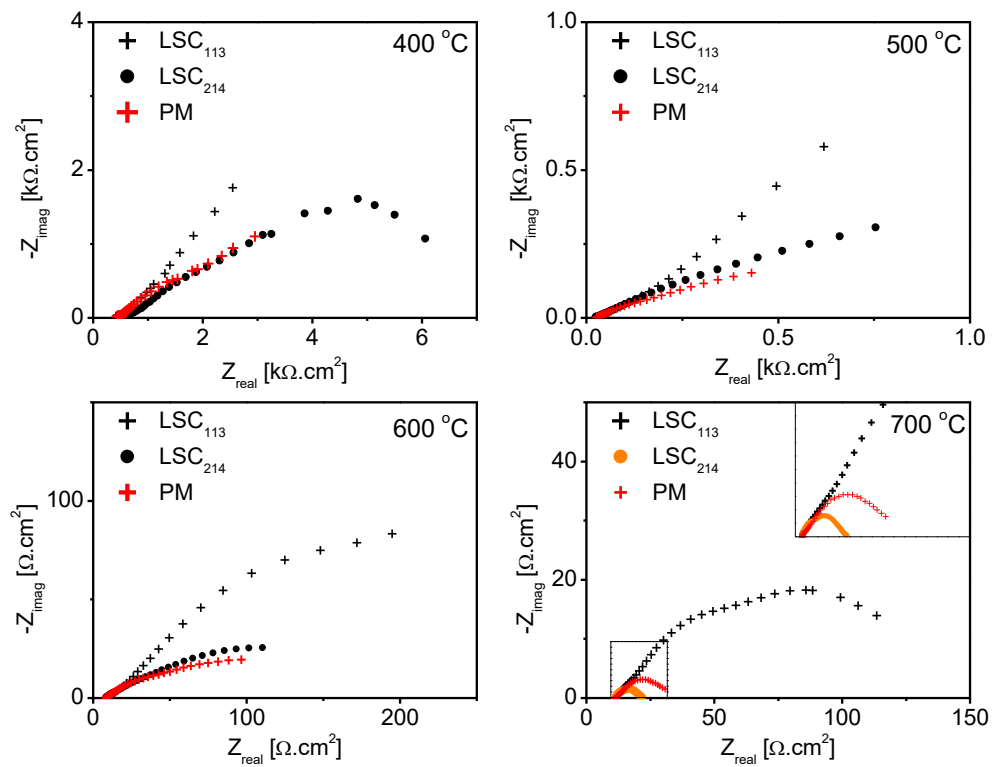


Figure 4-9 EIS responses of physically mixed powder (denoted as PM) at differential temperatures and ambient air

Since gold paste is highly porous, in calculation of ASR, cathode area was assumed to be 0.25 cm^2 , no significant ASR reduction was expected on surface thanks to highly porous gold paste [189]. In symmetric cells, $ASR = R_{cathode \text{ measured}} * Area/2$. Nyquist plots are drawn accordingly.

Unfortunately, Figure 4-9 (in which PM denotes physical mixture) shows that there is poor hetero-interface formation in physical blending of single phase $(La_{0.8}Sr_{0.2})CoO_{3-\delta}$ and $LaSrCoO_{4\pm\delta}$ powders, manifesting itself as a poor performance enhancement. While EIS at $400 \text{ }^\circ\text{C}$ mimics rule of mixture behavior, just slight enhancement which could be attributed to extension of hetero interface could only be attained at 500 and $600 \text{ }^\circ\text{C}$. Besides, co-existence of two phase becomes meaningless at $700 \text{ }^\circ\text{C}$. This electrochemical overview qualitatively manifests how poor the ability of physical mixing is to maximize hetero interface and promote cathode performance.

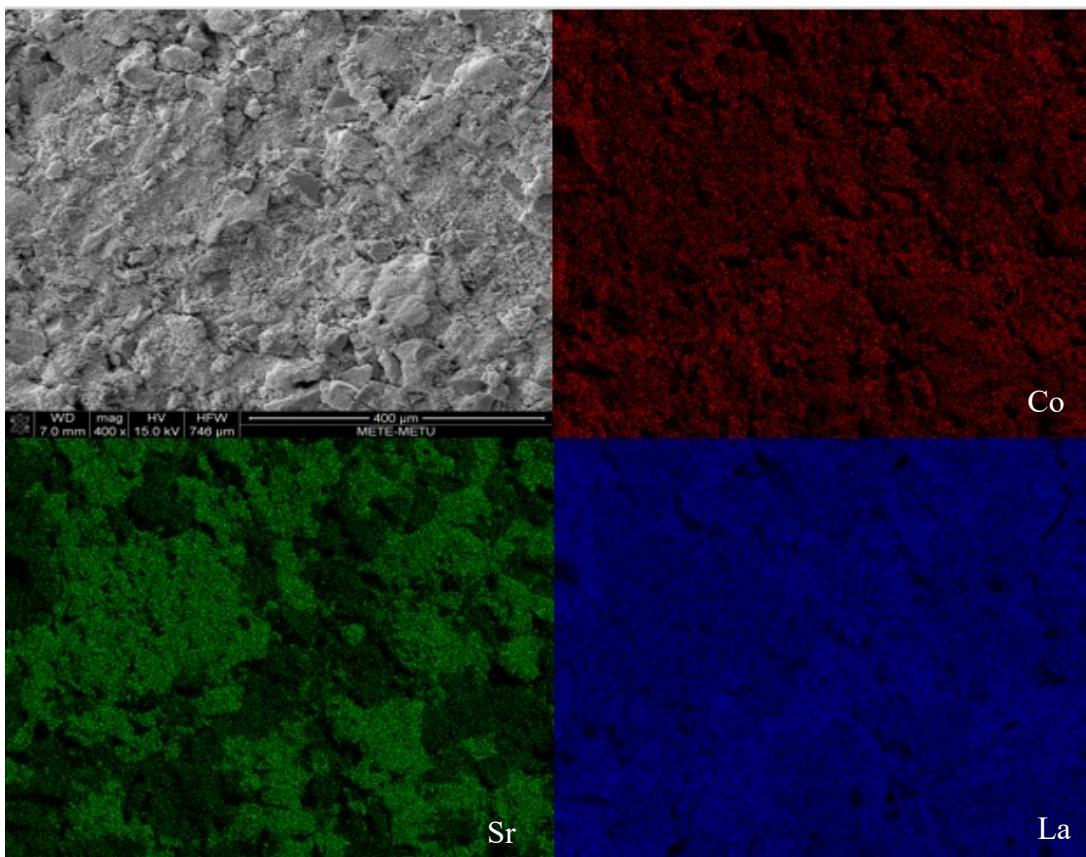


Figure 4-10 EDS mapping of physically mixed powder at 400 magnification

On the other hand, EDS mappings carried out on powder mixture can do this same *quantitatively*. Experimentally, 15kV accelerating voltage was used in order for having signals from rather near surface regions. For sufficient dead time in collecting signals, 5.5 spot size was selected. In order to reduce surface roughness, powders were pressed into pellets, were not exposed to high temperature, mounted in polyester and polished gradually.

In physically mixed powder, phases are namely $(\text{La}_{0.8}\text{Sr}_{0.2})\text{CoO}_{3-\delta}$ and $(\text{La}_{0.5}\text{Sr}_{0.5})_2\text{CoO}_4$ in which atomic fractions of La, Co and Sr are exactly known. Thus, expecting a significant contrast with mapping is reasonable at least for Sr atomic percent in case of physical mixing. Sr fractions are 0.04 and 0.14 in mixed powder for LSC_{113} and LSC_{214} respectively and such significant differential can easily be revealed by EDS mapping if matrix effects do not manipulate EDS. Figure 4-10 apparently proves this and manifests $\sim 100 \mu\text{m}^1$ scale of structure, as well.

In terms of Sr, huge contrast is manifested. The regions which are rich in Sr are slightly poor in terms of La as can be observed from Figure 4-10. Atomic fractions of La atoms are 0.16 and 0.14 in LSC_{113} and LSC_{214} respectively. EDS mapping is capable of revealing even such a slight differential, which is going to make EDS mapping quite reliable. Although it has higher atomic fraction difference (0.2 and 0.14), EDS mapping of Co atoms exhibited almost no contrast. This may be because of matrix effect when lower characteristic radiation energy ($\text{La}\alpha$ radiation for each atom) that Co atoms yield is taken into consideration.

To sum up, both EDS mapping and EIS responses of physically blended powders confirm that physical mixture of powders is not so effective in maximizing hetero interfaces.

4.2. One Pot Synthesis of Dual Phase of $(\text{La}_{1-x}\text{Sr}_x)\text{CoO}_3/(\text{La}_{1-y}\text{Sr}_y)_2\text{CoO}_4$

As opposed to physically blending two phases, synthesizing two phase structure *from one solution* which corresponds to one pot synthesis of dual phase could be a successful way of interface extension. For this purpose, everything was same as it was

¹ Roughly calculated by random line intercept technique.

comprehensively explained before (flowsheet in Figure 4-1), except for adjusting cation stoichiometry. Otherwise all the defined procedure was operated as explained previously.

In this case, nitrates of cations were separately adjusted for each phase such that as if $(\text{La}_{0.8}\text{Sr}_{0.2})\text{CoO}_{3-\delta}$ and $(\text{La}_{0.5}\text{Sr}_{0.5})_2\text{CoO}_{4+\delta}$ would form in final powders. Then these adjusted nitrates were added into a beaker with varying fractions assuming that formerly adjusted Sr doping levels for each phase would manifest themselves as $x=0.2$ and $y=0.5$ for LSC_{113} and LSC_{214} respectively in finally obtained powders (see Table 4-7). The highest possible interface extension is, in principle, expected in equal contribution of each phase. Therefore, three precursors of solutions were prepared in which relative amounts of phases were surrounding 1:1 ratio. Table 4-6 accordingly shows these precursors of solutions denoted as DP-1, DP-3 and DP-5. Moreover, as the way of checking the possible degree of penetration of nano-crystals to each other, physically mixed sample that previously evaluated was considered as a reference.

Table 4-6 Abbreviations of solutions and corresponding phase fraction expectations

	DP-1	DP-3	DP-5
$(\text{La}_{0.8}\text{Sr}_{0.2})\text{CoO}_{3-\delta}$	50%	60%	40%
$(\text{La}_{0.5}\text{Sr}_{0.5})_2\text{CoO}_{4+\delta}$	50%	40%	60%

Table 4-7 below manifests the stoichiometric nitrate calculation by virtue of DP-3. Same calculation is also valid for other dual-phase precursor solutions. Moreover, in order for comparison of final powders structurally, $(\text{La}_{1-x}\text{Sr}_x)\text{CoO}_{3-\delta}$ single phase powders with varying x (from 0-0.5) were synthesized to monitor lattice parameter variation in this study as a function of Sr doping. This is because lattice parameters referred in literature are mainly based on samples (powder or pellet), thermal history of which involved very high temperature processing. This consequently leads to lower lattice parameters in literature than what has been found in this study.

What is given in Table 4-7 represents the cation stoichiometry in the initial nitrate mixture within the beaker assuming $x=0.2$ and $y=0.5$. However, since the cation types

of both phases are exactly the same, whether any other undesired third phase would form or expected phase fractions would be achieved is not clear. Furthermore, there is no assurance for achieving presumed dopant degree of Sr in each phase as well as fictive phase fraction expectations. Contrary, deviation as a result of partitioning of Sr and La cations to each phase differently is very reasonable. Therefore, Rietveld refinement analysis is more fundamental tool in case of dual phase synthesis.

Table 4-7 Stoichiometric calculation for precursors of DP-3 powders as an instance

(La_{0.5}Sr_{0.5})₂CoO₄ (2n moles)	M_A (gr)	Amount (gr)	Mole
Co(NO ₃) ₂ .6H ₂ O	291.04	0.25000	0.00086
La(NO ₃) ₃ .6H ₂ O	433.01	0.37196	0.00086
Sr(NO ₃) ₂	211.63	0.18179	0.00086
Citric Acid Monohydrate	210.14	1.08306	0.00515
Ethylene Glycol	62.07	1.27964	0.02062
<hr/>			
La_{0.8}Sr_{0.2}CoO₃ (3n moles)	M_A (gr)	Amount (gr)	Mole
Co(NO ₃) ₂ .6H ₂ O	291.04	0.37501	0.00129
La(NO ₃) ₃ .6H ₂ O	433.01	0.44635	0.00103
Sr(NO ₃) ₂	211.63	0.05454	0.00026
Citric Acid Monohydrate	210.14	1.08306	0.00515
Ethylene Glycol	62.07	1.27964	0.02062
		TOTAL	
<hr/>			
DP-3 (5n moles)	M_A (gr)	Amount (gr)	Mole
Co(NO ₃) ₂ .6H ₂ O	291.04	0.62501	0.00215
La(NO ₃) ₃ .6H ₂ O	433.01	0.81830	0.00189
Sr(NO ₃) ₂	211.63	0.23633	0.00112
Citric Acid Monohydrate	210.14	2.16612	0.01031
Ethylene Glycol	62.07	2.55927	0.04123

4.2.1. Rietveld Refinement Evaluation of Dual Phase Powders

Sr site occupancies were not debatable for single phase powders since Sr fraction was already adjusted in initial solution prior to synthesis. However, this is not the case for

dual phase synthesis. In case of dual phase synthesis series, it is expectable for Sr compositions to well deviate from single phase powder by partitioning of it to phases differently. Furthermore, such uncontrolled Sr partitioning has a potential to give rise to formation of new and undesired phases and crystal structures. Thus, Rietveld refinement of XRD patterns belonging to dual phase syntheses is of significant importance.

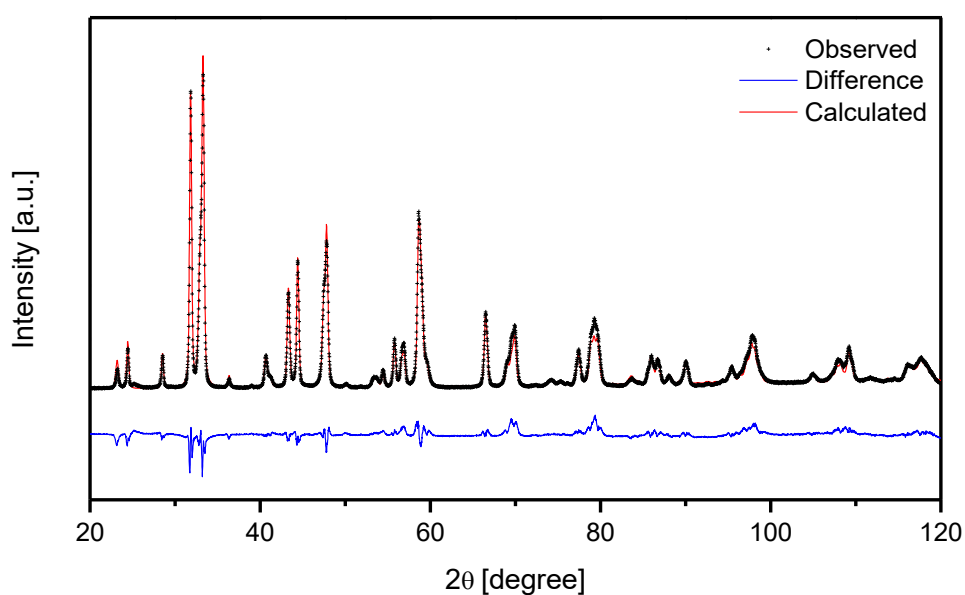


Figure 4-11 Refined pattern of DP-5

First, apart from partitioning problem, XRD patterns of dual phase series prove that synthesizing two phase system from one unique solution in the beaker is very successful; patterns clearly look like summation of all reflection peaks of single phase powders of LSC_{113} with the space group of $R\bar{3}c$ and LSC_{214} with the space group of $I4/mmm$, sure with accompanying slight peak position changes with respect to aforementioned single phase patterns. There is not any undesired third phase². Figure 4-11, Figure 4-12 and Figure 4-13 manifest this. Crystal structures are rhombohedral

² It should be kept in mind that XRD analysis with $\text{CuK}\alpha$ radiation is unable to differentiate existence of a possible additional phase less than certain limit. Therefore, the statement above should be treated with caution, since a third phase below the detectability limit might exist in the powders.

and tetragonal just like single phases, which means that x in $(\text{La}_{1-x}\text{Sr}_x)\text{CoO}_{3-\delta}$ must be in range of $0 < x < 0.5$ [190] and y in $(\text{La}_{1-y}\text{Sr}_y)_2\text{CoO}_{4\pm\delta}$ must be in the range of $0.3 < y < 1$ [72]. Otherwise space groups as well as crystal structures are going to change.

Small changes in both peak positions and intensities, on the other hand, are implications of lattice parameter changes and phase fraction deviations, respectively. That is why rather than certain site occupancies, phases involved are represented as $(\text{La}_{1-x}\text{Sr}_x)\text{CoO}_3$ and $(\text{La}_{1-y}\text{Sr}_y)_2\text{CoO}_4$ for dual phase synthesis powders in Table 4-8.

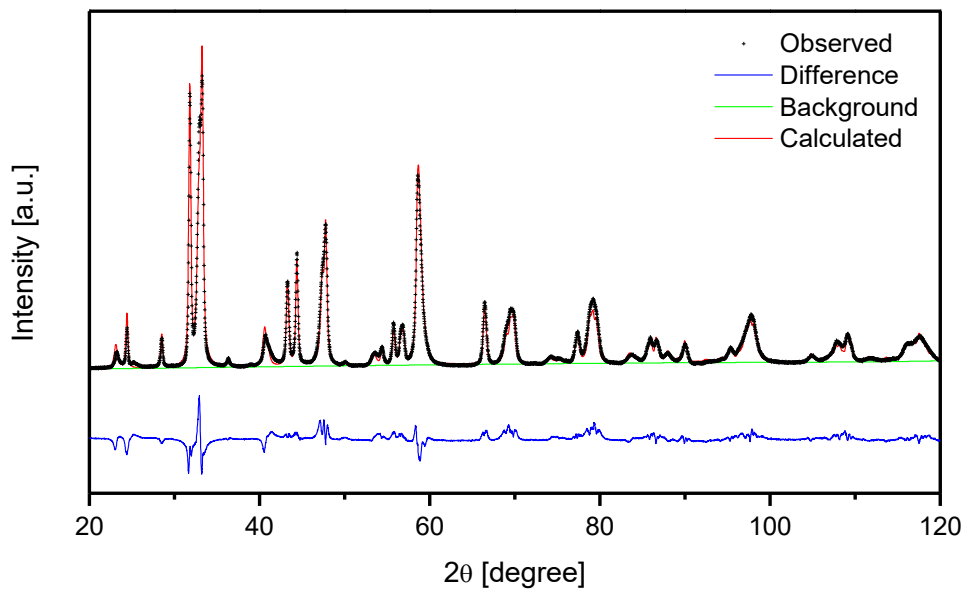


Figure 4-12 Refined pattern of DP-1

Since lattice parameter change is mainly because of A-site Sr occupation difference, site occupations were also aimed to be refined to reasonable values. The first drastic observation in pursuit of this aim was the detection of *insensitivity* of Rietveld refinement analysis to alteration of La:Sr site occupations at least with $\text{CuK}\alpha$ based XRD diffraction data of dual phase *powders* (for pellets sintered at very high temperatures, peaks will be very steep, making refinement easier). A variety of dummy histograms were made on the basis of profile parameters and preferred orientation information found by assuming $x=0.2$ and $y=0.5$ in phases. By keeping these parameters constant, lattice parameters as well as atomic coordinates of La and

Sr were simultaneously refined for setting certain Sr site occupations to variety of values (from 0 to 1) and unfortunately, no change in lattice parameters even for unreasonable site occupations was found. This simply refers to that Rietveld refinement was insensitive to Sr site occupation for, at least, current conditions of X-ray radiation characteristic and/or highly porous low particle size powders. That's why, sequential refinement to dual phase powder patterns were not adopted as the way of *exact determination* of site occupations and obvious conclusion on La:Sr partitioning behavior.

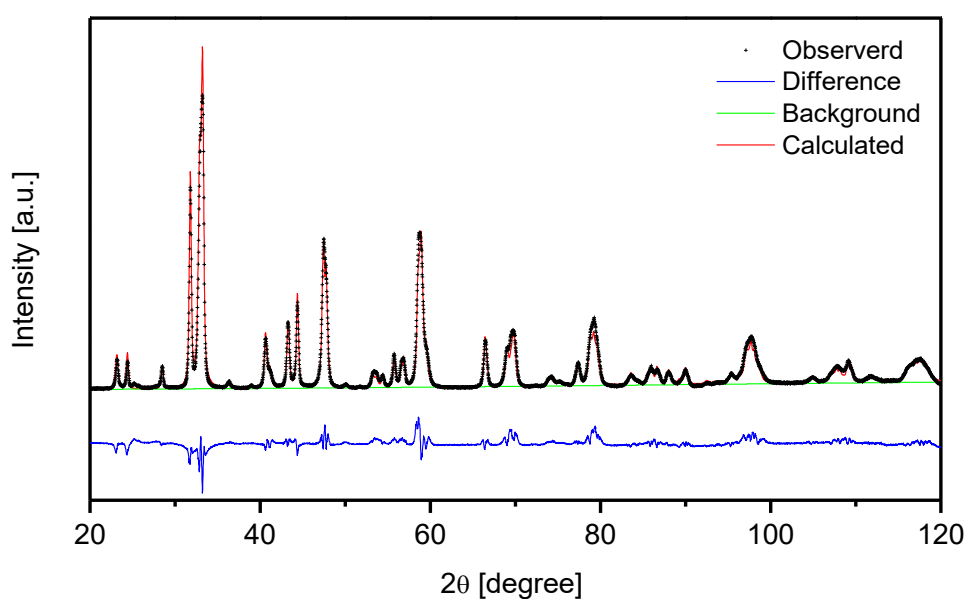


Figure 4-13 Refined pattern of DP-3

Nevertheless, reasonable estimations of La:Sr site occupations based on lattice parameter variations of phases in different powders and comparison of them with respect to literature were possible and made. Lattice parameters of the constituent phases in different dual phase powders are tabulated in Table 4-8. Fitting parameters as well as refined profiles assure lattice parameters.

Table 4-8 Lattice parameters of phases with accompanying fitting parameters

	Fitting Parameters		(La _{1-x} Sr _x)CoO ₃ Lattice Parameters (Å)		(La _{1-y} Sr _y) ₂ CoO ₄ Lattice Parameters (Å)	
DP-5	χ^2	2.096	a	5.438	a	3.803
	R _p	0.0881	b	5.438	b	3.803
	R _{wp}	0.1117	c	13.142	c	12.509
DP-1	χ^2	2.656	a	5.440	a	3.805
	R _p	0.0997	b	5.440	b	3.805
	R _{wp}	0.1259	c	13.176	c	12.510
DP-3	χ^2	2.707	a	5.442	a	3.805
	R _p	0.1034	b	5.442	b	3.805
	R _{wp}	0.1288	c	13.153	c	12.514

At first glance, assumption of a one-to-one correlation between lattice parameter and site occupation seems to reasonable. However, this is not the case for LSC₁₁₃. In this study, differently doped (0.1<x<0.5) LSC₁₁₃ powders were synthesized and lattice parameters detected are illustrated in Figure 4-16 and Figure 4-17. One can see here that while lattice expands in c-direction with increasing Sr, there is a fluctuating behavior in lattice within a-direction. For low (x=0.1) and high Sr content (x=0.5), lattice parameter ‘a’ is below 5.440 Å based on the result of this study. This is not only a finding pertaining to this study but this is also observed in literature [185,191–193]. Literature findings show that from x=0 to x=0.15, lattice parameter in a-direction first increases while after that point it falls whereas the case is reverse within c-direction. Till x=0.15, c decreases and afterwards it restores its higher values as illustrated in Figure 4-16 and Figure 4-17 below. Peak points should not be necessarily x=0.15 but it is seen that there is fluctuation. So, increasing Sr site occupation does not necessarily imply increasing lattice parameter in LSC₁₁₃ as opposed to LSC₂₁₄.

On the other hand, as Sr content increases in tetragonal LSC₂₁₄, lattice enlarges through c-direction and lattice parameter ‘a’ is going to be reduced as an undebatable phenomenon. See Figure 4-14 and Figure 4-15. In Figure 4-14, Figure 4-15, Figure 4-16 and Figure 4-17, black dots represent literature values of single phase powders.

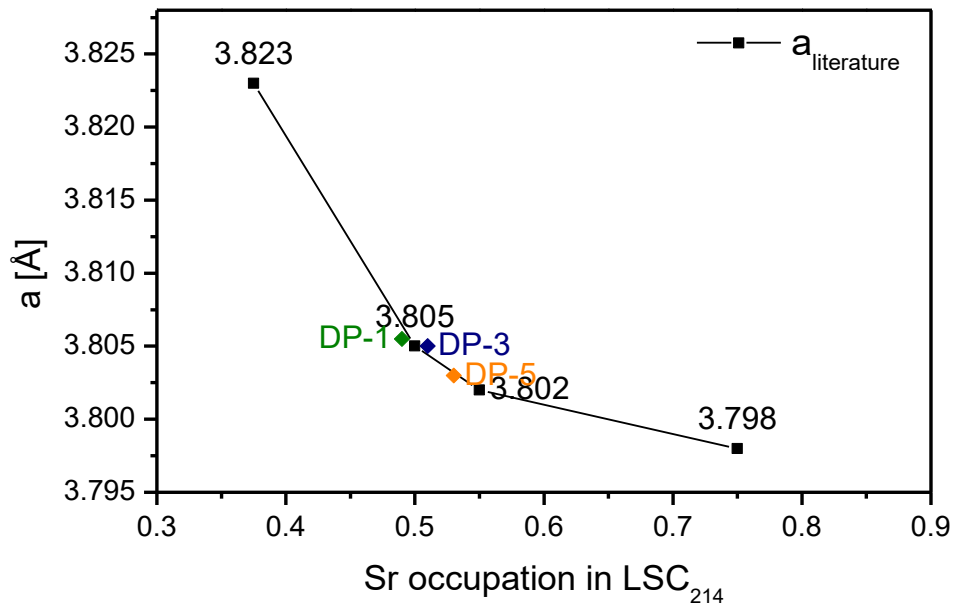


Figure 4-14 Change in lattice parameter a with respect to Sr doping in LSC₂₁₄ [149,186]

In the light of these information, Table 4-8 can be analyzed. The first notable observation was almost unchanged lattice parameters of LSC₂₁₄ as opposed to LSC₁₁₃, lattice parameters of which showed relatively wide variation. This observation implies stationary site occupation for LSC₂₁₄ along with variation of it in case of LSC₁₁₃, that is to say that from synthesis to synthesis and phase fraction to phase fraction, a site occupation was preserved in LSC₂₁₄. Furthermore, high number of Rietveld refinement iterations on the basis of tailoring various parameters yielded drastic changes on lattice parameters of LSC₁₁₃ and no change in lattice parameters of LSC₂₁₄, making this study confident on lattice constant of LSC₂₁₄.

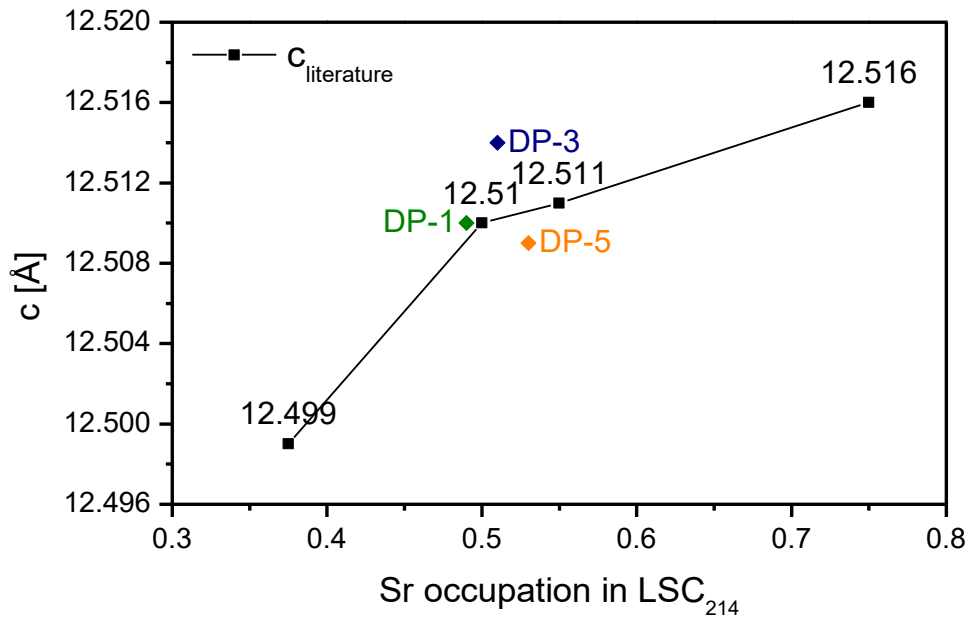


Figure 4-15 Change in lattice parameter c with respect to Sr doping in LSC_{214} [149,186]

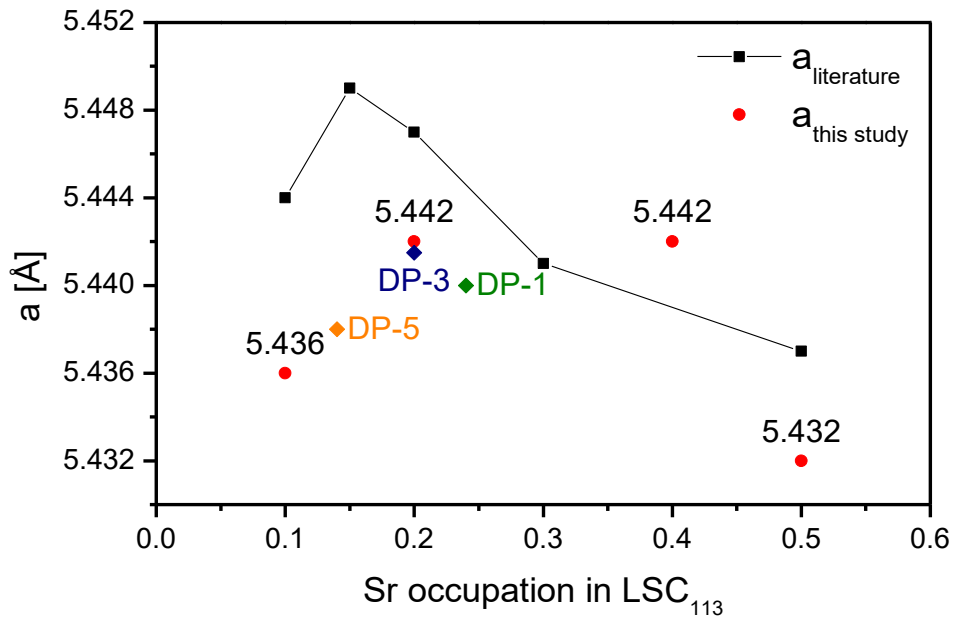


Figure 4-16 Change in lattice parameter a with respect to Sr doping in LSC_{113} [191,192]

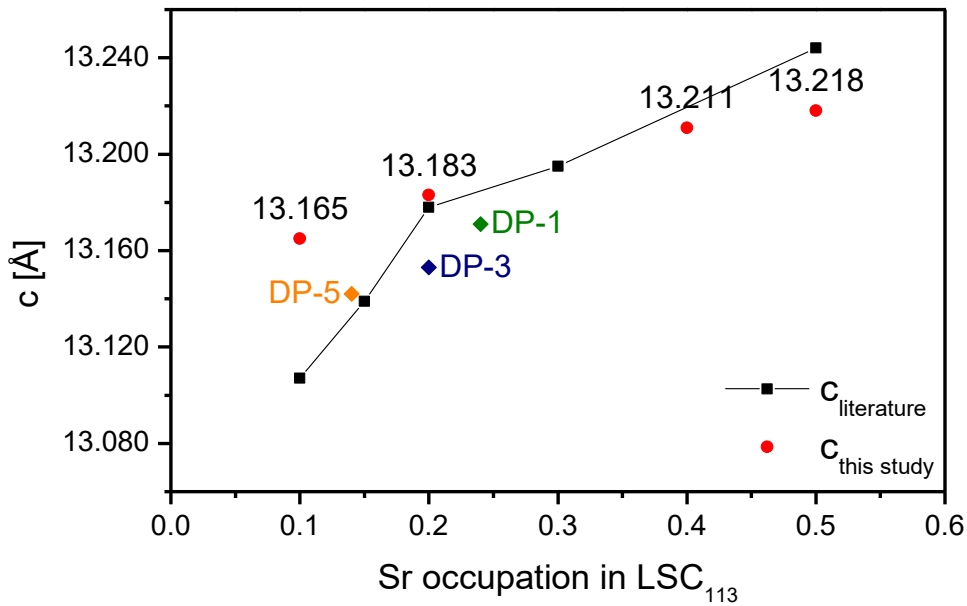


Figure 4-17 Change in lattice parameter c with respect to Sr doping in LSC_{113} [185,193,194]

Thanks to undebatable lattice parameters alteration regime in LSC_{214} , we can *roughly* set Sr site occupation to the lattice parameters. When the lattice constants obtained from single phase LaSrCoO_4 powder ($a=3.805 \text{ \AA}$, $c=12.506 \text{ \AA}$) and sluggish change in lattice parameter 'a' are considered, it can be asserted that LSC_{214} in DP-1 and DP-3 powders has almost $y=0.5$ corresponding to LaSrCoO_4 stoichiometry. DP-5 powder, on the other hand, has lower value of 'a' which is apparently corresponding to *slightly* higher Sr content than $y=0.5$ (see Figure 4-14 and Figure 4-15). Obviously, any selected Sr site occupancy for one phase will automatically dictate a certain Sr site occupancy for the other phase due to initially added constant cation amount in the beaker (see Table 4-11). Therefore, setting a certain y value in LSC_{214} *must* correspond to a reasonable x in LSC_{113} . Figures above were generated with this restriction.

Table 4-9 Weight and phase fractions of phases in each dual phase synthesis

		DP-5	DP-1	DP-3
LSC₁₁₃	wt%	0.328	0.432	0.532
	X ₁₁₃	0.412	0.533	0.627
	Expected X ₁₁₃	0.400	0.500	0.600
LSC₂₁₄	wt%	0.675	0.568	0.468
	X ₂₁₄	0.588	0.467	0.373
	Expected X ₂₁₄	0.600	0.500	0.400

Based on these reasonable site occupation estimations which have also been correlated with lattice parameters either found in literature or detected in this study, weight fractions were extracted from refinement (Table 4-9). Weight fractions are not altered significantly with changing Sr site occupations, which makes weight fraction output of Rietveld analysis a confident reference. Still, cross-correlation between weight fraction (its resultant mole fraction output that must also be compatible with beaker based n_{La}/n_{Sr} ratio) and Sr site occupation was concerned and eventual site occupations were estimated accordingly. In pursuit of this task, n_{La}/n_{Sr} mole fraction in initial solution was determined to be an ultimate reference. Final site occupancy estimations, which was set arbitrarily and by which Table 4-9 was formed, are manifested in Table 4-10.

Table 4-10 Refined cation stoichiometry of phases

	x	y	LSC₁₁₃	LSC₂₁₄
DP-5	0.14	0.53	(La _{0.86} Sr _{0.14})CoO ₃	La _{0.94} Sr _{1.06} CoO ₄
DP-1	0.24	0.49	(La _{0.76} Sr _{0.24})CoO ₃	La _{1.02} Sr _{0.98} CoO ₄
DP-3	0.20	0.51	(La _{0.80} Sr _{0.20})CoO ₃	La _{0.98} Sr _{1.02} CoO ₄

It is notable to indicate that strength of fit between calculated and observed patterns manifested in Figure 4-11, Figure 4-12 and Figure 4-13, makes lattice parameter values highly confident but degree of current fitting strength is not strong enough to *exactly* converge Sr site occupancies to actual undebatable values. Hence, although site occupancies have been set to *reasonable* values as given in Table 4-10, their

values are approximate and phase fractions have been calculated accordingly. This must be kept in mind.

Table 4-11 n_{La}/n_{Sr} ratio in beaker used as reference for checksum of site occupancies set

n_{La}/n_{Sr} ratio in beaker	
DP-5	1.35
DP-1	1.50
DP-3	1.69

Refinements seem to be well assured in all aspects, including phase fractions, lattice parameters and their relevance to corresponding Sr site occupancies in both phases. After assurance of refinements, its results and implications can be evaluated and discussed.

First of all, formation of LSC_{113} phase has apparently dominated the formation of Ruddlesden-Popper structure in all cases. Extend of this domination is least in DP-5 while it is well evident in other powders. Herein, one can infer that formation of LSC_{113} is more facilitated and easier with respect to LSC_{214} . Anyway, during single phase synthesis-calcination process, it was observed that minimum possible calcination temperature of single phase LSC_{214} was 800 °C whereas single phase LSC_{113} yielded well crystalline XRD pattern even calcination temperature of 740 °C. Thus, it can be concluded that LSC_{113} formation starts earlier than LSC_{214} which brings about domination of LSC_{113} formation within synthesis of two phase system. This confirms phase fraction calculations via Rietveld refinements.

Second, in structural analyses, certain La:Sr site occupancies were attempted to be revealed. However, though reverse was assumed, it should be kept in mind that there might not be a unique Sr site occupancy for each phase in all dual phase powders. In fact, such *Sr site occupancy differential* possibly caused by secondarily formed phases is thought to induce inevitable partial inconsistencies of lattice parameters and their relevance to site occupations as manifested in Figure 4-15. Whatsoever was attempted,

at least in one option among a and c-directions in one of the both lattices exhibited incompatibility in lattice parameter versus site occupancy diagrams. When the degree of fit among refinement and low fitting parameter values are considered, wrong calculation of lattice parameters as result of refinements is unlikely to be the reason for such incompatibilities. Probable reason is Sr site occupation differential. Detecting Sr differential quantitatively could be done by TEM analysis but in this case it is important to state and be sure about how representative of current TEM image obtained is for complete powder.

All the powders and phases involved are obtained via solution based method which simply implies nucleation-growth process in which one phase (primarily formed) constitutes nucleation site for other. Nucleation necessity of one from other may well cause some sort of divergence in lattice parameters, which is good news for interface maximization since this refers to preferred formation of phases from others surface sites. In this way, all the events are matter of La:Sr partitioning behavior during nucleation-growth from dried amorphous gel to final crystallinity, referring to atomic motilities of La and Sr in their media. Thus, Synchrotron radiation as function of increasing temperature and high number of sequential refinement is prospective solution of final site occupation determination but this would constitute a source of another complete study.

4.2.2. In Situ EIS Cell Responses

Hetero interface of $\text{LSC}_{113/214}$ can be and has been generated till now by varied sophisticated methods [11,21,88,122]. Tough success of these ways are undebatable, they are success-oriented expensive routes, making them unsuitable for massive applications. In this sense, dual phase synthesis of powders *from one unique solution* in a beaker was expected to enhance hetero interfaces through complete bulk with well cheaper and easy route. Obviously, this is possible if nanocrystals of phases penetrate to each other very well. Particle penetration criterion is not sufficient. Beyond that, these particles should be below temperature-specific critical utilization lengths, below which overall ORR is limited only by surface reduction of oxygen molecules.

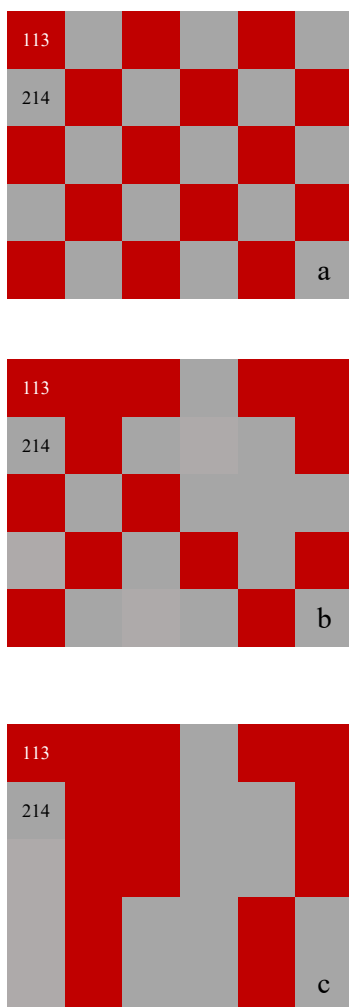


Figure 4-18 Particle penetration scenarios schematic illustrations (a) Extreme maximization, (b) intermediate penetration and (c) as if physical mixture

In this picture, there would be final extreme hetero interface between nanocrystals of phases and since particles are also below critical utilization length, l_{δ} , oxygen diffusion would not be a source of resistance, all the reaction limitation would be caused by surface/interface reduction of oxygen, which has already been facilitated by extreme generation of $\text{LSC}_{113/214}$ hetero interface and accelerated ORR there. Figure 4-18 exhibits good illustrations for possible scenarios regarding hetero interface formations.

Obviously, one pot synthesis was successful. But what about particles size, distribution and penetration? If the final case of powders is (c) in Figure 4-18, then dual phase synthesis is said to be unsuccessful and DP synthesis corresponds to physical mixing of individually synthesized powders, invalidating dual phase synthesis. If, however, the case corresponds to (a) in Figure 4-18 accompanying with sizes below l_δ , then surface limited behavior could be attained from very thick cathodes (namely more than 20-30 μm thicknesses). Attaining such surface limited behavior with conventional thick porous cathodes without use of sophisticated thin film deposition techniques would be first in literature and capable of significantly reduce both cost and operation temperature of SOFC. Although homogeneous mixing manifested in Figure 4-18(a) is an idealized scenario, it is still worthwhile to attempt when its possible consequences are taken into considerations.

Clarification of aforementioned motives in pursuit of dual phase synthesis is possible -at least qualitatively- by in situ EIS analysis. Symmetric cells of dual phase synthesis powders were derived following the procedures explained in 4.2.1 and EIS analyses were done in the light of experimental parameters explained in 4.1.2.5.

For $(\text{La}_{0.8}\text{Sr}_{0.2})\text{CoO}_{3-\delta}$, critical utilization length is calculated to be around 500 nm at 400 °C [43]. If particle penetration is extremely high as illustrated in Figure 4-18(a), EIS signals must demonstrate interface ORR limited behavior even at this temperature and even for 70 μm cathode thickness. Such a result would be outstanding but this is not the case. It is apparent from the Figure 4-19 that, at 400 °C, P_{O_2} differential has no effect on EIS spectra. It is understood that particle penetration is not high enough for 400 °C since if interface maximization were sufficiently advanced, there would be P_{O_2} dependency in EIS spectra.

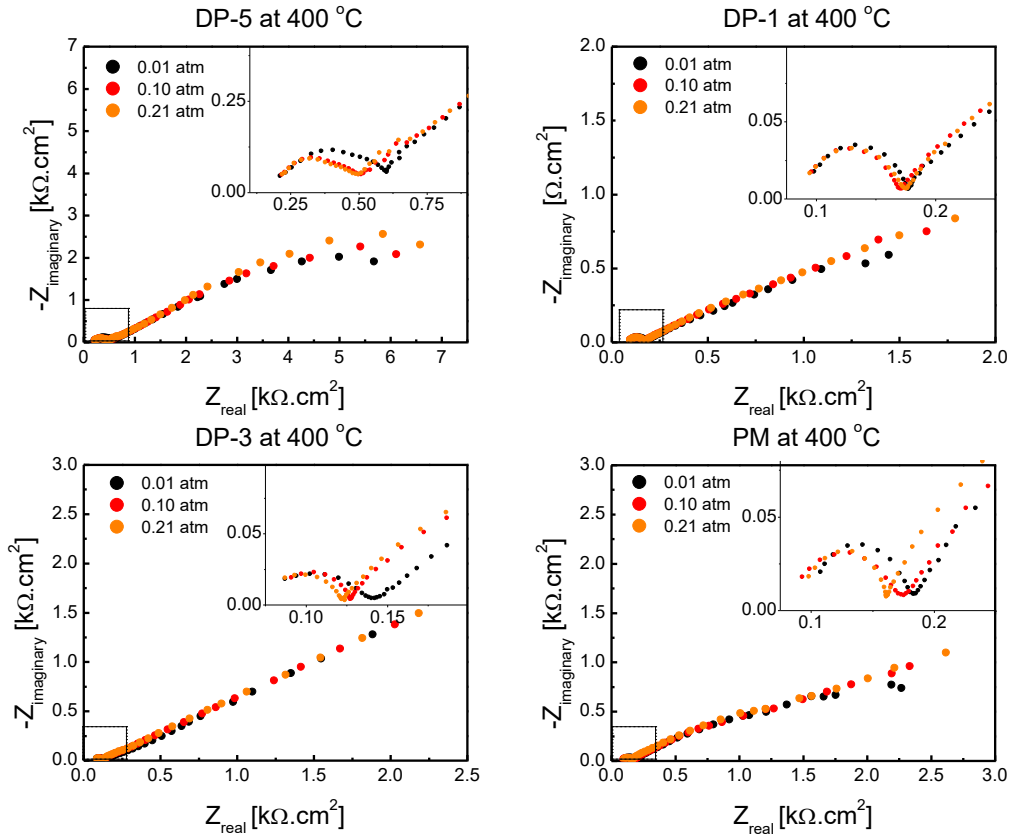


Figure 4-19 400 °C EIS responses of symmetric cells of DP-5, DP-1, DP-3 and PM with respect to differential P_{O_2}

Both dual phase series and physical powder mixtures exhibited resistance caused by oxygen ion transfer at cathode-electrolyte interface with a combined Warburg like behavior (see Figure 4-19). This is reasonable since oxygen diffusion is expected to be sluggish at 400 °C ($D_{(La_{0.8}Sr_{0.2})CoO_3}^* = 10^{-15} cm^2/s$ at 400 °C [43] and $D_{La_2CoO_4}^* = 2.5 \times 10^{-8} cm^2/s$ at 500 °C [146]) and cathode thickness already implies diffusion limited behavior. Combined effect of them seems to manifest itself as a huge cell resistance independent from P_{O_2} and far away from requirements for utilization, along with diffusion limited behavior. These are not surprising for 400 °C. Further temperatures are prone to make difference since l_δ is getting higher with increasing temperatures. But before going further, details are worthwhile to be criticized in Figure 4-19.

Change in the position of high frequency arc associated with oxygen ion transfer at electrode-electrolyte interface is definitely because of slight changes in the thickness of GDC electrolyte. Another reason may be change in ionic/electronic conductivity properties of GDC pellet with varying P_{O_2} . Change in size of it on the other hand is dependent upon many parameters, most principle of which is the degree of adhesion between cathode and electrolyte. Nonetheless, these deviations are not of great importance for all specimens and they will not be evaluated once again.

A closer look at the Figure 4-19 also attracts attention to EIS spectra of DP-5, which is drawn within higher values of x and y axes. This, at first glance, gives rise to “higher” resistance and capacitance in DP-5. But whereas in case of DP-1, DP-3 and PM, lower frequency responses converge to Warburg like behavior (an endless linear line), in DP-5 spectra, EIS response is converging to *finalize* a complete arc. This is an implication of more facilitated process on contrary to appearance. This makes sense since particle penetration is poor for 400 °C, cathodes are thick and LSC₁₁₃ phase is poor in terms of oxygen vacancy concentration at 400 °C [195], equivalent to low ionic conductivity. Under the conditions in which pure diffusion limited behavior prevails, higher LSC₁₁₃ content corresponds to higher resistances. However, LSC₂₁₄ has interstitial and faster diffusion [151], since DP-5 powder involves more LSC₂₁₄, it more easily converged to finalize a complete arc and the other cells were incapable of this, expressed as Warburg. Comparison of single phase LSC₁₁₃ and LSC₂₁₄ supports this assertion. LSC₁₁₃ especially exhibited a proper Warburg in Figure 4-20. DP-5 signals seem to be between single phase LSC₁₁₃ and LSC₂₁₄ but rather seem to be converging to LSC₂₁₄ response as can be seen from Figure 4-20. The remaining cell responses seem to obey lever rule.

Finally, slightly higher capacitances with increasing P_{O_2} at 400 °C EIS spectra is probably because higher P_{O_2} means lower oxygen vacancy concentration in LSC₁₁₃ and more accumulation of raised interstitial oxygen within LSC₂₁₄ at this low temperature [152]. This cumulative effect will change in following temperatures for sure with the dominant effect of diffusion. It is apparent that by means of dual phase synthesis, it is not possible to reduce operation temperature to 400 °C, which is critical threshold for long term stability [18]. Such an astonishing result would be

revolutionary anyway. But increasing temperatures can make difference. 500 °C is the temperature at which hetero interface formation corresponds to an enhancement in overall ORR.

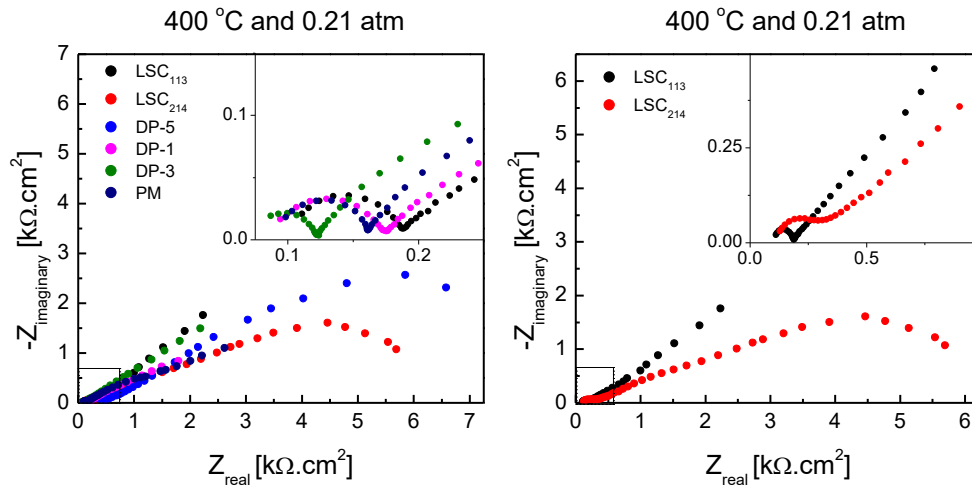


Figure 4-20 Comparison of all EIS spectra (left) and that of single phase cathodes at 400 °C and 0.21 atm P_{O_2}

As can be seen from Figure 4-21, all DP series cells as well as physical mixture exhibit depressed capacitances corresponding to probable arcs to be finalized at lower resistance than LSC_{113} or LSC_{214} . Their spectra are not between two single phase responses contrary to 400 °C spectra and they hence do not imply lever rule. This can be explained by hetero interfacial enhancement. Similar to previous spectra, LSC_{113} still obeys Warburg element properly. DP-5 once more is more likely to finish the arc. Oxygen partial pressure has no significant effect on EIS responses, too, except for lowering capacitive effect, logic behind of which has already been explained in 400 °C spectra evaluations (see Figure 4-22). DP-1 and PM show the lowest capacitances and the arcs which are more likely to be finalized early, meaning lower cathode resistance at 500 °C. But it is hard to state that this case is originated from more successful interface maximization that these syntheses can do in sub-micron scale. But somehow, whether in the form of contact between single phase agglomerates in tens of microns' scales with each other or in the form of hetero-interface creation during

nucleation growth process of solution based synthesis, there releases a catalytic effect caused by two-phase existence at 500 °C.

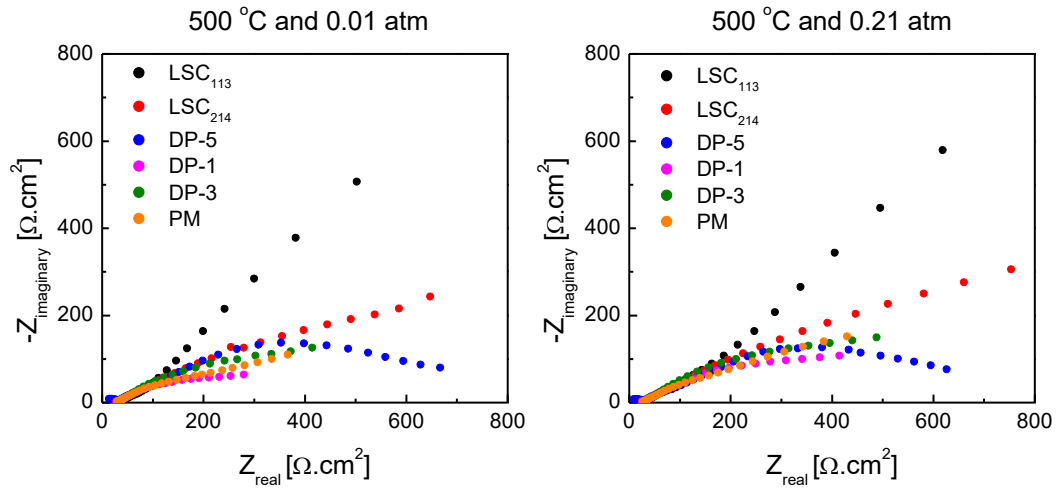


Figure 4-21 Comparison of all cells at 500 °C with varying oxygen

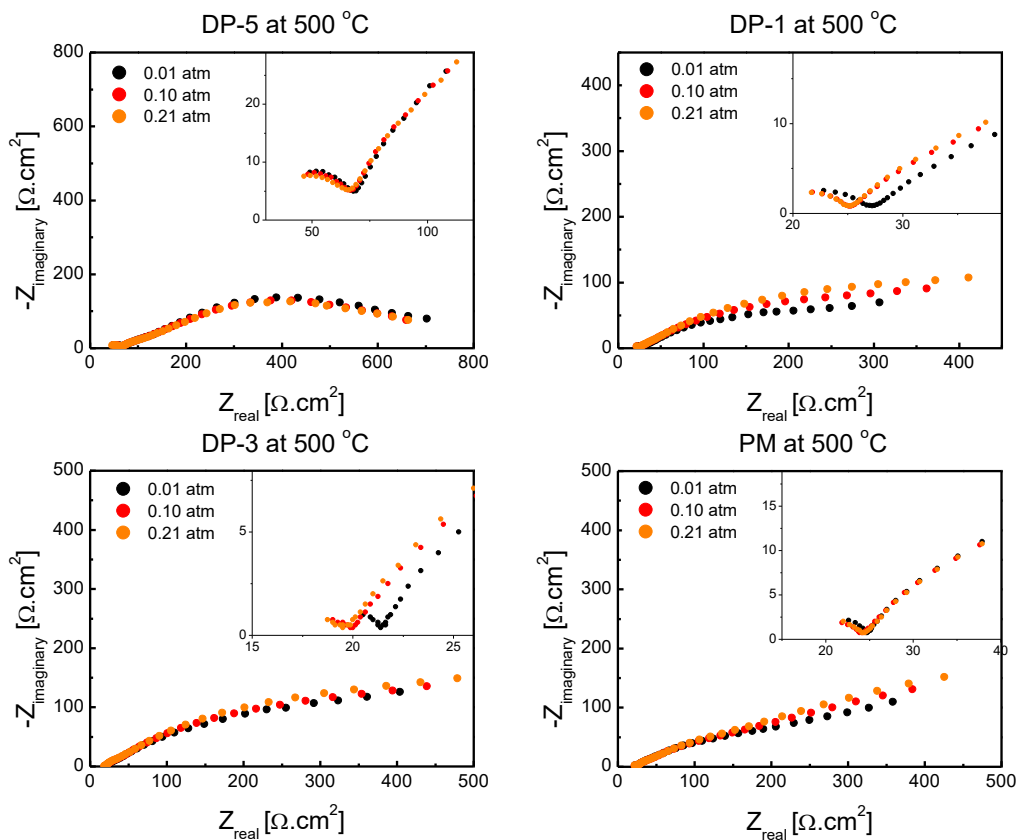


Figure 4-22 500 °C EIS responses of symmetric cells of DP-5, DP-1, DP-3 and PM with respect to differential P_{O_2}

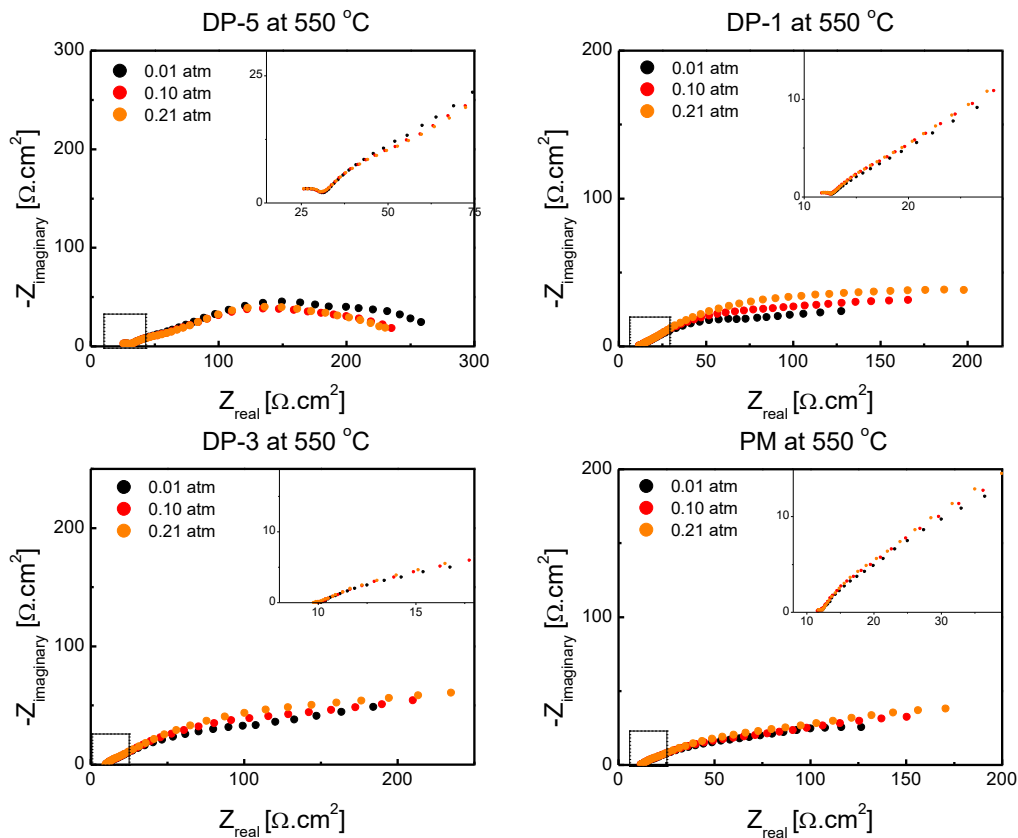


Figure 4-23 550 °C EIS responses of symmetric cells of DP-5, DP-1, DP-3 and PM with respect to differential P_{O_2}

In previous comments, made in evaluation of EIS responses in 400 °C, slight increase in capacitance with increasing P_{O_2} was attributed to cumulative effect of both phases and it was stated that this regime would change in following temperatures. 550 °C was such a temperature; spectra did not necessarily show higher capacitances with increasing P_{O_2} . Contrary, in DP-5, capacitance was higher in 0.01 atm than it was in 0.21 atm as illustrated in Figure 4-23. While lowering P_{O_2} induces vacancy formation at this temperature within LSC_{113} phase and facilitates oxygen transport, its effect on reducing the diffusion of interstitial species is more dominant in DP-5. Since other cells include more LSC_{113} , effect of increasing P_{O_2} is more drastic with respect to 400 °C spectra; 0.21 atm capacitances deviate more than previous temperatures. This is because higher temperatures mean a transformation of charge compensation mechanism from electrical to ionic.

Another characteristic of 550 °C is disappearing of ion exchange resistance at cathode-electrolyte interface. Hetero interface enhancement is once more valid for 550 °C, too. Nonetheless, it is still debatable to point out which multi-phase cells show better performance. Cells involving more LSC₁₁₃ phase are situated in more advantageous position in 0.01 atm P_{O_2} since with increasing temperature, oxygen vacancies formed meet more easily with interstitials oxygen of LSC₂₁₄ causing more depressed and reduced arcs. This is manifested in Figure 4-24, in which 0.01 and 0.21 atm responses of all cells are compared. It is seen that DP-3, DP-1 and PM, involving more LSC₁₁₃, cell responses are slightly reduced while 214 and DP-5 cells exhibited slightly enhanced arcs. Similar situation will also be seen in 600 °C.

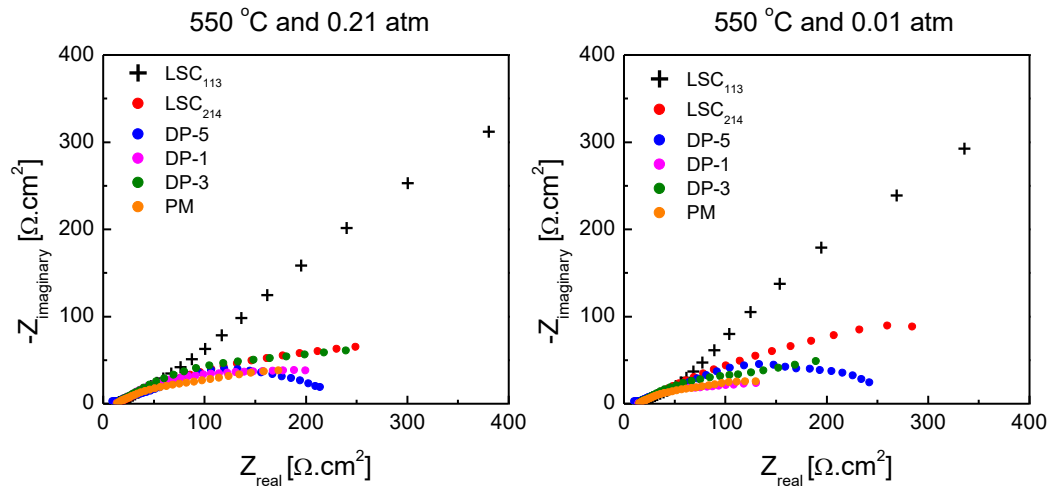


Figure 4-24 Comparison of all cells at 550 °C with varying oxygen

The only principle alteration in 600 °C spectra is the reduced ASR values with respect to spectra of 550 °C, which is not surprising. P_{O_2} dependencies of different cells are almost same for each cell (compare Figure 4-23 and Figure 4-25). There is still an enhancement in overall ORR caused by hetero interface contacts except for DP-3 as given in Figure 4-26. EIS response of DP-3 is between LSC₁₁₃ and LSC₂₁₄ at 600 °C with higher arc than LSC₂₁₄. Surface Sr segregation is expected to have an effect to see such response with increasing temperatures since LSC₁₁₃ is highly prone to segregation and DP-3 involves significant LSC₁₁₃. But this is, on the other hand, an

indication for losing enhancing effect of hetero interface with increasing temperatures after intermediate range is exceeded.

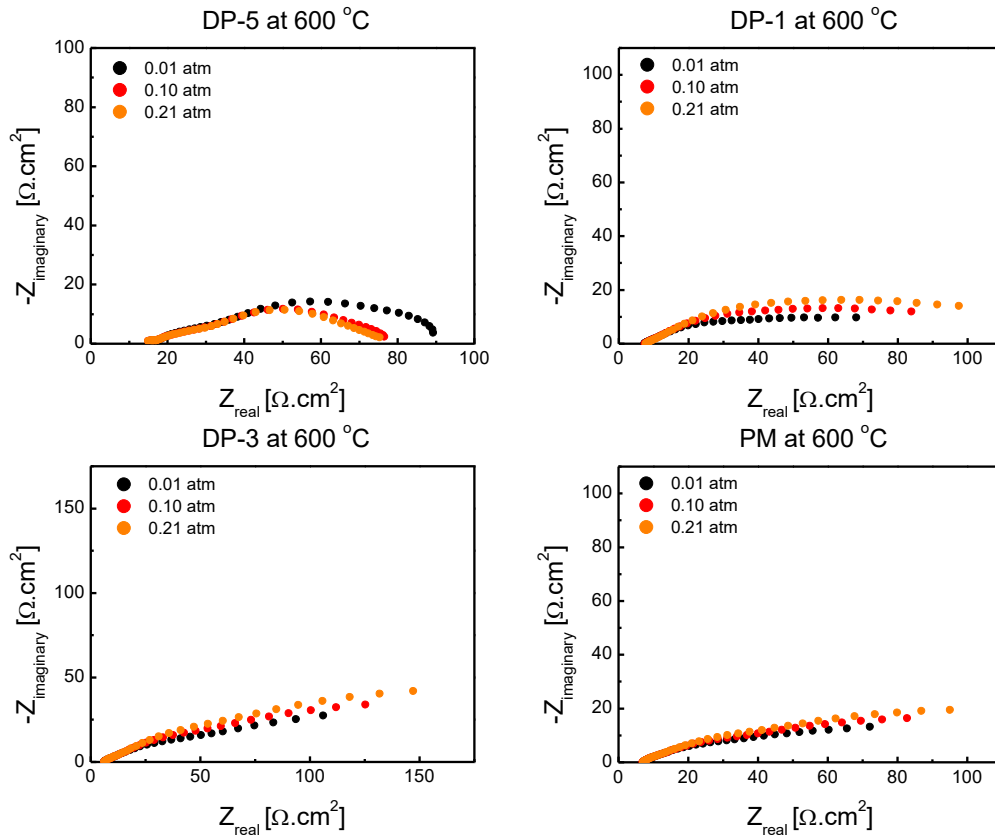


Figure 4-25 600 °C EIS responses of symmetric cells of DP-5, DP-1, DP-3 and PM with respect to differential P_{O_2}

The lowest recorded ASR at 600 °C is observed in DP-5, as a rich cathode in terms of LSC_{214} constituent. It is $60 \Omega\text{cm}^2$. Nevertheless, use of LSC_{214} at this temperature is more advantageous than use of DP-3 cathode. But the other cell responses are still in advantageous position with respect to single phase powders.

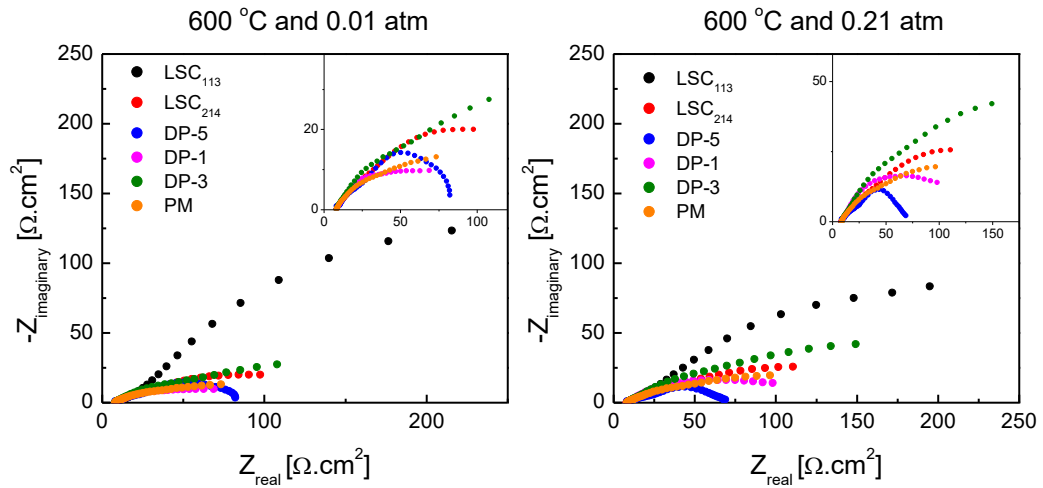


Figure 4-26 Comparison of all cells at 600 °C with varying oxygen

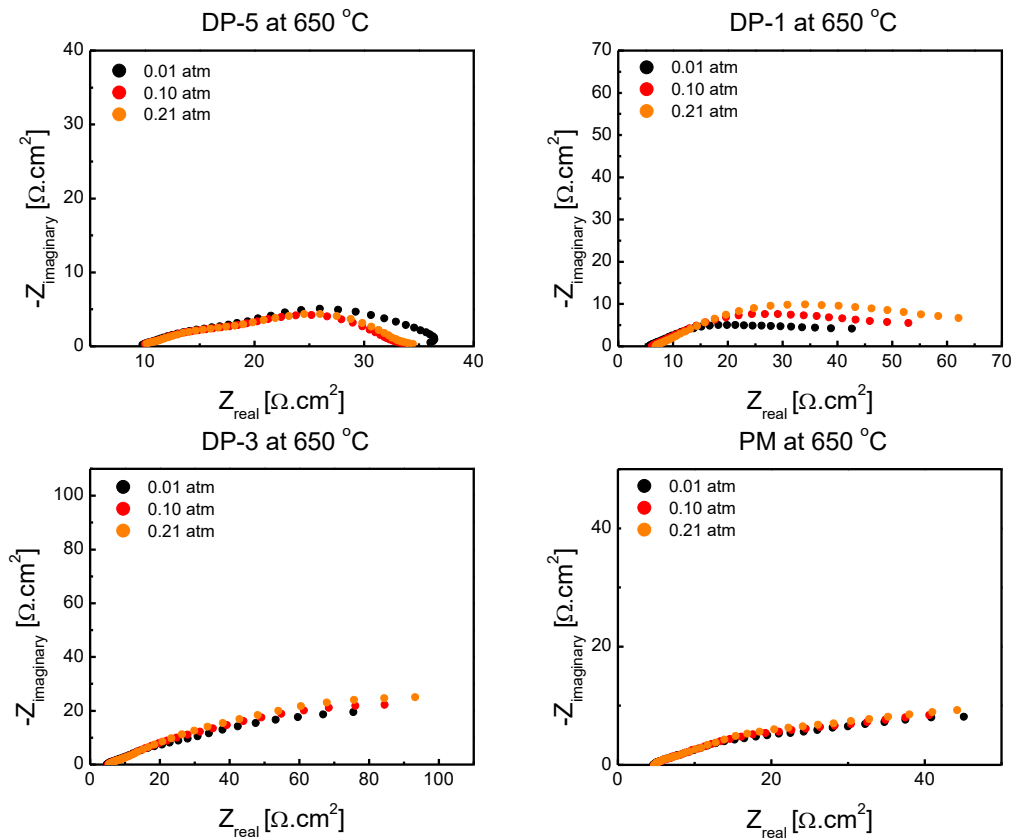


Figure 4-27 650 °C EIS responses of symmetric cells of DP-5, DP-1, DP-3 and PM with respect to differential P_{O_2}

At 650 °C, significant reduction in LSC₂₁₄ arc is accompanied with quite high increase in DP-3 resistance. DP-3 response converges to LSC₁₁₃. P_{O_2} dependency is almost same as it was for previous cathodes; higher oxygen content of ambient meant slightly higher capacitances as illustrated in Figure 4-27 above.

As it was stated, surface Sr segregation is important reason for this ASR increase but it should also be emphasized that with increasing temperatures, electrical conductivity of LSC₁₁₃ must decrease since vacancy formation mechanism for charge balance is now more operative at such temperatures. Low electrical conductivity can't catalyze well ORR and this caused increasing ASR in cathodes including more LSC₁₁₃. That's why hetero interfacial ORR enhancement is operative only at intermediate temperature ranges. Examinations at 650 and 700 °C played role of demonstrating that.

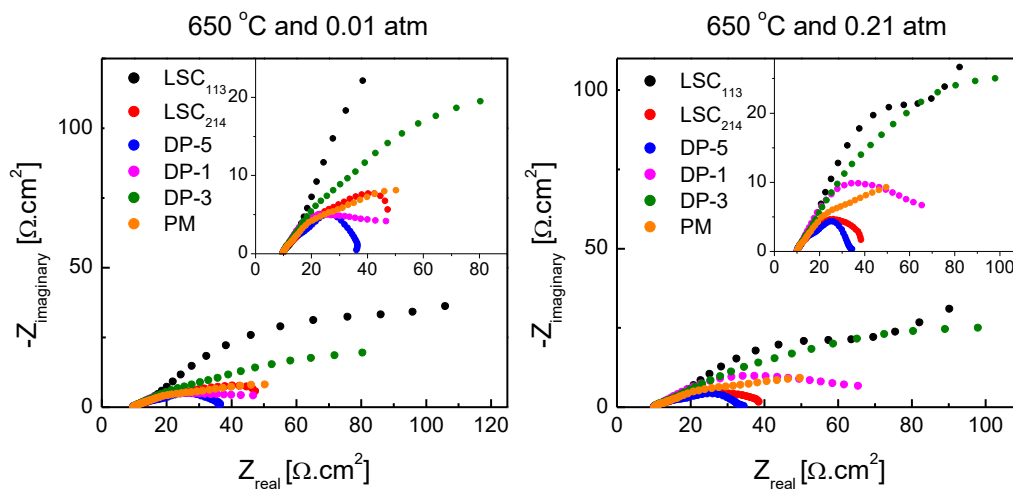


Figure 4-28 Comparison of all cells at 650 °C with varying oxygen

The lowest ASR at 650 °C belongs to DP-5. In fact, at this temperature, coexistence of each phase is advantageous only in DP-5 cathode. Otherwise, the all other cathodes become useless with respect to utilization of LSC₂₁₄ single phase cathode. It should be at this point underlined that if the cathode thickness would be lower than that of these cathodes, other cathodes having different phase fractions than DP-5 could also be

advantageous. Nonetheless, many probable unknown parameters may also alter the situation drastically. Therefore, focusing on one of them is pointless.

Unexpectedly, inverse relationship with P_{O_2} as an implication of surface signals was detected in LSC₂₁₄ at 650 °C. Figure 4-29 illustrates a interfered surface ORR related arc changing inversely with P_{O_2} . This is reasonable since critical utilization length of LSC₂₁₄ is well high. As an exceptional case, surface signals were detectable at this conditions. But this is rare situation. In general, surface signals are non-detectable with these thick cathodes.

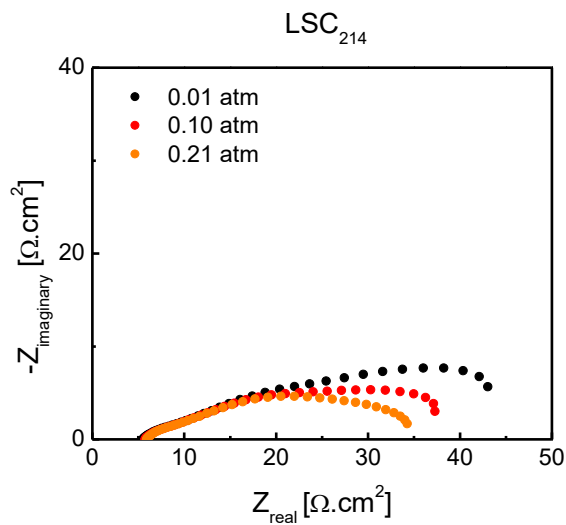


Figure 4-29 LSC₂₁₄ response at 650 °C with varying P_{O_2}

The ultimate examination temperature was 700 °C. The most drastic conclusion that 700 °C examinations exhibited is pointlessness of dual phase synthesis utilization at this stage. After that point, ASR of LSC₂₁₄ is the lowest anymore. Moreover, even at such a high temperature, any of the ASR observed is not sufficient to satisfy requirement of 0.15 Ωcm² [1]. The lowest one belonging to LSC₂₁₄ is 9.55 Ωcm². This is remarkable consequence.

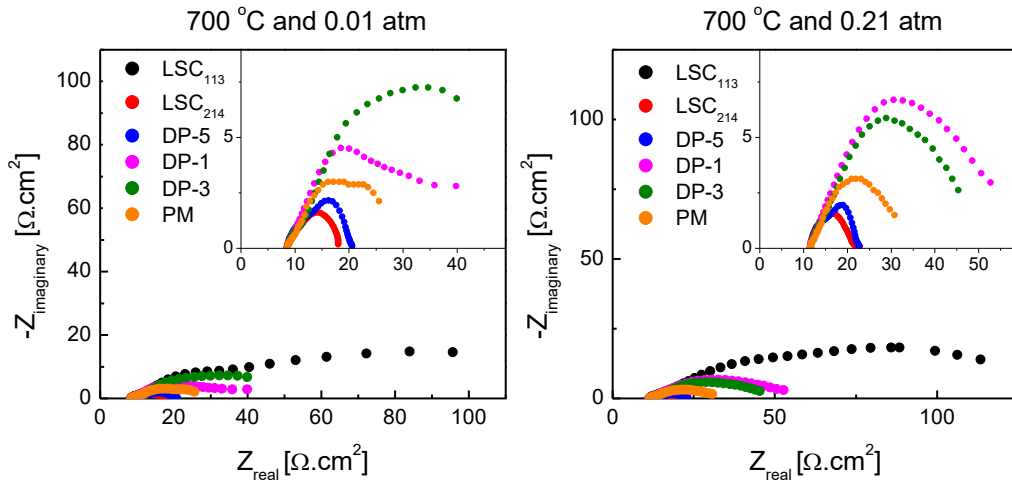


Figure 4-30 Comparison of all cells at 700 °C with varying oxygen

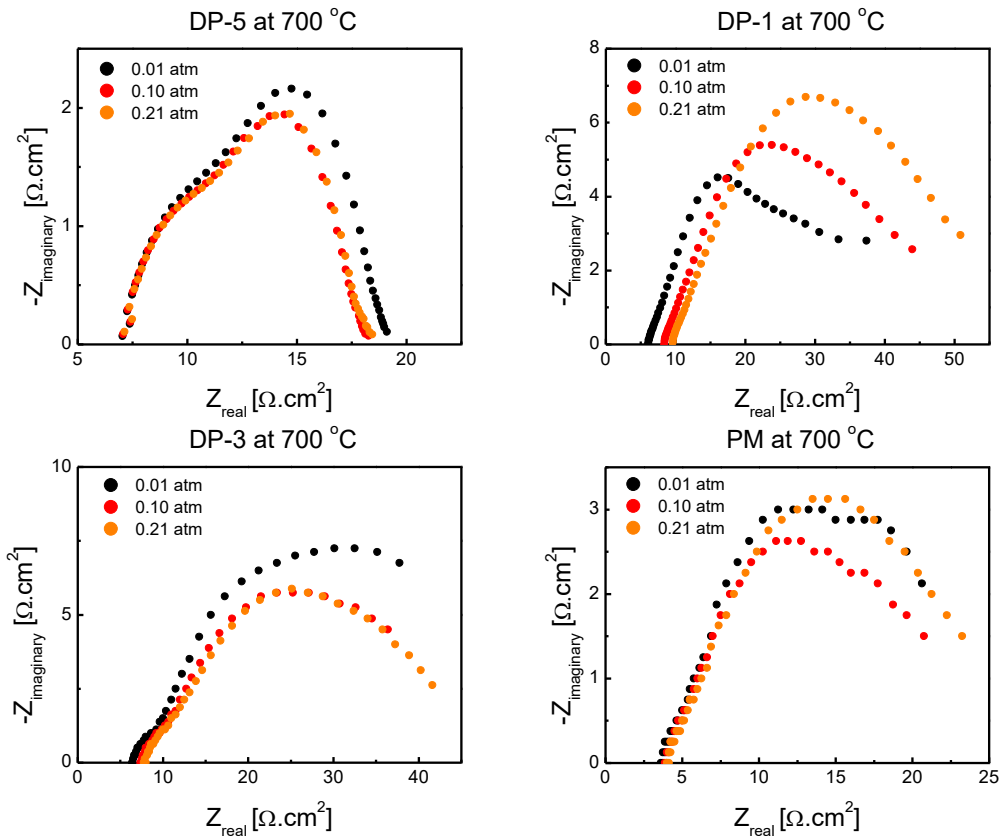


Figure 4-31 700 °C EIS responses of symmetric cells of DP-5, DP-1, DP-3 and PM with respect to differential P_{O_2}

As can be seen from the all spectra, starting point of arcs in Z_{real} was non-zero. This resistance without any imaginary contribution is ionic resistance caused by GDC electrolyte (ionic conductor). As the first time at 700 °C, resistance caused by electrolyte is changing with respect to P_{O_2} . Higher P_{O_2} corresponded to slightly higher ASR as illustrated in Figure 4-31. When it is considered that GDC could unfortunately be electrically conductive depending upon conditions [10] and total conductivity of it decreases with increasing P_{O_2} , which is manifested as higher ASR with higher P_{O_2} , EIS responses make sense [196]. Especially in DP-1, increasing ASR of GDC with is apparently observed.

700 °C was the last probable temperature at which surface limited behavior would be observed since critical utilization length at this temperatures is significantly bigger than low temperature regimes; combination of $D_{(La_{0.8}Sr_{0.2})CoO_3}^* = 10^{-9.75} \text{cm}^2/\text{s}$ and $k_{(La_{0.8}Sr_{0.2})CoO_3}^* = 10^{-6.8} \text{cm}/\text{s}$ at 700 °C [43] yields 11.2 μm critical utilization length. This is quite more in case of LSC₂₁₄ oxides [146]. This means that even if agglomerates are around 10 μm , surface limited behavior is expected to be observed but this did not happen.

To sum up, the EIS responses of dual phase synthesis powders, electrochemical behaviors of symmetric cells could be classified into four different regimes as a function of temperature. In the first regime prevailing at 400-500 °C interval, EIS responses mimic rule of mixture. In the second regime (500-550 °C), dual phase powders have performance better than single phases but equivalent to physically blended powder. Third regime, prevailing at 550-650 °C, is the only one at which even better performances of dual phase powders than physically mixed one was observed. In the last regime (650-700 °C), whether in the form of physical blending or dual phase synthesis, co-existence of two phase structure becomes pointless such that single phase LSC₂₁₄ has the best cathode performance. The regimes of these different performances are illustrated in Figure 4-32.

The observations reported above will be discussed with respect to three aspects. These are i) scale of structure in dual phase synthesis, ii) site occupancy in one pot synthesis and iii) the relevance of EIS responses to cathode thicknesses.

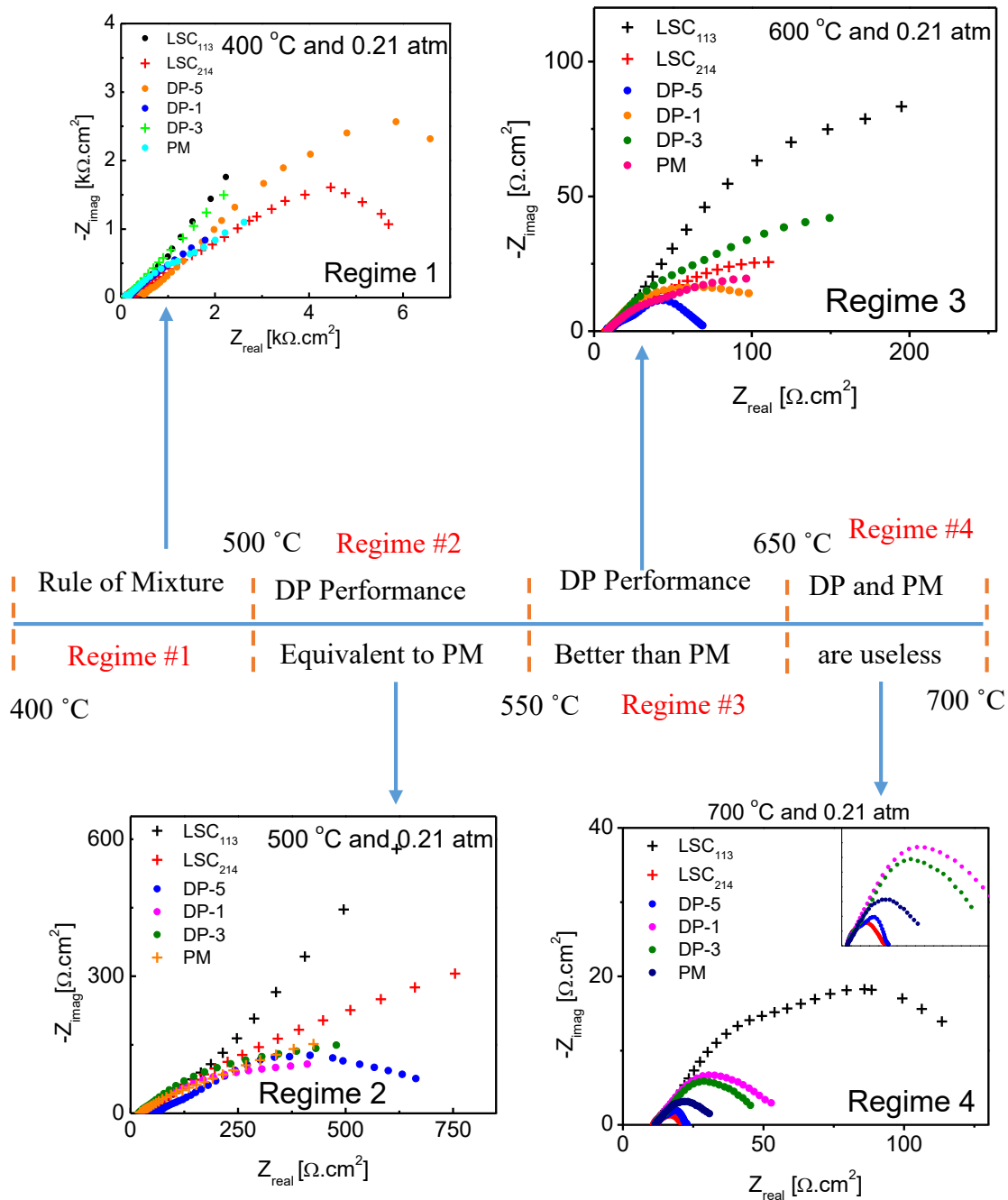


Figure 4-32 A summary of electrochemical behaviors of symmetric cells

The first issue is the scale of final structure in dual phase powders and its relevance to cathode performances. Figure 4-32 manifests that beneficial effect of dual phase synthesis over physical mixture was observed only in the temperature range of 550-650 °C and the degree of the enhancement is modest. It is, therefore, qualitatively

inferred that degree of the hetero interface formation is modest even in case of dual phase synthesis. This aspect was checked by EDS mapping.

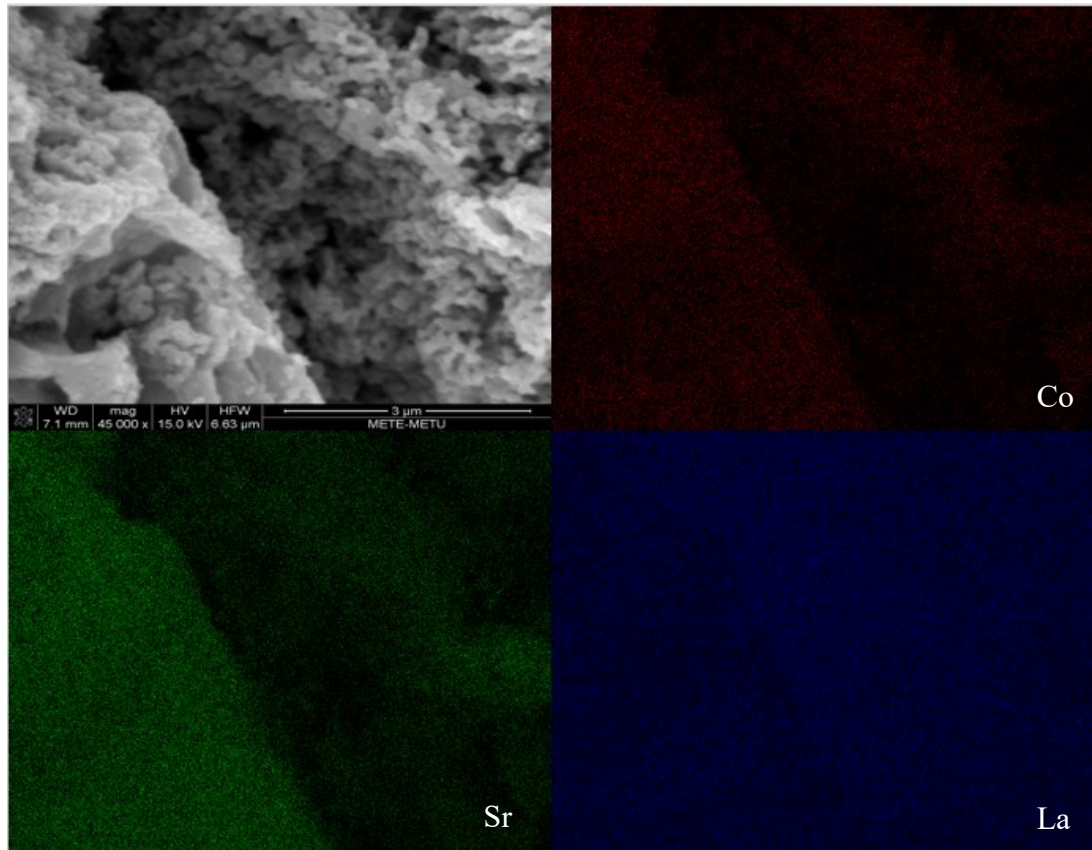


Figure 4-33 EDS mapping of physically mixed powder at 45000 magnification

It was expected that dual phase powders were mixed in the fine scale, interpenetrated to each other as opposed to the case of physically mixed powder. To check the scale of structure in the dual phase powder *quantitatively*, a special experiment was conducted. A dual phase sample was examined and EDS mapped at different magnifications, namely 400, 1000, 2000, 4000, 8000, 16000, 30000 and 45000³. Unlike the physical mixture where clear elemental contrast was obtained at x400 (see Figure 4-10), there was no such contrast in dual phase powder. The contrast observed in physical mixture can be followed at magnifications as high as x45000. This was

³ Aforementioned mappings results are not included not to unnecessarily increase the volume of the thesis

considered to be the limit of elemental resolution in the current study. Dual phase powder when examined at x45000, there was no elemental contrast in terms any atom type. This implies that the scale of structure in dual phase powder is less than that observable under x45000. This roughly corresponds to a structural size of less than ~ 6 μm . So, EDS mappings of dual phase powder imply a successful interpenetration between phases because there is no contrast in terms of any element in broad range of magnifications. Consequently, it is understood that interpenetrated nano-porous agglomerates of constituent phases that are lower than ~ 6 μm in size but higher than particle size shown in SEM images namely at most 200-300 nm (refer to Table 4-3 and Figure 4-5) were attained.

Fine scale of structure implies us successful hetero interface formation in principle. Nevertheless, if such a reduced scale of structure is the case as well as significantly successful continuous contacts between phases is the case, then cathodes made up of with these dual phase synthesis powders are supposed manifest this. In other words, these cells are supposed to yield significant enhancement in overall oxygen reduction rate manifested as reduced cell polarization resistance induced by $\text{LSC}_{113/214}$ not only with respect to single phases powders but also with respect to physically mixed powder. However, aforementioned EIS responses show that beneficial effect of fine scale of structure did not reflect to cathode performance caused by $\text{LSC}_{113/214}$ hetero structures.

When disproof of the controversies surrounding the scale of structure findings in following pages in the light of site occupation are considered, excess porosity within powders which probably has led to poorly meeting constituent phases to air in fine scale is possible reason for modest electrochemical effect. Lack of triple phase boundaries is implied here. Moreover, there are thick and microstructurally heterogeneous cathodes through which many parameters can affect many things and it is hard to exactly identify what the case is as Baumann *et al.* [22] thoroughly states. Very high thickness (up to 100 μm) as well as porosity structure effects may have led to deficient EIS responses recorded. That is why, although dual phase synthesis did not yield huge agglomerates of two phases as opposed to physically mixing separately

synthesized powders and it gave fine scale of structure, affirmative reflection of it in overall performance was not monitored.

The second aspect is site occupations or La/Sr partitioning behavior constituting not only an interesting problem concerning one pot synthesis but also it is leading to controversies surrounding evaluation of EDS mapping results. For instance, one may assert as counter argument to “fine scale of structure” that there is still coarse scale of structure but almost *same* atomic fraction of *all* atoms in *both* phase inhibits any contrast. At this point it is very important to remind that even La difference between 0.14 and 0.16 could be recognized by mapping in physically mixed powder (see Figure 4-10). In order for mapping not to recognize any contrast, even such a very small difference should not be present within powder. But this is not realistic. In both phases, almost same atomic fractions possibility of all elements in phases is restricted not only by prospective lattice parameter mismatch but also this is forbidden by weight fraction calculations that Rietveld analyses revealed. One can also recommend tailoring experimental details namely accelerating voltage spot size etc. However, detecting difference even between 0.14 and 0.16 was possible in aforementioned conditions, making such tailoring senseless.

On the other hand, Sr (and/or La) site occupation differential could be considered as another source of incapability to detect contrast. However, this necessitates extremely heterogeneous distribution of La and Sr cations through *complete* matrix, which in turn necessitates very serious broadening of XRD patterns. Extent of broadening in this case would be so much that rather than broadening, release of new peaks pertaining to different angles would be the case. However, XRD patterns are not compatible with such high site occupation differential. Hence, although there is some sort of site occupation differential that is expected as stated before, its extent is not so much as to allow no contrast even at 45000 magnifications. Consequently, fine scale of structure cannot be opposed in the light of speculations based on site occupation uncertainties. It is also meaningful to note that EDS is not a suitable tool to detect atomic contrast at very low scale of structures. So, inability to clearly detect contrast can also be considered as an indicator of fine scale of structure.

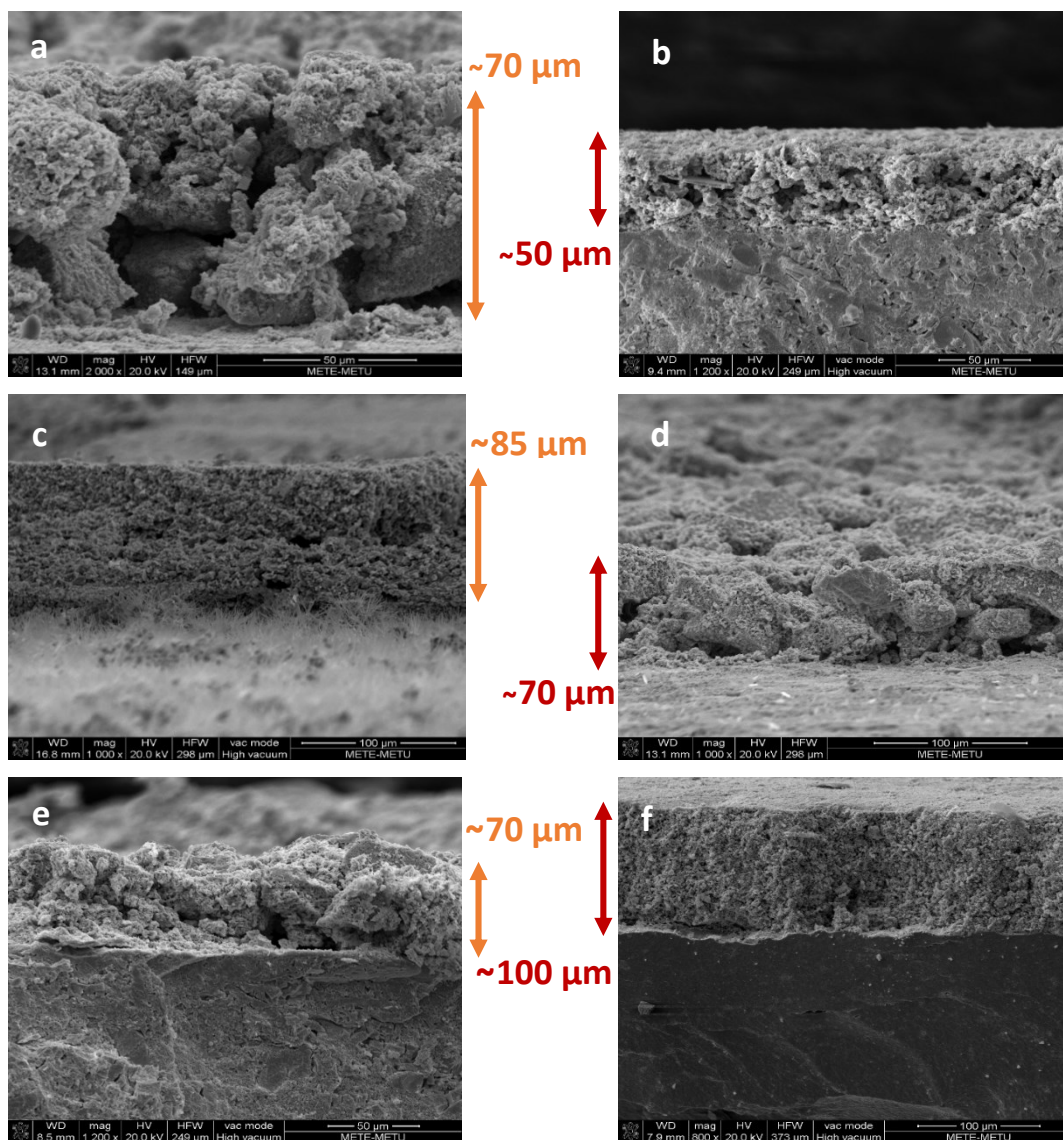


Figure 4-34 Cross sectional SEM images of symmetric cells showing cathode thicknesses (a) DP-1, (b) DP-3 (c) LSC₂₁₄ (d) LSC₁₁₃ (e) PM and (f) DP-5

Finally, cathode thickness effects to EIS responses should be taken into consideration. Many comments and evaluations has been done regarding all symmetric cells but credibility of these can be attained only if they are correlated with cathode thicknesses since any deviation in thickness can manifest itself as a deviation in overall cell resistance. Low thickness means low resistance in principle. Thicknesses of all cathodes have been observed in almost same thicknesses, clearing away any uncertainty of evaluations on ASR. Figure 4-34 gives cross sectional SEM images of

all cathodes. Only significant differential is observed in DP-3 and DP-5 cathodes with around 50 and 100 μm thicknesses respectively. Both deviate from the average expected values of 80 μm and DP-5 with higher thickness is expected to yield lower ASR. But in spite of higher thickness, it yielded the lowest ASR among all fortunately. Likewise, DP-3 with the lowest average cathode thickness exhibited high ASR. If for example DP-5 were to have the lower thickness, it would yield more reduced ASR. Consequently, one can not attribute performance differentials among signals pertaining to different dual phase powders to different cathode thicknesses; effect of thickness is eliminated in the light of Figure 4-34.

Fitting EIS responses to a reasonable equivalent circuit models is a fundamental task in researches based on impedance analysis. However, this is viable and significant only for the well-defined systems, which is not the case in this part of study. 70 μm thickness along with huge surface roughness and heterogeneously distributed porosities with varied sizes would makes such an attempt pointless, as comprehensively explained in previous sections.

Additionally, all of the cathodes have apparently have huge surface roughness. This situation in fact makes calculated area of air exposed surface indefinite for properly characterizing ASR. But this is valid for all cells and it should be kept in mind that the main concern is *comparison* of EIS responses of cells rather than determination of definite ASR for a certain cathode. Determination of suitable ASR for SOFC cathode is the task assigned to thin film cathode part in next chapter.

On the other hand, while any study that is keen on LSC cathodes must conduct a supplementary stability examination since chemical instability is of great concern for LSC cathodes, in thick film part of this study, such an attempt is pointless since current cathodes already seriously suffer from very high resistance due to thicknesses without any worthwhile hetero interfacial enhancement and poor interface maximization. Rather, chemical stability examination is also assigned to thin film cathode part in this study.

4.3. Conclusions

As the first time, synthesizing LSC_{113/214} dual phase system from one unique solution via Pechini method has been successfully achieved without any undesired third phase. It has been deduced from refinements and syntheses that formation of LSC₁₁₃ has dominated the formation of LSC₂₁₄ phase. EDS mappings demonstrated that dual phase synthesis did not produce huge agglomerates of phases. The scale of structure that is attained by one pot synthesis of LSC_{113/214} dual phase structure was between ~6 μm to ~200-300 nm. However, although finely dispersion of phases has been achieved, the positive effect of this in terms of hetero interface maximization has not been reflected to in situ electrochemical performances; the degree of cathode performance enhancement was modest. This might be attributed to the excess porosity resulting in low density of triple phase boundaries of LSC₁₁₃-air-LSC₂₁₄. Furthermore, beneficial effect of dual phase powders over physical blending was limited to the temperature interval of 550-650 °C. This does not mean that the use of dual phase synthesis is limited to this temperature interval, since this might change depending upon the cathode thickness and the porosity structure. Alteration of cathode thickness as well as microstructural features are susceptible to revise aforementioned useable limit. Although dual phase synthesis is incapable of making conventional thick cathode surface ORR limited, it can obviously be concluded to be a stimulating approach.

CHAPTER 5

FABRICATION AND PERFORMANCE OF THIN FILM LSC CATHODES

5.1. Introduction

The main concern of this chapter is the success in reduction of operating temperature *regardless* from the cost and/or fabrication difficulties of SOFCs. Maximized LSC_{113/214} hetero interfaces along with utilization of them through thin film cathode surface and significant temperature reduction were aimed since thin film cathodes are *well-defined* as opposed to thick porous cathodes and low-resistance alternatives along with cost and/or fabrication difficulties. For this purpose, as the way of LSC_{113/214} maximization, co-sputtering (simultaneous) of (La_{0.8}Sr_{0.2})CoO_{3-δ} and LaSrCoO_{4±δ} onto (Ce_{0.9}Gd_{0.1})O_{2-x} electrolyte was adopted and thin film composite cathodes were produced.

5.2. Preparation of Oxide Sputtering Targets

(La_{0.8}Sr_{0.2})CoO_{3-δ} and (La_{0.5}Sr_{0.5})₂CoO_{4±δ} powders were synthesized via Pechini route, as details of which comprehensively explained in previous chapter, and as-synthesized single phase powders were separately pressed into 2-inches diameter oxide sputtering targets using deformable die [197]. (La_{0.8}Sr_{0.2})CoO_{3-δ} and (La_{0.5}Sr_{0.5})₂CoO_{4±δ} targets were sintered at 1100 °C for 10 hours and air exposed surfaces of final targets were used in order for sputtering. This is because the bottom surface is in contact with crucible and loses cations to crucible. Concurrently, GDC powders were pressed into 19-mm pellets, which would act as electrolyte finally. These GDC pellets were sintered at 1350 °C for 10 hours to obtain a dense oxygen ion conducting membrane.

5.3. Fabrication of LSC Cathodes via Magnetron Co-Sputtering

Two GDC pellets were positioned in selected positions in the vacuum chamber. Then, magnetron sputtering of composite cathode was carried out on surfaces of two GDC pellets under 10^{-7} torr base pressure. Ar was maintained at a flow rate of $10 \text{ cm}^3/\text{min}$. Sputtering time was 10 hours for simultaneous sputtering of LSC. The substrate temperature was kept to $400 \text{ }^\circ\text{C}$.

Power loading on $(\text{La}_{0.8}\text{Sr}_{0.2})\text{CoO}_{3-\delta}$ and $\text{LaSrCoO}_{4\pm\delta}$ were 30 Watt for each. These values were selected based on previous experiments [198] which yielded $\text{LSC}_{214-10\% \text{ LSC}_{113}}$ and $\text{LSC}_{214-25\% \text{ LSC}_{113}}$. These will be named as cell-10% LSC_{113} and cell-25% LSC_{113} , respectively.

5.3.1. Fabrication of Symmetric Cell with Thin Film Cathode

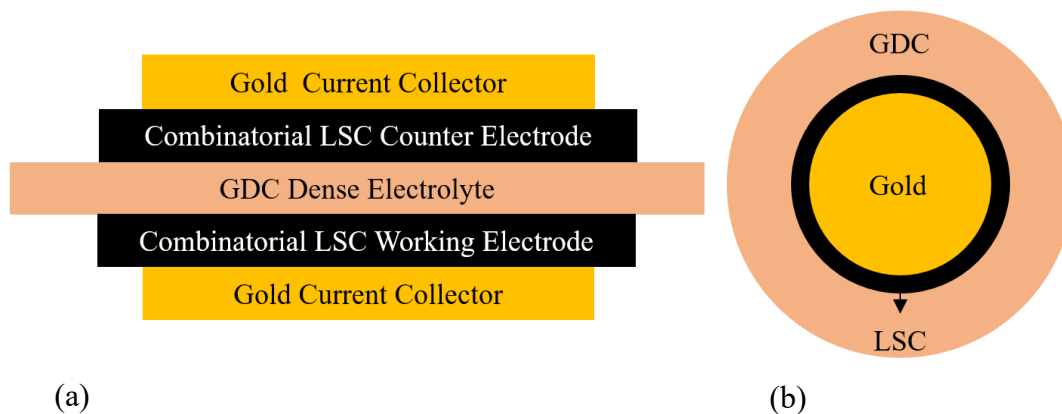


Figure 5-1 Schematic illustration of symmetric cells. (a) Cross section of cell and (b) Top/bottom view. Lateral size of air exposed surface (depicted by black) is seen in (b).

Details of final symmetric cells are illustrated schematically in Figure 5-1. Following cathode depositions to each side of GDC pellets over the circular mask having aperture size (diameter) of 12 mm, as current collector, gold was sputtered on surface cathode over a mask having 10 mm circular aperture size/diameter, which resulted in 1 mm lateral size of air exposed surface of cathode from which EIS responses were going to

be recorded. This 1 mm lateral aperture was used to calculate area of air exposed surface of cathode. Deposition time of Gold was 1 hour since Gold layer acted only as current collector and its deposition kinetic is higher because it is a metal. The same procedures were applied onto each side of GDC pellet and thereby two symmetric cells were attained for electrochemical analyses. The overall cell geometry is illustrated in Figure 5-1.

5.4. In situ Electrochemical Impedance Analysis

Final symmetric cells were analyzed by in situ electrochemical impedance spectroscopy (EIS) in the temperature range of 300-700 °C. Frequency range was 1 MHz-0.01 Hz with 10 mV perturbation amplitude. P_{O_2} was kept constant to ambient air. At 300-400 °C range, temperature increment was 20 °C, which turned out to be 50 °C between 400 °C and 700 °C. At each temperature, area specific resistances of composite cathodes were extracted on the basis of equation given below.

$$ASR = \frac{R_{measured} * Area}{2}$$

Thin film systems are well-defined systems, which reasonably enables attributing penetrated and/or separated impedance arcs to certain reaction steps, microstructural and/or chemical characteristics of cathode. This is done by fitting EIS data to certain equivalent circuit models. Hence, all spectra were fitted to equivalent circuit models, so long as this is literally recognized, possible, and physically reasonable.

In both cells, at the point at which 0.20 Ωcm^2 was attained, stability study was conducted since cell instability at increasing temperatures is the main concern regarding SOFCs [9,18]. ASR values were subsequently recorded per 2 hours and degradation regime of combinatorial symmetric cells were revealed and compared with literature. Finally post mortem SEM analysis were done on symmetric cells.

5.4.1. EIS Responses of Cell-10% LSC₁₁₃

Cell-10% LSC₁₁₃ is the one having excess LSC₂₁₄ with relatively modest content of LSC₁₁₃ due to its position near to LaSrCoO_{4+δ} target. Although EIS measurements were carried out subsequently at starting from 300 °C, evaluation of EIS responses begins with 700 °C since higher temperature responses are more evident in terms of equivalent circuit models and resultant ASR values.

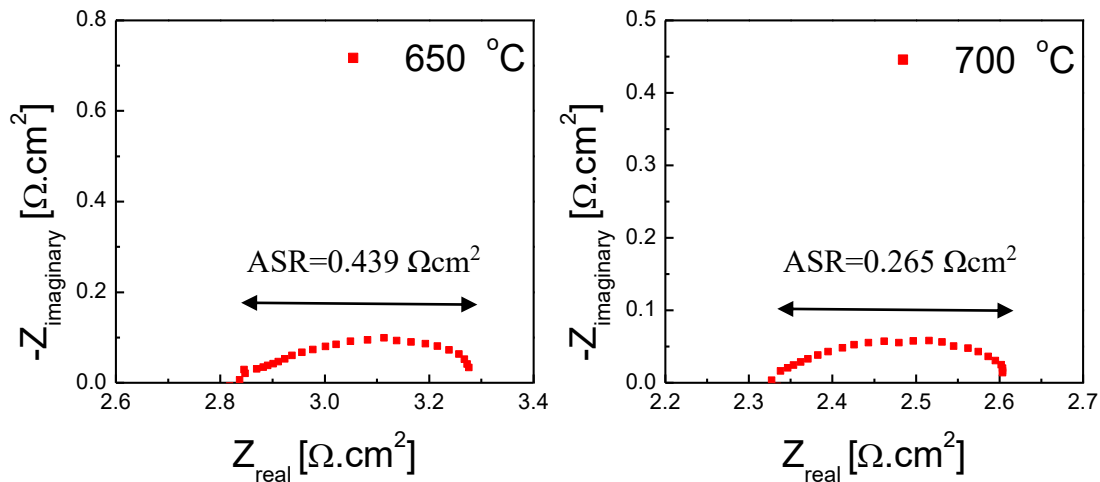


Figure 5-2 EIS Spectra of cell-10% LSC₁₁₃ at 650 and 700 °C

EIS spectra of cell-10% LSC₁₁₃ obtained at 700 and 650 °C are fitted to same equivalent circuit model depicted in Figure 5-2. In each case, there is one arc which is belonging to surface oxygen exchange step, which means that surface oxygen exchange step is the only rate limiting step at these temperatures. This is reasonable because at these temperatures, oxygen ionic diffusion is very fast and the length over which diffusion must take place is highly reduced, which excludes ionic transport process from being a source of resistance [173]. In the light of fitting EIS data to circuit models, ASR of cathodes have been found to be 0.439 and 0.265 Ωcm² at 650 and 700 °C, respectively. However, situation changes at 600 °C, in which an additional high frequency arc releases.

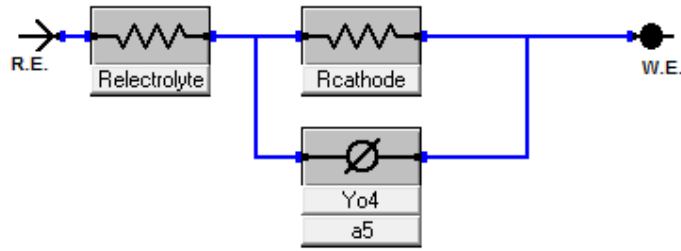


Figure 5-3 Equivalent circuit model #1 for cell-10% LSC₁₁₃ at 650 and 700 °C

At decreasing temperatures, an additional arc pertaining to oxygen ion exchange at electrode/electrolyte interface releases. In other words, oxygen ion exchange at this interface starts to be a source resistance anymore. Consequently, two arcs partially interpenetrating to each other in one spectrum is manifested. This behavior starts at 600 °C and was observed in 550 and 500 °C, too. This is illustrated in Figure 5-4 and Figure 5-6.

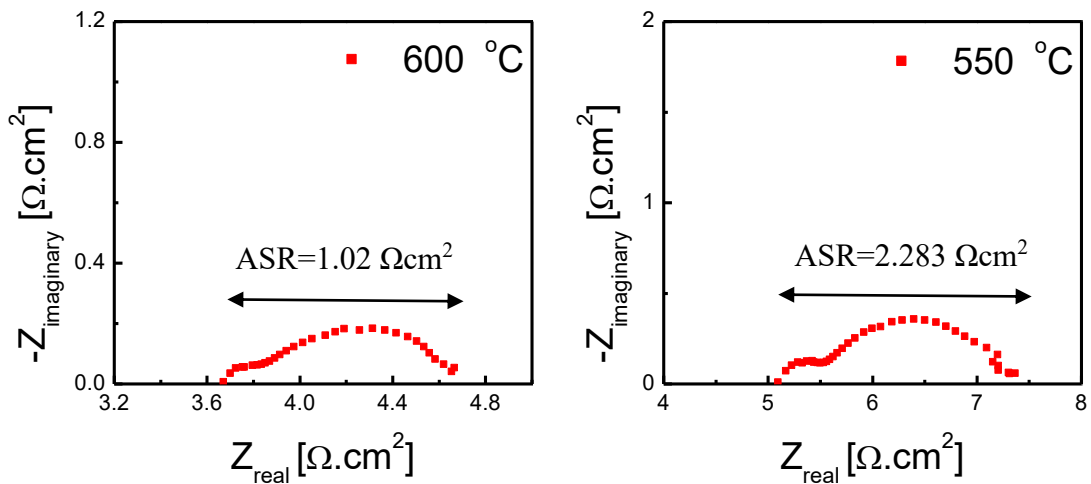


Figure 5-4 EIS Spectra of cell-10% LSC₁₁₃ at 600 and 550 °C

The well-known equivalent circuit model to MIEC cathodes at intermediate temperature range, manifested as interpenetrated two arcs, has been manifested by Baumann *et al.* [133]. This equivalent circuit model prevailing in a broad temperature range and fitting very well to 600, 550, 500, 450 and 400 °C EIS responses of cell-10% LSC₁₁₃ is illustrated in Figure 5-5. R_{CT} means charge transfer resistance

corresponding to the ion exchange resistance at electrode/electrolyte interface in case of SOFC. R_{lf} means low frequency resistance attributed to surface oxygen exchange step. \emptyset denotes constant phase element, mainly originated from non-ideality of the system as compared to ideal capacitive behavior.

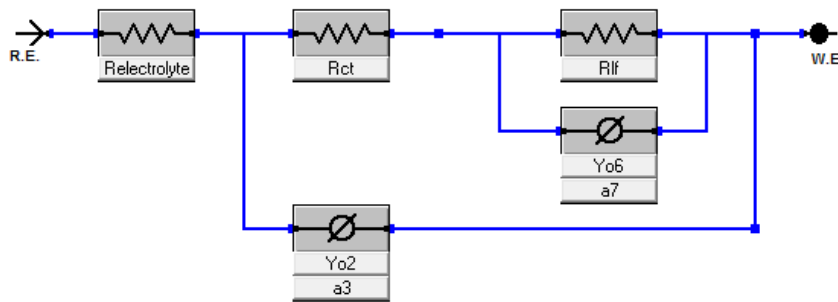


Figure 5-5 Equivalent circuit model #2 pertaining to 600, 550, 500 and 450 °C
[133,138]

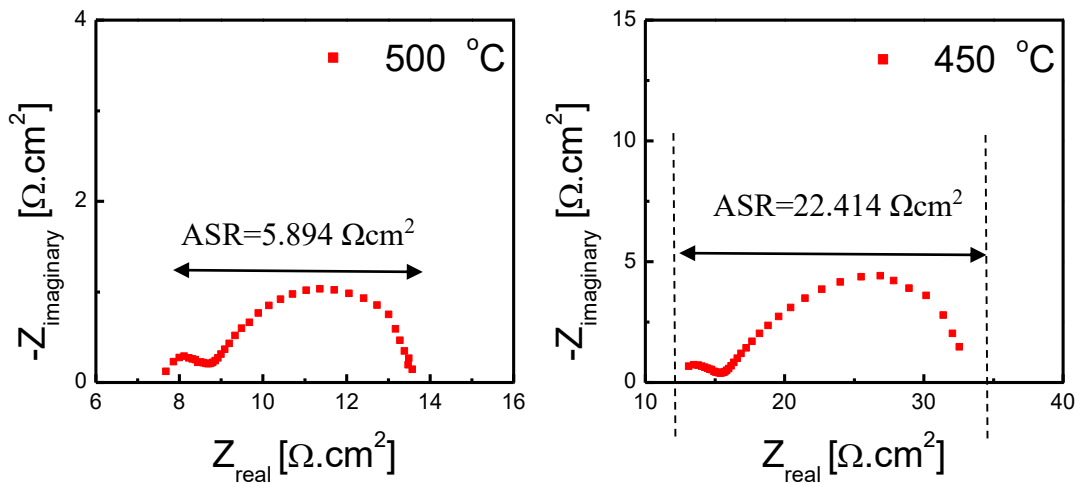


Figure 5-6 EIS Spectra of cell-10% LSC₁₁₃ at 500 and 450 °C

In general, underlying reason for fitting data to an equivalent model is to extraction of resistances pertaining to specified processes within electrode thanks to alternating current. However, in this study, overall ASR of cathodes are sought, which is possible only when incomplete arcs are finalized and the points at which data intersects with x-axis are revealed and/or partial interpenetration of arcs are solved by deconvolution

of these interpenetrated arcs. Therefore, the reason for fitting EIS data to model is mainly to finalize these arcs, one example of which is seen in cell response at 450 °C. By fitting this data, overall cathode ASR at 450 °C has been found to be 22.414 Ωcm^2 .

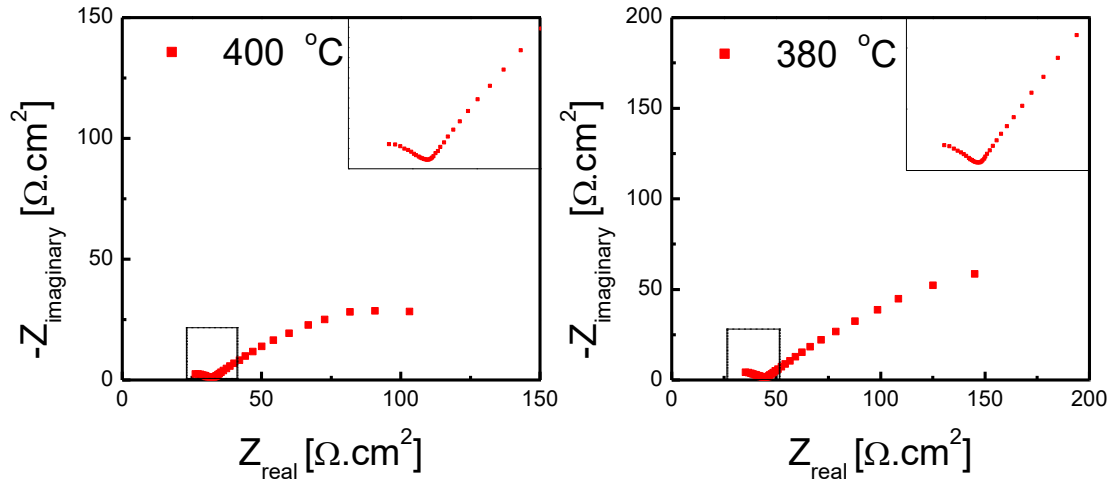


Figure 5-7 EIS Spectra of cell-10% LSC₁₁₃ at 400 and 380 °C

When temperature range below 400 °C is considered, Gerischer like behavior is more probable/expectable to prevail due to expected contribution of bulk ionic transport at decreasing temperatures [6]. Especially 400, 380 and 360 °C responses mimic Gerischer impedance. Nevertheless, circuit models involving Gerischer element exhibited weak goodness of fit during analyses. From 400 to 360 °C, equivalent circuit model #2 is thought to be the relevant model either because EIS responses are likely to finalize and intersect x-axis or it yielded relatively reasonable goodness of fit when used. Figure 5-8 shows EIS responses at 360 and 340 °C. ASR values, manifested in Table 5-1, have been calculated in the light of fit to model #2 in Figure 5-5.

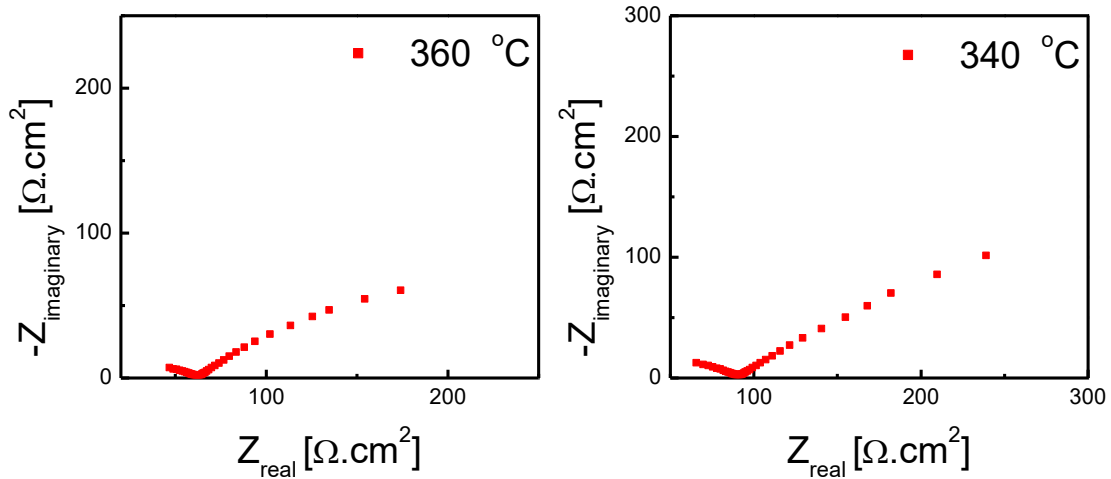


Figure 5-8 EIS Spectra of cell-10% LSC₁₁₃ at 360 and 340 °C

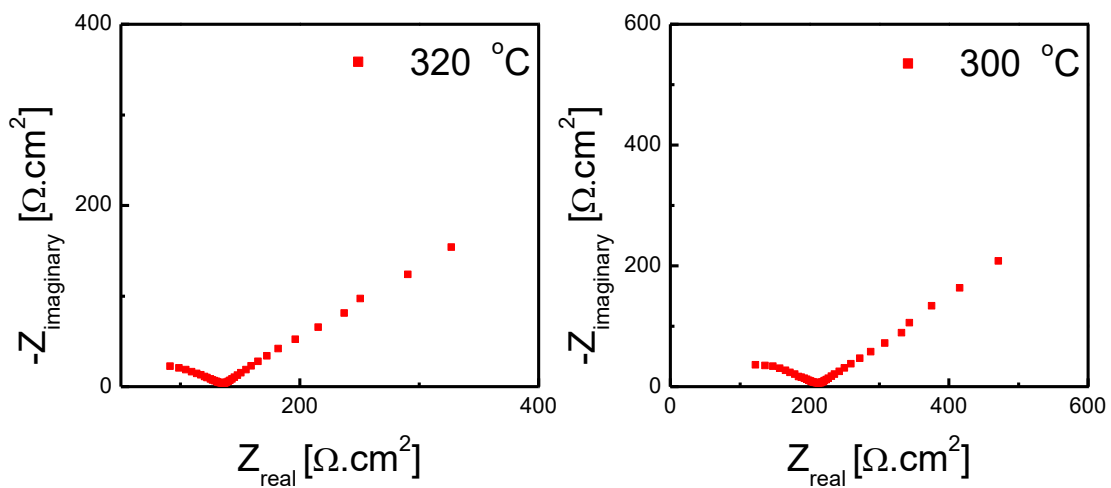


Figure 5-9 EIS Spectra of cell-10% LSC₁₁₃ at 320 and 300 °C

However, it is very hard to conclude with a confident circuit model for temperatures lower than 360 °C. From medium to low frequency range in 340, 320 and 300 °C spectra, EIS responses converge to linear like behavior. This is illustrated in Figure 5-8 and Figure 5-9. This linearization with decreasing frequency could be either due to Warburg element or it can typically be attributed to starting point of a semicircle. Which one is the valid is debatable. This debate enforces us to extrapolate ASR line in the ASR vs $\log(1/T)$ for the temperature in case of which fitting to equivalent circuit

model is unsatisfactory since practice of fitting and revealing the ASR is not realistic. This extrapolation was started from 400 °C. This is because even though the spectra at 380 and 400 °C was said to show nice goodness of fit, the ASR values that these fittings yield were not exactly assured and change in ASR would be able to deteriorate Arrhenius plot drastically.

Table 5-1 Calculated area specific resistances of cell-10% LSC₁₁₃ and its electrolyte in the light of equivalent circuit models

T (°C)	R_{cathode} (Ωcm²)	R_{electrolyte} (Ωcm²)
700	0.265	2.246
650	0.439	2.7646
600	1.02	3.629
550	2.283	5.011
500	5.894	7.629
450	22.414	13.13
400	-	26.35
380	-	35.34
360	-	46.76
340	-	65.63
320	-	91.35
300	-	122.28

Lack of almost error-free model fitting in this study indicates that symmetric cells obtained in this study are not perfectly well-defined as opposed to many thin film systems widely studied in literature [11,21,22,122,134,199]. Imperfections in fitting data to models in spite of dense thin micro electrode geometry in this study is thought to be mainly originated from surface roughness dictated by GDC electrolyte/substrate obtained via pressing its powders and sintering. Moreover, as opposed to widely investigated systems, lateral thickness of air exposed surface is 1 mm (see Figure 5-1 and Figure 5-10). Such a high lateral length, over which surface diffusion of oxygen atoms also takes place, more or less prevent achieving a homogeneous signal from the system.

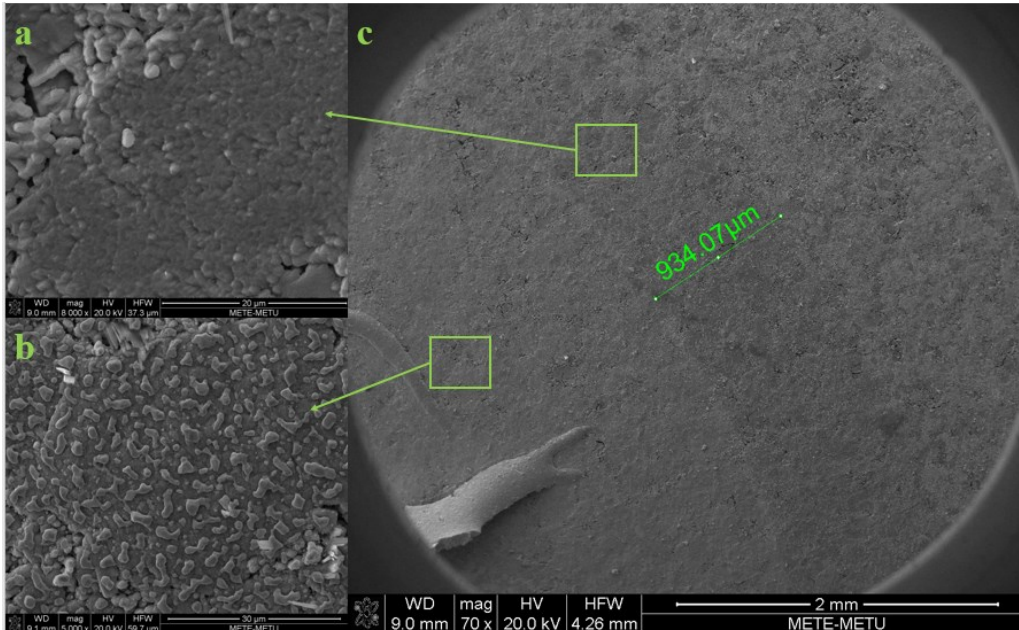


Figure 5-10 SEM image of cathode of cell-10% LSC₁₁₃. (a) dense microstructure of cathode free surface, (b) surface of Gold current collector and (c) lateral thickness of cathode free surface

5.4.2. EIS Responses of Cell-25% LSC₁₁₃

Cell-25% LSC₁₁₃ involves relatively more LSC₁₁₃ content than cell-10% LSC₁₁₃, which corresponds to formation of more catalytic hetero interfaces and leads to expectation of observing lower polarization resistance than cell-10% LSC₁₁₃. Truly, lower ASR values were detected in the case of cell-25% LSC₁₁₃ but only above 550 °C. Below this temperature, cathode of cell-10% LSC₁₁₃ yields lower polarization resistance. While the lowest ASR in cathode of cell-10% LSC₁₁₃ was 0.265 Ωcm², it was 0.14 Ωcm² in cathode of cell-25% LSC₁₁₃. Fortunately, the ASR pertaining to cathode of cell-25% LSC₁₁₃ is ideally lower than what is necessitated for fuel cell application [1]. However, the temperature at which these lowest ASR values have been observed, namely 700 °C, is very high in cell stability aspect. Because of 700 °C, cells are prone to be rapidly degraded.

700, 650, 600, 550, 500 and 450 °C cell responses match with equivalent circuit model illustrated in Figure 5-3. The only rate limiting step is surface oxygen exchange through these temperatures. High frequency arc which is associated with oxygen

exchange at electrolyte/electrode interface emerged at 400 °C in cathode of cell-25% LSC₁₁₃. This emerging temperature was 650 °C in cathode of cell-10% LSC₁₁₃ involving higher LSC₂₁₄ content. What can be the reason?

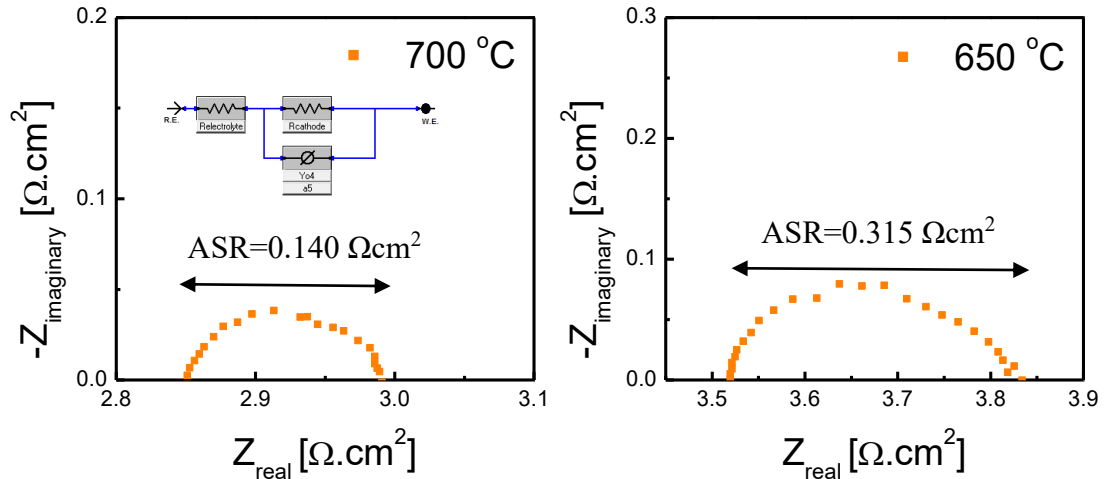


Figure 5-11 EIS Spectra of cell-25% LSC₁₁₃ at 700 and 650 °C

Transport of oxygen was mainly driven by interstitial diffusion of oxygen in LSC₂₁₄ as opposed to LSC₁₁₃ through which oxygen transport occurs via oxygen vacancies. On one hand, higher temperatures promote formation of oxygen vacancies but on the other hand, this promotion is relatively more in interstitial oxygen movement of LSC₂₁₄. Aside from more promotion of interstitials at higher temperatures, jumping of interstitial oxygen to electrolyte is supposed also be easier at also lower temperatures than substitutional moving of oxygen via vacancies of LSC₁₁₃. Furthermore, vacancy driven diffusion is anisotropic and direction dependent, making diffusivities generally larger [170]. When the huge volume of LSC₁₁₃ is considered, postponed release of high frequency arc is expected to be seen in cell-10% LSC₁₁₃, the one that is supposed to have higher LSC₂₁₄ content. However, reverse is valid. Oxygen jump to electrolyte is easier in cell-25% LSC₁₁₃ as manifested in EIS spectra in following pages. In such case, an insufficient interpenetration of cathode to electrolyte surface seems to be the most reasonable answer.

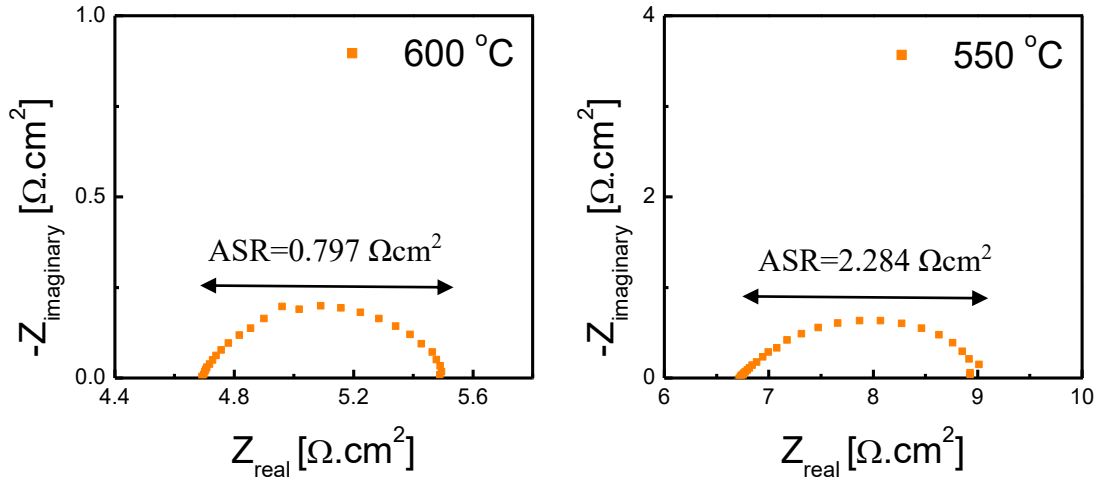


Figure 5-12 EIS Spectra of cell-25% LSC₁₁₃ at 600 and 550 °C

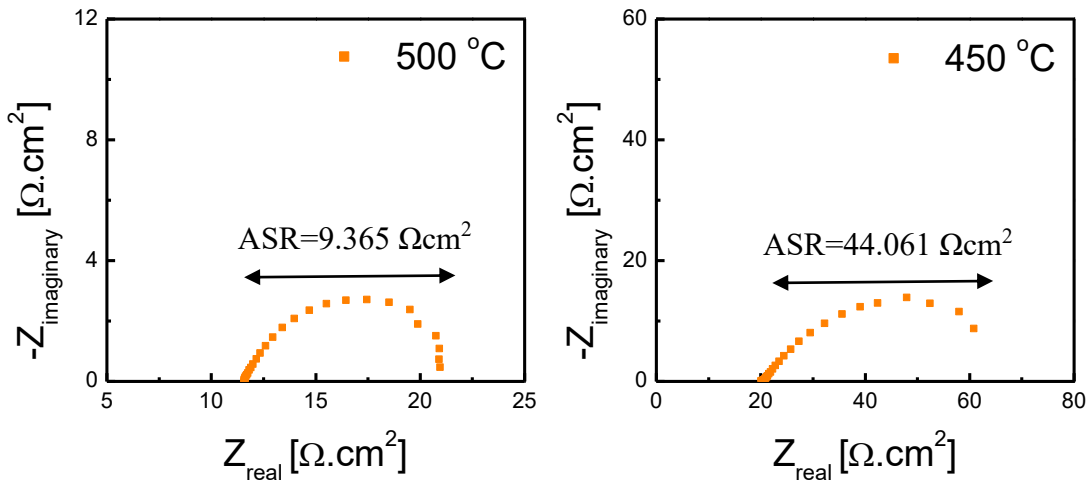


Figure 5-13 EIS Spectra of cell-25% LSC₁₁₃ at 500 and 450 °C

Another observation was based on goodness of fits of spectra to equivalent circuit models which are referred in literature. Until 450 °C, goodness of fits was highly satisfactory. The main reason for it was the availability of x-intercepts of arc. But it turned out to be insufficient after 400 °C, which makes resultant ASR uncertain and involving relatively high error. That's why resultant ASR values are not used below 400 °C in spite of the confidence on validity of equivalent circuit models. Table 5-2 gives the resistances of cell-25% LSC₁₁₃ that fitting yields well. Empty sites are the ones extrapolated.

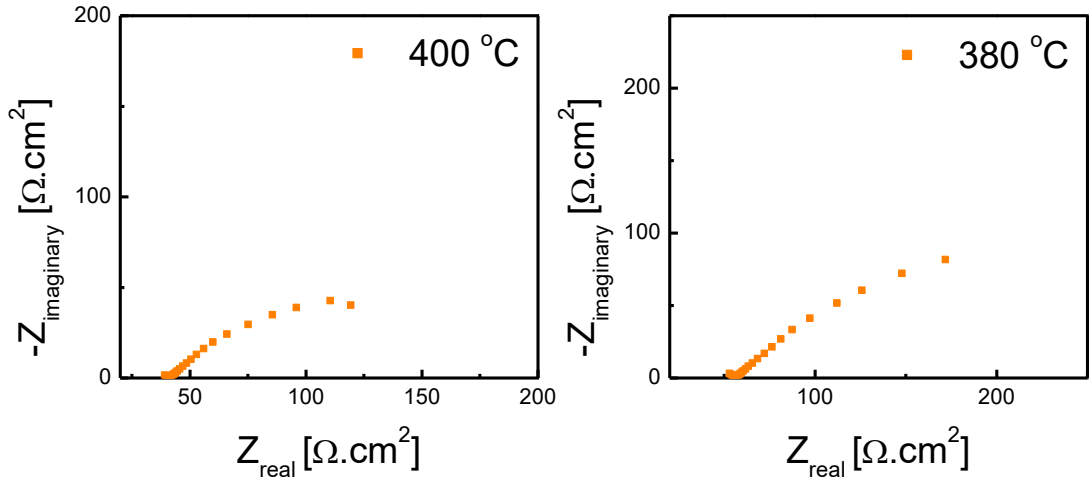


Figure 5-14 EIS Spectra of cell-25% LSC₁₁₃ at 400 and 380 °C

Table 5-2 Calculated area specific resistances of cell-25% LSC₁₁₃ and its electrolyte in the light of equivalent circuit models

T (°C)	R_{cathode} (Ωcm²)	R_{electrolyte} (Ωcm²)
700	0.140	2.85
650	0.315	3.52
600	0.797	4.69
550	2.284	6.73
500	9.365	11.59
450	44.061	20.06
400	-	39.12
380	-	53.01
360	-	74.16
340	-	107.84
320	-	141.51
300	-	203.89

Despite of the problems regarding fitting data to circuit model and evaluation of EIS spectra at low temperature regime (namely converging to 300 °C), there is an implicit strategy in struggling with this problem; concept of critical utilization length. By determining critical utilization length at specific temperature, what kind of process is

rate determining can be estimated, which allows correlation of EIS spectra with rate determining step. If cathode thickness is below critical utilization length (l_δ), then it can be stated that overall cathode resistance is limited by surface oxygen exchange step. If the reverse is valid, then bulk ionic transport is said to be rate limiting. l_δ of $(\text{La}_{0.8}\text{Sr}_{0.2})\text{CoO}_3$ at different temperatures are listed in Table 5-3.

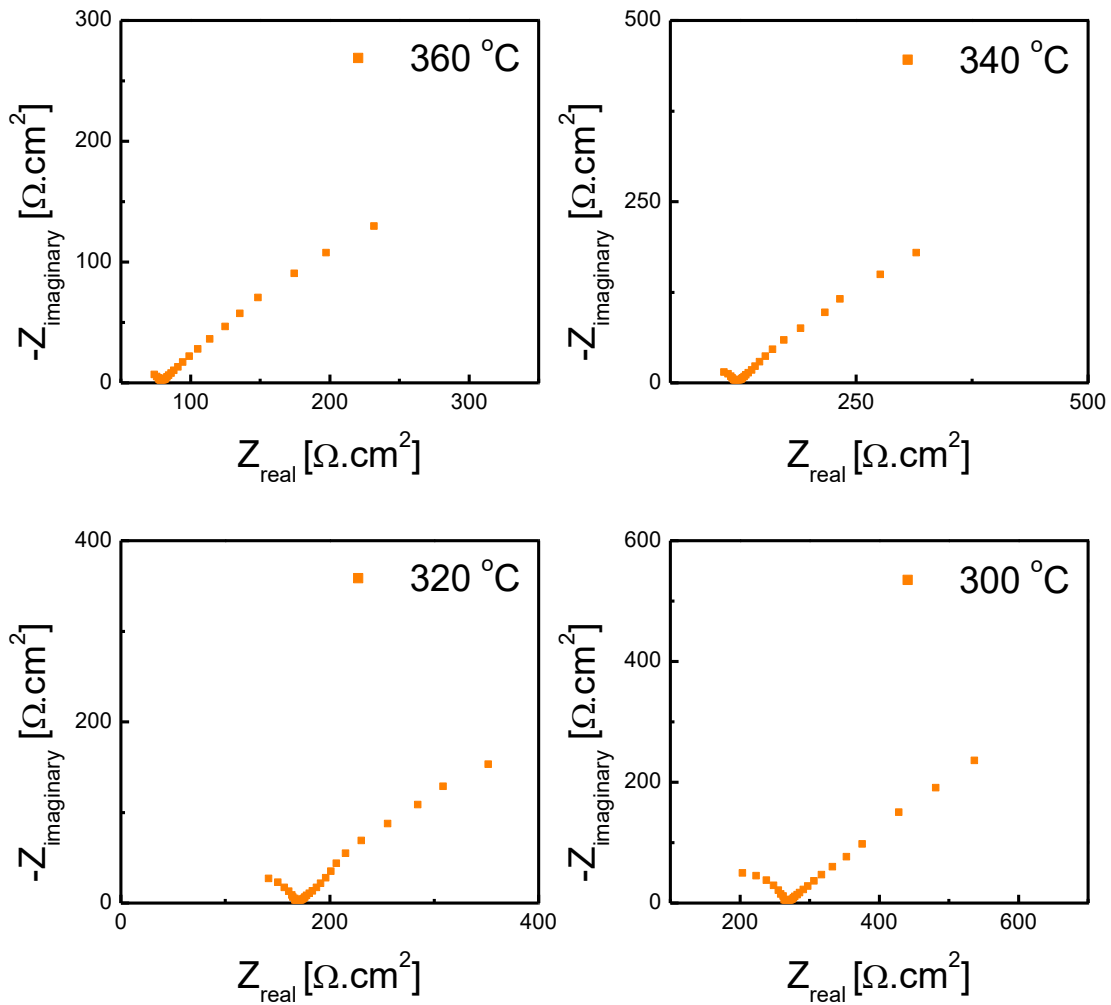


Figure 5-15 EIS spectra of cell-25% LSC₁₁₃ from 360 to 300 °C

Table 5-3 Critical utilization length (l_{δ}) of $(\text{La}_{0.8}\text{Sr}_{0.2})\text{CoO}_3$ at different temperatures [43]

T ($^{\circ}\text{C}$)	l_{δ}
700	$13 \pm 1.30 \mu\text{m}$
600	$3.47 \pm 0.35 \mu\text{m}$
500	$1.43 \pm 0.14 \mu\text{m}$
450	$630 \pm 63 \text{ nm}$
400	$400 \pm 40 \text{ nm}$

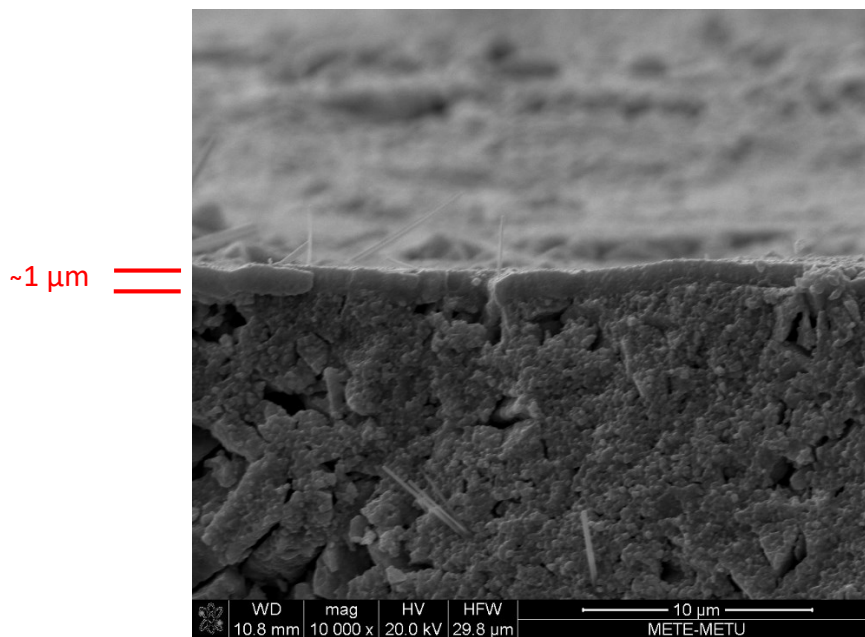


Figure 5-16 Cross section of cell-10% LSC_{113} manifesting the μm level thickness

If it is considered that aforementioned cathodes are around in $1 \mu\text{m}$ thickness, it is inferred that starting from 400°C , current thicknesses of cathodes lead the cathodes to be limited by bulk ionic transport rather not by surface oxygen exchange step after that point since cathode thickness is well higher than l_{δ} anymore. In addition to geometric considerations of cells explained before, critical utilization length concept explains why impedance responses exhibited unstableness after $400\text{-}450^{\circ}\text{C}$. In the light of l_{δ} values, it is not surprising to see Warburg behavior at 300°C and Gerischer like behavior at 450°C . These values also explain unfinished EIS arcs in Chapter 4.

5.4.3. Stability of Cathodes

Cathode stability is one of the biggest concern mainly because of surface Sr segregation in cobalt containing perovskites [19,87]. Therefore, how stable the co-sputtered cathodes are sought. Accordingly, the temperature at which aforementioned targeted ASR value ($0.2 \Omega\text{cm}^2$) was attained was determined.

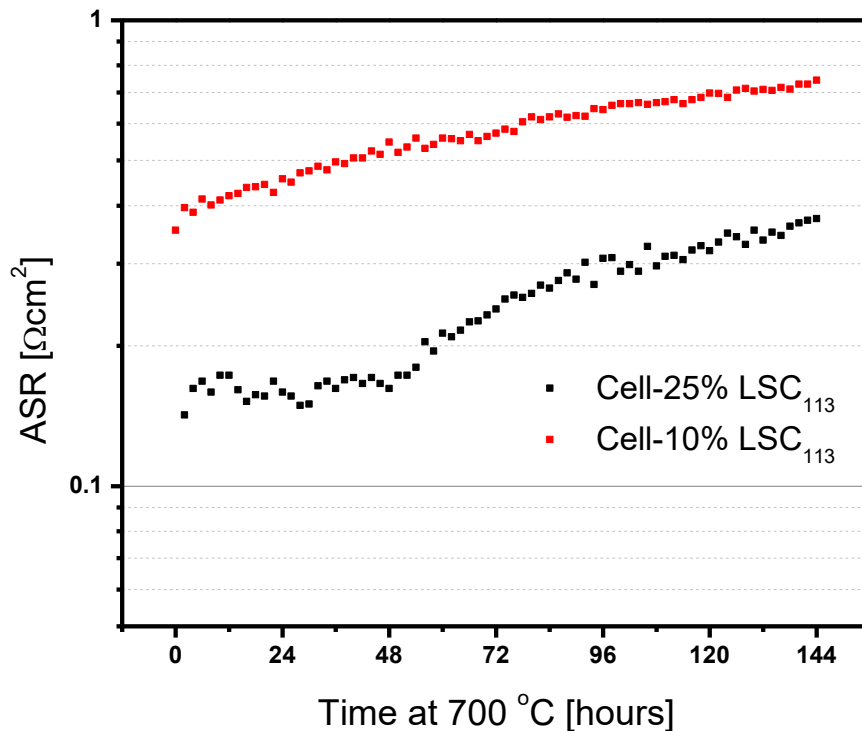


Figure 5-17 Cell resistances at 700 °C as function of time

Unfortunately, even at 700 °C, cell-10% LSC₁₁₃ yielded $0.265 \Omega\text{cm}^2$ and 700 °C is supposed to result in very robust performance degradation in the light of literature findings. Cai *et al.* [18] found that polarization resistance of cathode made up of with LSC₁₁₃ promotes to around $20 \Omega\text{cm}^2$ from $0.7 \Omega\text{cm}^2$ at 650 °C and within 72 hours. Similarly, Kubicek *et al.* [9] revealed an increase in cathode polarization resistance from $0.8 \Omega\text{cm}^2$ to $75 \Omega\text{cm}^2$ at again 650 °C and within 72 hours.

Cathodes of cell-10% LSC₁₁₃ and cell-25% LSC₁₁₃ were tested at 700 °C for 144 hours in the current system and these aforementioned rates are expected to be well higher in

case of them. In spite of higher temperature and testing time, however, cathodes of cell-25% LSC₁₁₃ and cell-10% LSC₁₁₃ exhibited resistance increase rates *much lower* than the literature findings stated above. Cell-10% LSC₁₁₃ started from 0.265 Ωcm² cathode polarization resistance and at the end of 144 hours, ASR was just 0.74 Ωcm², corresponding to 20 times lower degradation rate than what Cai *et al.* [18] discovered. In case of cathode of cell-25% LSC₁₁₃, aside from lower ASR than cathode of cell-10% LSC₁₁₃ at the same temperature, degradation rate of it is even lower as compared to cathode of cell-10% LSC₁₁₃. Its ASR raised to 0.30 Ωcm² from 0.14 Ωcm² in 144 hours, corresponding to 28 times lower rate than ref [18]. Therefore, co-sputtered cathodes in this study yielded outstanding stability in literature. This is a remarkable result. Nonetheless, both of the cathodes of cell-10% LSC₁₁₃ and cell-25% LSC₁₁₃ are still beyond the requirements for a successful commercialization not only because of limited lifetime but also their high operation temperature restricting interconnect material.

5.5. Comparative Evaluation of EIS responses

If the chemical processes occurring at SOFC cathode are namely oxygen reduction and cathode is activation limited rather than diffusion limited (non-thick film case), then overall cathode reaction should be triggered by temperature. This dictates Arrhenius behavior for aforementioned cathode when the thin dense film case is considered. Arrhenius equation, which is supposed to govern aforementioned cathodes, is given below.

$$k = A * \exp\left(-\frac{E_a}{k_B T}\right)$$

Where A is pre-exponential constant, k is reaction rate, E_a is activation energy, k_B is Boltzmann constant and T is temperature in Kelvin. It can be transformed to another form more apparently manifesting temperature dependence characteristics.

$$\ln k = \ln A - \frac{E_a}{k_B} \frac{1}{T}$$

Equation above means that reaction rate, which is in correlation with cell resistance, is a linear function of $1/T$ and E_a/k_B is slope of such a linear equation. Accordingly, logarithm of ASR values extracted from the EIS were drawn as function of $1/T$ and linearity was achieved as it is manifested in Figure 5-18, from which slopes are extracted.

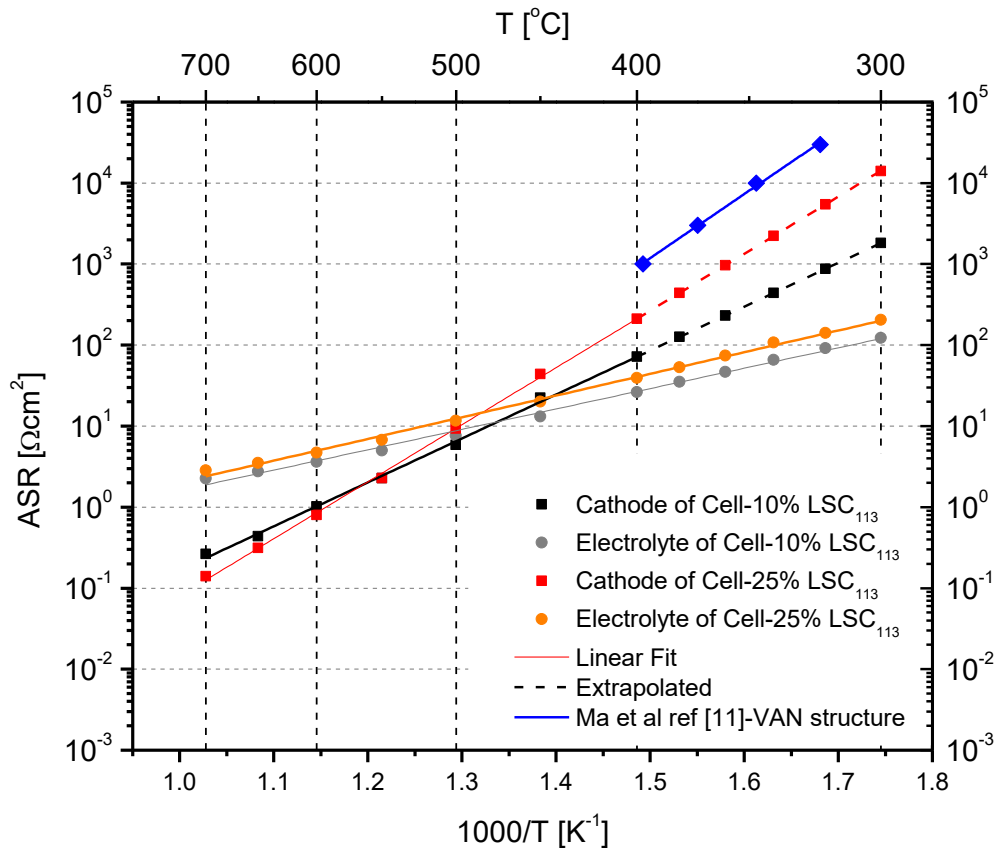


Figure 5-18 Temperature dependence of area specific resistance (ASR) pertaining to electrolytes and differential cathodes

Variation of ASR values pertaining to both cathodes and electrolytes with respect to inverse temperature yielded perfect linear behavior. However, below 400 °C, lines are extrapolated due to aforementioned imperfections and/or uncertainties in EIS data fitting to circuit models at lower temperatures. Extrapolation was done only for cathodes because electrolytes had no problem of goodness of fit. These extrapolated parts are identified by dashed lines in Figure 5-18. In terms of representativeness,

extrapolation was done in such a way that slope at 700-400 °C range was preserved in scale of 10^{-4} . Thanks to extremely slight contribution of high frequency arc, associated with the resistance caused by oxygen jump from cathode to electrolyte, the slope pertaining to overall ASR is also the slope of the real contribution of low frequency arc, which is attributed to surface oxygen exchange process at the air exposed surface. Thus, ASR records which are monitored in Figure 5-18 can also be read as ‘resistance of surface oxygen exchange process’. Numeric values of these slopes and corresponding activation energies were represented in Table 5-4.

Ma *et al.* [11] first time adopted combinatorial sputtering by pulse laser deposition (PLD) and attained vertically aligned nano-structures (VAN), yielding $10^3 \Omega\text{cm}^2$ at 400 °C and ambient oxygen. Differently from this unique study in literature, magnetron sputtering was used first time as the way of combinatorial sputtering in this study. Hence, even though there are many studies utilizing LSC cathodes as well as LSC_{113/214}, VAN structure is the major comparison reference due to simultaneous sputtering.

Table 5-4 Modified Arrhenius equations derived from data, corresponding slopes, activation energies and goodness of fit depicted as R^2

Component	Equation ($y=aX+b$)	Slope	R^2	E_a (eV)
Cathode of Cell-25% LSC ₁₁₃	$y=7.036X-8.129$	7.036	0.9997	1.22±0.02
Cathode of Cell-10% LSC ₁₁₃	$y=5.42X-6.199$	5.420	0.9995	0.94±0.02
Electrolyte of cell-25% LSC ₁₁₃	$y=2.515X-2.309$	2.515	0.9960	0.44±0.01
Electrolyte of cell-10% LSC ₁₁₃	$y=2.678X-2.372$	2.678	0.9980	0.46±0.01

Accordingly, it can be stated that activation energies given in Table 5-4 are ultimate comparison parameter. Cathodes derived in this study exhibited relatively lower activation energies with respect to VAN structure for surface oxygen exchange process. VAN structure yields 1.35 eV activation energy while cathodes of cell-25% LSC₁₁₃ and cell-10% LSC₁₁₃ above produced 1.22 and 0.94 eV, respectively. This means that cathodes derived in this study are less sensitive to temperature increments than what literature concluded. In the light of this finding, at 400 °C, cathodes of cell-

25% LSC₁₁₃ and cell-10% LSC₁₁₃ seem to show lower ASR than VAN at first glance. But due to higher sensitivity to T changes, VAN is candidate to turn out to be a lower resistance alternative at increasing temperatures. 400 °C responses of cell-25% LSC₁₁₃ and cell-10% LSC₁₁₃ are respectively 211.4 and 71.6 Ωcm², which are well lower than 10³ Ωcm² of VAN.

Furthermore, Ma *et al.* [11] detected one-fold enhancement caused by hetero interfaces as depicted by the blue line in Figure 5-18. As can be seen from figure, cathodes derived by magnetron sputtering in this study showed one more fold advancement in surface oxygen exchange ASR than VAN structure. Accordingly, it can also be stated that magnetron co-sputtering provided better catalytic effect at lower temperature regime than VAN structure obtained by PLD. But 3-4 orders of magnitude enhancement [15,21] have not been achieved in this study. At most 1.5 or 2-fold enhancement has been attained in surface oxygen exchange. It can be definitely stated that this is not an astonishing results and not caused by any direction dependent property of cathodes due to absence of any epitaxy within the cathodes herein. In order to explain the possible reasons, mechanism behind this enhancement as well as microstructural features of cathodes, i.e. geometry of cell, must be revealed.

One may claim at this point that VAN structure is ideal and almost defect free in terms of cathode geometry, namely surface roughness and/or lateral length of cathode free surface as well as epitaxy. This makes VAN suitable for low temperature regime evaluation as opposed to cathodes of cell-10% LSC₁₁₃ and cell-25% LSC₁₁₃ where for example significant surface roughness prevails. This is true but, effect of this surface roughness differential is too modest to explain more than 1-fold additional reduction in ASR. Thus, it can be apparently stated that magnetron co-sputtering has led to significant reduction in ASR more than PLD. Nevertheless, what kind of microscopic history has led to this is debatable. For instance, whether targeted hetero interfaces were formed or not is not known. If they are formed, how densified they are or if they are vertically aligned are debatable. Maybe both of the targeted phases were not formed but the reason for enhancement was non-crystalline structure of films at least by part. SEM images given in Figure 5-10 and Figure 5-16 manifest imperfections in cathode geometry implying that SEM analysis is inadequate for clarification of these.

Without FIB-TEM study, it is impossible to make statement on interface direction, alignment and/or geometry. Nonetheless, it is anticipated that there is no uniform hetero-interface distribution, alignment through cathode surface and/or bulk. Polycrystalline substrate and high surface roughness's strengthen such anticipation. But still what can be the reason for unexpected reduction in ASR can be discussed.

First, when discussions on mechanisms behind $\text{LSC}_{113/214}$ induced ORR are considered, oxygen deficiencies and excessiveness in LSC_{113} and LSC_{214} must be respectively referred. One possibility is the formation of Sr site occupations in either LSC_{113} and LSC_{214} different from well-studied compositions and resulting degree of ORR enhancement that has created higher enhancement in ORR reflected by lower ASR in this study. However, its capability to yield 1-1.5 orders of magnitude additional ASR reduction is still debatable. Second, extreme dissimilar interface densification may have been employed here. But this is also not a probable reason on the basis of SEM images of cathode. Even if this is so, it is important to note the degree of interface densification in VAN structure that Ma *et al.* derived [11], which is the form of 200-300 nm phase domains through 200-nm thick epitaxial films. The aforementioned cathodes of this study are unlikely to surpass such a high densification degree if complexity and non-ideality of the current cathodes are taken into consideration. Consequently, at least partial non-crystallinity through the cathodes of this study is considered to be the most probable reason for surpassing ASR reduction than the unique combinatorial sputtering study of literature [11]. High stability of the current cathodes as reflected previously also supports this assertion.

Aside from comparisons/debates based on co-sputtering, abovementioned cathodes have not opened a new scope regarding not only hetero interface but also temperature regardless cathode performance. The lowest ASR reported to date, which is $0.023 \text{ } \Omega\text{cm}^2$ at $600 \text{ } ^\circ\text{C}$, has been obtained from thin film electrode utilizing $\text{LSC}_{113/214}$ [119]. What has been found in this study was at most $0.797 \text{ } \Omega\text{cm}^2$, which is behind such results.

5.6. Conclusions

LSC₁₁₃/LSC₂₁₄ composite cathodes were obtained for first time via magnetron co-sputtering of LaSrCoO₄ and (La_{0.8}Sr_{0.2})CoO₃ phases. Performances of eventual dense thin film cathodes were evaluated on the basis of cell polarization resistances with the aid of EIS. First of all, target of 400 °C SOFC operation temperature could not be achieved; polarization resistances dictated by energy conversion efficiency could be acquired hardly at 700 °C. Nonetheless, studied phase fractions within cathodes yielded around 1.5-fold enhancement as well as lower activation energy of surface oxygen exchange induced by hetero-structure. This constitutes the best degree of enhancement in literature achieved from co-sputtered LSC₁₁₃/LSC₂₁₄ systems, the only study of which was based on PLD and yielded 1-fold enhancement [11]. As second, accordingly, such enhancement makes this study the best in reducing ASR of co-sputtered cells. Possible reason for such consequence in spite of relatively not as well-defined current structure than Ma *et al.* [11] can be the possible non-crystallinity within cathodes in this study. Finally, magnetron co-sputtering of LSC₁₁₃/LSC₂₁₄ yielded the best cell stability as compared to those reported in the literature [9,18].

CHAPTER 6

CONCLUSIONS

In this study, two approaches were adopted to utilize $\text{LSC}_{113/214}$ hetero structures for enhancing SOFC cathode performance. In first approach, maximization of $\text{LSC}_{113/214}$ hetero interface was aimed by thick porous conventional cathode, which is rather unusual in the literature. One pot synthesis of $\text{LSC}_{113/214}$ dual phase structure was implemented in pursuit of this target. In second approach, $\text{LSC}_{113/214}$ hetero structures were constructed by magnetron co-sputtering through which two phases were simultaneously sputtered in order to maximize hetero interface in dense thin film cathode.

In first approach, LSC_{113} and LSC_{214} powders were separately synthesized successfully. This was followed by physically blending them in order to maximize the hetero interfaces. However, the scale of structure in this method was found to be ~ 100 μm by SEM-EDS analysis, which resulted in poor cathode performance as measured by in situ EIS. One pot synthesis of $\text{LSC}_{113/214}$ dual phase composite was carried out by Pechini method. Synthesis of $\text{LSC}_{113/214}$ dual phase cathode from one unique solution via Pechini route has been successfully achieved for the first time in literature without any undesired third phase. It has been inferred from XRD refinements that the formation of LSC_{113} is favored more than the formation of LSC_{214} phase. EDS mappings of resultant powders showed that dual phase synthesis leads to a more refined microstructure. The scale of structure that is attained by one pot synthesis of $\text{LSC}_{113/214}$ dual phase structure was found to be between ~ 6 μm to ~ 200 - 300 nm. However, although finely dispersion of phases has been achieved, the positive effect of it in terms of hetero interface maximization has not been reflected to EIS measurements; degree of cathode performance enhancement was relatively modest.

This might be attributed to the excess porosity resulting in low density of triple phase boundaries of LSC_{113} -air- LSC_{214} . Furthermore, beneficial effect of dual phase powders over physical blending was limited to the temperature interval of 550-650 °C. This does not mean that the use of dual phase synthesis is limited to this temperature interval, since this might change depending upon the cathode thickness and the porosity structure. Alteration of cathode thickness as well as microstructural features are susceptible to revise aforementioned useable limit. Although dual phase synthesis is incapable of making conventional thick cathode surface ORR limited, it can obviously be concluded to be a stimulating approach.

The main problem in analysis of dual phase composite structure was the highly debatable partitioning of cations La and Sr between the constituent phases. Rietveld analysis based on $\text{CuK}\alpha$ radiation on XRD was insensitive to site occupation refinement. Exact and sensitive determination of final site occupations could be solved by neutron diffraction and corresponding Rietveld refinement.

Moreover, EIS responses are strong functions of cathode thickness in especially porous conventional cathodes. Hence, any thinner cathodes derived by screen printing or tape casting namely with the same dual phase powders are expected to yield different comparative EIS responses than what was attained in this study. When goodness in scale of structure in dual phase syntheses is considered, thinner cathodes are expected to yield more favorable results. Finally, new solution based synthesis routes could be sought by sol-gel chemists for the commercial success of dual phase synthesis.

In the second approach, $\text{LSC}_{113}/\text{LSC}_{214}$ composite cathodes were obtained for first time via magnetron co-sputtering of LaSrCoO_4 and $(\text{La}_{0.8}\text{Sr}_{0.2})\text{CoO}_3$ phases. Performances of eventual dense thin film cathodes were evaluated on the basis of cell polarization resistances with the aid of EIS. First, target of 400 °C SOFC operation temperature could not be achieved; polarization resistances dictated by energy conversion efficiency could be acquired hardly at 700 °C. Nonetheless, studied phase fractions within cathodes yielded around 1.5-fold enhancement as well as lower activation energy of surface oxygen exchange induced by hetero-structure. This constitutes the best degree of enhancement in literature achieved from co-sputtered

LSC₁₁₃/LSC₂₁₄ systems, the only study of which was based on PLD and yielded 1-fold enhancement [11]. As second, accordingly, such enhancement makes this study the best in reducing ASR of co-sputtered cells. Possible reason for such consequence in spite of relatively not as well-defined current structure than Ma *et al.* [11] can be the possible non-crystallinity within cathodes in this study. Finally, magnetron co-sputtering of LSC₁₁₃/LSC₂₁₄ yielded the best cell stability as compared to those reported in the literature [9,18].

Non-crystallinity is proposed as the reason for ASR reduction and this can be understood by FIB-TEM analysis, a representative one of which is also essential in revealing hetero interface characteristics in the thin film. Thus, a comprehensive FIB-TEM investigation is advised regarding co-sputtering study. In addition, target of achieving 400 °C has not been achieved but only two compositions were analyzed in this study. Further variation in LSC_{113/214} systems obtained via magnetron co-sputtering are expected to yield lowering operation temperature than what is achieved in this study.

REFERENCES

- [1] B.C. Steele, A. Heinzl, Materials for fuel-cell technologies., *Nature*. 414 (2001) 345–352. doi:10.1038/35104620.
- [2] R.A. George, Status of tubular SOFC field unit demonstrations, *J. Power Sources*. 86 (2000) 134–139. doi:10.1016/S0378-7753(99)00413-9.
- [3] S.C. Singhal, Advances in solid oxide fuel cell technology, *Solid State Ionics*. 135 (2000) 305–313. doi:10.1016/S0167-2738(00)00452-5.
- Figure retrieved from
<http://citeseerx.ist.psu.edu/viewdoc/download?doi=10.1.1.325.2772&rep=rep1&type=pdf> (accessed on 23.06.2017)
- [4] N. Laosiripojana, W. Wiyaratn, W. Kiatkittipong, A. Arpornwichanop, A. Soottitantawat, S. Assabumrungrat, Reviews on solid oxide fuel cell technology, *Eng. J.* 13 (2009) 65–83. doi:10.4186/ej.2009.13.1.65.
- [5] A.J. Jacobson, Materials for solid oxide fuel cells, *Chem. Mater.* 22 (2010) 660–674. doi:10.1021/cm902640j.
- [6] S.B. Adler, Factors governing oxygen reduction in solid oxide fuel cell cathodes, *Chem. Rev.* 104 (2004) 4791–4843. doi:10.1021/cr020724o.
- [7] N. Mahato, A. Banerjee, A. Gupta, S. Omar, K. Balani, Progress in material selection for solid oxide fuel cell technology: A review, *Prog. Mater. Sci.* 72 (2015) 141–337. doi:10.1016/j.pmatsci.2015.01.001.
- [8] S.P. Jiang, Activation, microstructure and polarization of solid oxide fuel cell cathodes, *J. Solid State Electrochem.* 11 (2006) 93–102. doi:10.1007/s10008-005-0076-9.
- [9] M. Kubicek, A. Limbeck, T. Frömling, H. Hutter, J. Fleig, Relationship between Cation Segregation and the Electrochemical Oxygen Reduction Kinetics of $\text{La}_{0.6}\text{Sr}_{0.4}\text{CoO}_{3-\delta}$ Thin Film Electrodes, *J. Electrochem. Soc.* 158 (2011) B727. doi:10.1149/1.3581114.
- [10] E.D. Wachsman, K.T. Lee, Lowering the temperature of solid oxide fuel cells., *Science* (80-.). 334 (2011) 935–9. doi:10.1126/science.1204090.
- [11] W. Ma, J.J. Kim, N. Tsvetkov, T. Daio, Y. Kuru, Z. Cai, Y. Chen, K. Sasaki, H.L. Tuller, B. Yildiz, Vertically aligned nanocomposite $\text{La}_{0.8}\text{Sr}_{0.2}\text{CoO}_{3-\delta}/(\text{La}_{0.5}\text{Sr}_{0.5})_2\text{CoO}_{4+\delta}$ cathodes – electronic structure, surface chemistry and oxygen reduction kinetics, *J. Mater. Chem. A*. 3 (2015) 207–219. doi:10.1039/C4TA04993D.
- [12] K.T. Lee, A. Manthiram, Comparison of $\text{Ln}_{0.6}\text{Sr}_{0.4}\text{CoO}_{3-\delta}$ (Ln=La, Pr, Nd, Sm, and Gd) as Cathode Materials for Intermediate Temperature Solid Oxide

- Fuel Cells, *J. Electrochem. Soc.* 153 (2006) A794–A798.
doi:10.1149/1.2172572.
- [13] C. Sun, R. Hui, J. Roller, Cathode materials for solid oxide fuel cells: A review, *J. Solid State Electrochem.* 14 (2010) 1125–1144.
doi:10.1007/s10008-009-0932-0.
- [14] J.A. Kilner, M. Burriel, Materials for Intermediate-Temperature Solid-Oxide Fuel Cells, *Annu. Rev. Mater. Res.* 44 (2014) 365–393. doi:10.1146/annurev-matsci-070813-113426.
- [15] M. Sase, K. Yashiro, K. Sato, J. Mizusaki, T. Kawada, N. Sakai, K. Yamaji, T. Horita, H. Yokokawa, Enhancement of oxygen exchange at the hetero interface of (La,Sr)CoO₃/(La,Sr)₂CoO₄ in composite ceramics, *Solid State Ionics.* 178 (2008) 1843–1852. doi:10.1016/j.ssi.2007.11.039.
- [16] B. Wei, Z. Lü, X. Huang, J. Miao, X. Sha, X. Xin, W. Su, Crystal structure, thermal expansion and electrical conductivity of perovskite oxides Ba_xSr_{1-x}Co_{0.8}Fe_{0.2}O_{3-δ} (0.3 ≤ x ≤ 0.7), *J. Eur. Ceram. Soc.* 26 (2006) 2827–2832.
doi:10.1016/j.jeurceramsoc.2005.06.047.
- [17] A.B. Stambouli, E. Traversa, Solid oxide fuel cells (SOFCs): A review of an environmentally clean and efficient source of energy, *Renew. Sustain. Energy Rev.* 6 (2002) 433–455. doi:10.1016/S1364-0321(02)00014-X.
- [18] Z. Cai, M. Kubicek, J. Fleig, B. Yildiz, Chemical Heterogeneities on La_{0.6}Sr_{0.4}CoO_{3-δ} Thin Films—Correlations to Cathode Surface Activity and Stability, *Chem. Mater.* 24 (2012) 1116–1127. doi:10.1021/cm203501u.
- Figure retrieved from
<http://pubs.acs.org/doi/abs/10.1021/cm203501u> (accessed on 23.06.2017)
- [19] N. Tsvetkov, Q. Lu, L. Sun, E.J. Crumlin, B. Yildiz, Improved chemical and electrochemical stability of perovskite oxides with less reducible cations at the surface, *Nat. Mater.* 15 (2016) 1010–1016. doi:10.1038/NMAT4659.
- [20] W.C. Chueh, S.M. Haile, Electrochemistry of mixed oxygen ion and electron conducting electrodes in solid electrolyte cells, *Annu Rev Chem Biomol Eng.* 3 (2012) 313–341. doi:10.1146/annurev-chembioeng-073009-101000.
- [21] E.J. Crumlin, E. Mutoro, S.J. Ahn, G.J. La O, D.N. Leonard, A. Borisevich, M.D. Biegalski, H.M. Christen, Y. Shao-Horn, Oxygen reduction kinetics enhancement on a heterostructured oxide surface for solid oxide fuel cells, *J. Phys. Chem. Lett.* 1 (2010) 3149–3155. doi:10.1021/jz101217d.
- [22] F.S. Baumann, J. Fleig, G. Cristiani, B. Stuhlhofer, H.-U. Habermeier, J. Maier, Quantitative Comparison of Mixed Conducting SOFC Cathode Materials by Means of Thin Film Model Electrodes, *J. Electrochem. Soc.* 154 (2007) B931. doi:10.1149/1.2752974.
- [23] M.P. Pechini, Method of preparing lead and alkaline earth titanates and niobates and coating method using the same to form a capacitor, US3330697 A, n.d.

- [24] M.J. Vinod, Efficiency Analysis of Planar Solid Oxide Fuel Cell, *ECS Trans.* 7 (2007) 1939–1943. doi:10.1149/1.2729306.
- [25] D.R. Gaskell, *Introduction to the Thermodynamics of Materials*, 5th ed., CRC Press, New York, 2008.
- [26] A. Bejan, *Advanced Engineering Thermodynamics*, John Wiley & Sons, 2016.
- [27] M.M. Kuklja, E.A. Kotomin, R. Merkle, Y.A. Mastrikov, J. Maier, Combined theoretical and experimental analysis of processes determining cathode performance in solid oxide fuel cells, *Phys. Chem. Chem. Phys.* 15 (2013) 5443–5471. doi:10.1039/c3cp44363a.
- [28] A. Evans, A. Bieberle-Hütter, L.J. Bonderer, S. Stucklenholz, L.J. Gauckler, Micro-solid oxide fuel cells using free-standing 3 mol.% yttria-stabilised-tetragonal-zirconia-polycrystal electrolyte foils, *J. Power Sources.* 196 (2011) 10069–10073. doi:10.1016/j.jpowsour.2011.07.087.
- [29] A. Chroneos, B. Yildiz, A. Tarancón, D. Parfitt, J.A. Kilner, Oxygen diffusion in solid oxide fuel cell cathode and electrolyte materials: mechanistic insights from atomistic simulations, *Energy Environ. Sci.* 4 (2011) 2774. doi:10.1039/c0ee00717j.
- [30] E.J. Crumlin, *Fundamental Studies of Heterostructured Oxide Thin Film Electrocatalysts for Oxygen Reduction at High Temperatures*, 2012.
Figure retrieved from
<https://dspace.mit.edu/handle/1721.1/74904#files-area> (accessed on 23.06.2017)
- [31] X. Wang, P.D. Thesis, *Dual-ion Conducting Nanocomposite for Low Temperature Solid Oxide Fuel Cells*, 2012.
- [32] B.C.H. Steele, Survey of materials selection for ceramic fuel cells: II. Cathodes and anodes, *Solid State Ionics.* 86–88 (1996) 1223–1234. doi:10.1016/0167-2738(96)00291-3.
- [33] K. Nikooyeh, R. Clemmer, V. Alzate-Restrepo, J.M. Hill, Effect of hydrogen on carbon formation on Ni/YSZ composites exposed to methane, *Appl. Catal. A Gen.* 347 (2008) 106–111. doi:10.1016/j.apcata.2008.06.005.
- [34] J.F.B. Rasmussen, A. Hagen, The effect of H₂S on the performance of Ni-YSZ anodes in solid oxide fuel cells, *J. Power Sources.* 191 (2009) 534–541. doi:10.1016/j.jpowsour.2009.02.001.
- [35] J.W. Fergus, Electrolytes for solid oxide fuel cells, *J. Power Sources.* 162 (2006) 30–40. doi:10.1016/j.jpowsour.2006.06.062.
- [36] R. Woolley, *Ruddlesden-Popper Phases as Solid Oxide Fuel Cell Cathodes : Electrochemical Performance and In Situ Characterisation*, 2014.
- [37] B.C.H. Steele, Material science and engineering : The enabling technology for the commercialisation of fuel cell systems, *J. Mater. Sci.* 6 (2001) 1053–1068.

- [38] O. Yamamoto, Solid oxide fuel cells: fundamental aspects and prospects, *Electrochim. Acta.* 45 (2000) 2423–2435. doi:10.1016/S0013-4686(00)00330-3.
- [39] B.C.H. Steele, Materials for IT-SOFC stacks - 35 years R&D: The inevitability of gradualness?, *Solid State Ionics.* 134 (2000) 3–20. doi:10.1016/S0167-2738(00)00709-8.
- [40] A.R. Genreith-Schriever, P. Hebbeker, J. Hinterberg, T. Zacherle, R.A. De Souza, Understanding Oxygen-Vacancy Migration in the Fluorite Oxide CeO₂: An Ab Initio Study of Impurity-Anion Migration, *J. Phys. Chem. C.* 119 (2015) 28269–28275. doi:10.1021/acs.jpcc.5b07813.
- [41] E. Ivers-Tiffée, A. Weber, D. Herbstritt, Materials and technologies for SOFC-components, *J. Eur. Ceram. Soc.* 21 (2001) 1805–1811. doi:10.1016/S0955-2219(01)00120-0.
- [42] L. Wang, R. Merkle, J. Maier, Surface Kinetics and Mechanism of Oxygen Incorporation Into Ba_{1-x}Sr_xCo_yFe_{1-y}O_{3-δ} SOFC Microelectrodes, *J. Electrochem. Soc.* 157 (2010) B1802. doi:10.1149/1.3494224.
- [43] R. De Souza, Oxygen transport in La_{1-x}Sr_xMn_{1-y}Co_yO_{3±δ} perovskites Part I. Oxygen tracer diffusion, *Solid State Ionics.* 106 (1998) 175–187. doi:10.1016/S0167-2738(97)00499-2.
- [44] F.M. Figueiredo, F.M.B. Marques, J.R. Frade, Electrochemical permeability of La_{1-x}Sr_xCoO_{3-δ} materials, *Solid State Ionics.* 111 (1998) 273–281. doi:10.1016/S0167-2738(98)00192-1.
- [45] H. Ullmann, N. Trofimenko, F. Tietz, D. Stöver, A. Ahmad-Khanlou, Correlation between thermal expansion and oxide ion transport in mixed conducting perovskite-type oxides for SOFC cathode, *Solid State Ionics.* 138 (2000) 12.
- [46] L. Wang, R. Merkle, J. Maier, Oxygen Reduction Kinetics and Transport Properties of (Ba,Sr)(Co,Fe)O_{3-δ}, *ECS Trans.* 25 (2009) 2497–2505. doi:10.1149/1.3205805.
- [47] R. Küngas, F. Bidrawn, E. Mahmoud, J.M. Vohs, R.J. Gorte, Evidence of surface-reaction rate limitations in SOFC composite cathodes, *Solid State Ionics.* 225 (2012) 146–150. doi:10.1016/j.ssi.2012.04.030.
- [48] C. Endler-Schuck, J. Joos, C. Niedrig, A. Weber, E. Ivers-Tiffée, The chemical oxygen surface exchange and bulk diffusion coefficient determined by impedance spectroscopy of porous La_{0.58}Sr_{0.4}Co_{0.2}Fe_{0.8}O_{3-δ} (LSCF) cathodes, *Solid State Ionics.* 269 (2015) 67–79. doi:10.1016/j.ssi.2014.11.018.
- [49] Y.X. Lu, C. Kreller, S.B. Adler, Measurement and Modeling of the Impedance Characteristics of Porous La_{1-x}Sr_xCoO_{3-δ} Electrodes, *J. Electrochem. Soc.* 156 (2009) B513–B525. doi:10.1149/1.3079337.
- [50] M.J. Jørgensen, M. Mogensen, Impedance of Solid Oxide Fuel Cell LSM/YSZ Composite Cathodes, *J. Electrochem. Soc.* 148 (2001) A433–

A442. doi:10.1149/1.1360203.

- [51] T. Kenjo, S. Osawa, K. Fujikawa, High Temperature Air Cathodes Containing Ion Conductive Oxides, *J. Electrochem. Soc.* 138 (1991) 349–355. doi:10.1149/1.2085587.
- [52] I.R. De Larramendi, N. Ortiz-Vitoriano, I.B. Dzul-Bautista, T. Rojo, Designing Perovskite Oxides for Solid Oxide Fuel Cells, in: *Perovskite Mater. - Synth. Characterisation, Prop. Appl.*, 2016. doi:10.5772/61304.
- Figures retrieved from
<https://www.intechopen.com/books/perovskite-materials-synthesis-characterisation-properties-and-applications/designing-perovskite-oxides-for-solid-oxide-fuel-cells> (accessed on 23.06.2017)
- [53] A. Aguadero, L. Fawcett, S. Taub, R. Woolley, K.T. Wu, N. Xu, J.A. Kilner, S.J. Skinner, Materials development for intermediate-temperature solid oxide electrochemical devices, *J. Mater. Sci.* 47 (2012) 3925–3948. doi:10.1007/s10853-011-6213-1.
- [54] C. Kittel, *Introduction to Solid State Physics*, 7th ed., Wiley, New York, 1996.
- [55] S.B. Adler, X.Y. Chen, J.R. Wilson, Mechanisms and rate laws for oxygen exchange on mixed-conducting oxide surfaces, *J. Catal.* 245 (2007) 91–109. doi:10.1016/j.jcat.2006.09.019.
- [56] J.A. Kilner, Fast oxygen transport in acceptor doped oxides, *Solid State Ionics.* 129 (2000) 13–23. doi:10.1016/S0167-2738(99)00313-6.
- [57] J.W. Stevenson, T.R. Armstrong, R.D. Carneim, L.R. Pederson, W.J. Weber, Electrochemical Properties of Mixed Conducting Perovskites $\text{La}_{1-x}\text{M}_x\text{Co}_{1-y}\text{Fe}_y\text{O}_{3-\delta}$ (M=Sr, Ba, Ca), *J. Electrochem. Soc.* 143 (1996) 2722–2729.
- [58] E. V. Bongio, H. Black, F.C. Raszewski, D. Edwards, C.J. Mcconville, V.R.W. Amarakoon, Microstructural and High-Temperature Electrical Characterization of $\text{La}_{1-x}\text{Sr}_x\text{FeO}_{3-\delta}$, *J. Electroceramics.* 14 (2005) 193–198. doi:10.1007/s10832-005-0957-4.
- [59] S.P. Jiang, Development of lanthanum strontium manganite perovskite cathode materials of solid oxide fuel cells: A review, 2008. doi:10.1007/s10853-008-2966-6.
- [60] M. V. Patrakeev, J.A. Bahteeva, E.B. Mitberg, I.A. Leonidov, V.L. Kozhevnikov, K.R. Poeppelmeier, Electron/hole and ion transport in $\text{La}_{1-x}\text{Sr}_x\text{FeO}_{3-\delta}$, *J. Solid State Chem.* 172 (2003) 219–231. doi:10.1016/S0022-4596(03)00040-9.
- [61] A. Petric, P. Huang, F. Tietz, Evaluation of La-Sr-Co-Fe-O perovskites for solid oxide fuel cells and gas separation membranes, *Solid State Ionics.* 135 (2000) 719–725. doi:10.1016/S0167-2738(00)00394-5.
- [62] L.W. Tai, M.M. Nasrallah, H.U. Anderson, D.M. Sparlin, S.R. Sehlin, Structure and electrical properties of $\text{La}_{1-x}\text{Sr}_x\text{Co}_{1-y}\text{Fe}_y\text{O}_3$. Part 1. The system

- La_{0.8}Sr_{0.2}Co_{1-y}Fe_yO₃, *Solid State Ionics*. 76 (1995) 259–271.
doi:10.1016/0167-2738(94)00244-M.
- [63] K. Iwasaki, T. Ito, T. Nagasaki, Y. Arita, M. Yoshino, T. Matsui, Thermoelectric properties of polycrystalline La_{1-x}Sr_xCoO₃, *J. Solid State Chem.* 181 (2008) 3145–3150. doi:10.1016/j.jssc.2008.08.017.
- [64] A. Mineshige, M. Inaba, T. Yao, Z. Ogumi, K. Kikuchi, M. Kawase, Crystal Structure and Metal–Insulator Transition of La_{1-x}Sr_xCoO_{3-δ}, *J. Solid State Chem.* 121 (1996) 423–429. doi:10.1006/jssc.1996.0058.
- [65] Y. Ji, J.A. Kilner, M.F. Carolan, Electrical properties and oxygen diffusion in yttria-stabilised zirconia (YSZ)-La_{0.8}Sr_{0.2}MnO_{3±δ} (LSM) composites, *Solid State Ionics*. 176 (2005) 937–943. doi:10.1016/j.ssi.2004.11.019.
- [66] T. Sørensen, *Nonstoichiometric Oxides*, Academic Press, New York, 1981.
- [67] Y. Teraoka, T. Nobunaga, K. Okamoto, N. Miura, N. Yamazoe, Influence of constituent metal cations in substituted LaCoO₃ on mixed conductivity and oxygen permeability, *Solid State Ionics*. 48 (1991) 207–212.
doi:10.1016/0167-2738(91)90034-9.
- [68] M.J. Gadre, Y.-L. Lee, D. Morgan, Cation interdiffusion model for enhanced oxygen kinetics at oxide heterostructure interfaces, *Phys. Chem. Chem. Phys.* 14 (2012) 2606. doi:10.1039/c2cp23033j.
- [69] M. Mogensen, D. Lybye, N. Bonanos, P. V. Hendriksen, F.W. Poulsen, Factors controlling the oxide ion conductivity of fluorite and perovskite structured oxides, *Solid State Ionics*. 174 (2004) 279–286.
doi:10.1016/j.ssi.2004.07.036.
- [70] I.H. Inoue, Electrostatic carrier doping to perovskite transition-metal oxides, *Semicond. Sci. Technol.* 20 (2005) S112–S120. doi:10.1088/0268-1242/20/4/013.
- [71] J. Richter, P. Holtappels, T. Graule, T. Nakamura, L.J. Gauckler, Materials design for perovskite SOFC cathodes, *Monatshefte Fur Chemie*. 140 (2009) 985–999. doi:10.1007/s00706-009-0153-3.
- [72] J.C. Boivin, G. Mairesse, Recent Material Developments in Fast Oxide Ion Conductors, *Chem. Mater.* 10 (1998) 2870–2888. doi:10.1021/cm980236q.
- [73] H. Yokokawa, H. Tu, B. Iwanschitz, A. Mai, Fundamental mechanisms limiting solid oxide fuel cell durability, *J. Power Sources*. 182 (2008) 400–412. doi:10.1016/j.jpowsour.2008.02.016.
- [74] G.C. Kostogloudis, G. Tsiniarakis, C. Ftikos, Chemical reactivity of perovskite oxide SOFC cathodes and yttria stabilized zirconia, *Solid State Ionics*. 135 (2000) 529–535. doi:10.1016/S0167-2738(00)00433-1.
- [75] Y. Chen, H. Téllez, M. Burriel, F. Yang, N. Tsvetkov, Z. Cai, D.W. McComb, J.A. Kilner, B. Yildiz, Segregated Chemistry and Structure on (001) and (100) Surfaces of (La_{1-x}Sr_x)₂CoO₄ Override the Crystal Anisotropy in Oxygen

- Exchange Kinetics, *Chem. Mater.* 27 (2015) 5436–5450.
doi:10.1021/acs.chemmater.5b02292.
- [76] H. Yokokawa, T. Horita, N. Sakai, K. Yamaji, M.E. Brito, Y.P. Xiong, H. Kishimoto, Thermodynamic considerations on Cr poisoning in SOFC cathodes, *Solid State Ionics*. 177 (2006) 3193–3198.
doi:10.1016/j.ssi.2006.07.055.
- [77] H. Yokokawa, N. Sakai, T. Horita, K. Yamaji, M.E. Brito, H. Kishimoto, Thermodynamic and kinetic considerations on degradations in solid oxide fuel cell cathodes, *J. Alloys Compd.* 452 (2008) 41–47.
doi:10.1016/j.jallcom.2006.12.150.
- [78] T. Tsai, S.A. Barnett, Effect of LSM-YSZ cathode on thin-electrolyte solid oxide fuel cell performance, *Solid State Ionics*. 93 (1997) 207–217.
doi:10.1016/S0167-2738(96)00524-3.
- [79] W.Z. Zhu, S.C. Deevi, Development of interconnect materials for solid oxide fuel cells, *Mater. Sci. Eng. A*. 348 (2003) 227–243. doi:10.1016/S0921-5093(02)00736-0.
- [80] S.P. Jiang, S. Zhang, Y.D. Zhen, Deposition of Cr Species at (La,Sr)(Co,Fe)O_{3-δ} Cathodes of Solid Oxide Fuel Cells, *J. Electrochem. Soc.* 153 (2006) A127. doi:10.1149/1.2136077.
- [81] K. Katsiev, B. Yildiz, B. Kavaipatti, P. Salvador, Correlations of Electronic and Chemical State on La_{0.7}Sr_{0.3}MnO₃ Dense Thin Film Cathode Surfaces, *ECS Trans.* 25 (2009) 2309–2318. doi:10.1149/1.3205782.
- [82] E.J. Crumlin, E. Mutoro, Z. Liu, M.E. Grass, M.D. Biegalski, Y.-L. Lee, D. Morgan, H.M. Christen, H. Bluhm, Y. Shao-Horn, Surface strontium enrichment on highly active perovskites for oxygen electrocatalysis in solid oxide fuel cells, *Energy & Environ. Sci.* 5 (2012) 6081.
doi:10.1039/c2ee03397f.
- [83] Y. Lu, C.R. Kreller, S.B. Adler, J.R. Wilson, S.A. Barnett, P.W. Voorhees, H.-Y. Chen, K. Thornton, Performance Variability and Degradation in Porous La_{1-x}Sr_xCoO_{3-δ} Electrodes, *J. Electrochem. Soc.* 161 (2014) F561–F568.
doi:10.1149/2.101404jes.
- [84] W. Lee, J.W. Han, Y. Chen, Z. Cai, B. Yildiz, Cation size mismatch and charge interactions drive dopant segregation at the surfaces of manganite perovskites, *J. Am. Chem. Soc.* 135 (2013) 7909–7925.
doi:10.1021/ja3125349.
- [85] D. Lee, Y.-L. Lee, W.T. Hong, M.D. Biegalski, D. Morgan, Y. Shao-Horn, Oxygen surface exchange kinetics and stability of (La,Sr)₂CoO_{4±δ}/La_{1-x}Sr_xMO_{3-δ} (M=Co and Fe) hetero-interfaces at intermediate temperatures, *J. Mater. Chem. A*. 3 (2015) 2144–2157. doi:10.1039/C4TA05795C.
- [86] Y. Orikasa, E.J. Crumlin, S. Sako, K. Amezawa, T. Uruga, M.D. Biegalski, H.M. Christen, Y. Uchimoto, Y. Shao-Horn, Surface Strontium Segregation of Solid Oxide Fuel Cell Cathodes Proved by In Situ Depth-Resolved X-ray

- Absorption Spectroscopy, *ECS Electrochem. Lett.* 3 (2014) F23–F26. doi:10.1149/2.006404eel.
- [87] N. Tsvetkov, Q. Lu, B. Yildiz, Improved electrochemical stability at the surface of $\text{La}_{0.8}\text{Sr}_{0.2}\text{CoO}_{3-\delta}$ achieved by surface chemical modification, *Faraday Discuss.* 182 (2015) 257–269. doi:10.1039/C5FD00023H.
- [88] Z. Feng, Y. Yacoby, M.J. Gadre, Y. Lee, W.T. Hong, H. Zhou, M.D. Biegalski, H.M. Christen, S.B. Adler, D. Morgan, Y. Shao-Horn, Anomalous Interface and Surface Strontium Segregation in $(\text{La}_{1-y}\text{Sr}_y)_2\text{CoO}_{4\pm\delta}/\text{La}_{1-x}\text{Sr}_x\text{CoO}_{3-\delta}$ Heterostructured Thin Films, *J. Phys. Chem. Lett.* 5 (2014) 1027–1034. doi:10.1021/jz500293d.
- [89] F. Tietz, *Thermal Expansion of SOFC Materials*, 5 (1999) 129–139.
- [90] A. Weber, E. Ivers-Tiffée, Materials and concepts for solid oxide fuel cells (SOFCs) in stationary and mobile applications, *J. Power Sources.* 127 (2004) 273–283. doi:10.1016/j.jpowsour.2003.09.024.
- [91] F. Tietz, I. Arul Raj, M. Zahid, D. Stöver, Electrical conductivity and thermal expansion of $\text{La}_{0.8}\text{Sr}_{0.2}(\text{Mn},\text{Fe},\text{Co})\text{O}_{3-\delta}$ perovskites, *Solid State Ionics.* 177 (2006) 1753–1756. doi:10.1016/j.ssi.2005.12.017.
- [92] S.R. Tai, L. W., Nasrallah, M. M., Anderson, H. U., Sparlin, D. M. and Sehlin, Structure and electrical properties of $\text{La}_{1-x}\text{Sr}_x\text{Co}_{1-y}\text{Fe}_y\text{O}_3$. Part 1 . The system $\text{La}_{0.8}\text{Sr}_{0.2}\text{Co}_{1-y}\text{Fe}_y\text{O}_3$, 76 (1995). doi:10.1016/0167-2738(94)00244-M.
- [93] H. Lv, Y.J. Wu, B. Huang, B.Y. Zhao, K.A. Hu, Structure and electrochemical properties of $\text{Sm}_{0.5}\text{Sr}_{0.5}\text{Co}_{1-x}\text{Fe}_x\text{O}_{3-\delta}$ cathodes for solid oxide fuel cells, *Solid State Ionics.* 177 (2006) 901–906. doi:10.1016/j.ssi.2006.01.038.
- [94] S.P. Simner, J.F. Bonnett, N.L. Canfield, K.D. Meinhardt, V.L. Sprenkle, J.W. Stevenson, Optimized Lanthanum Ferrite-Based Cathodes for Anode-Supported SOFCs, *Electrochem. Solid-State Lett.* 5 (2002) A173. doi:10.1149/1.1483156.
- [95] A. Berenov, A. Atkinson, H. Wood, Evaluation of $\text{La}_{0.8}\text{Sr}_{0.2}\text{Cu}_{1-x}\text{Mn}_x\text{O}_d$ double Perovskite for Use in SOFCs, in: *ECS Trans.*, 2007: pp. 1173–1181. doi:10.1149/1.2729216.
- [96] J. Mizusaki, Electronic conductivity, Seebeck coefficient, defect and electronic structure of nonstoichiometric $\text{La}_{1-x}\text{Sr}_x\text{MnO}_{3-\delta}$, *Solid State Ionics.* 132 (2000) 167–180. doi:10.1016/S0167-2738(00)00662-7.
- [97] S. Bishop, Chemical expansion of solid oxide fuel cell materials: A brief overview, *Acta Mech. Sin.* 29 (2013) 312–317. doi:10.1007/s10409-013-0045-y.
- [98] R.D. Shannon, Revised effective ionic radii and systematic studies of interatomic distances in halides and chalcogenides, *Acta Crystallogr. Sect. A.* 32 (1976) 751–767. doi:10.1107/S0567739476001551.

- [99] X. Chen, J. Yu, S.B. Adler, Thermal and Chemical Expansion of Sr-Doped Lanthanum Cobalt Oxide ($\text{La}_{1-x}\text{Sr}_x\text{CoO}_{3-\delta}$), *Chem. Mater.* 17 (2005) 4537–4546. doi:10.1021/cm050905h.
- [100] L. Vasylechko, V. Vashook, D. Savytskii, A. Senyshyn, R. Niewa, M. Knapp, H. Ullmann, M. Berkowski, A. Matkovskii, U. Bismayer, Crystal structure, thermal expansion and conductivity of anisotropic $\text{La}_{1-x}\text{Sr}_x\text{Ga}_{1-2x}\text{Mg}_{2x}\text{O}_{3-\delta}$ ($x=0.05, 0.1$) single crystals, *J. Solid State Chem.* 172 (2003) 396–411. doi:10.1016/S0022-4596(03)00016-1.
- [101] H.M. Zhang, N. Yamazoe, Y. Teraoka, Effects of B site partial substitutions of perovskite-type $\text{La}_{0.6}\text{Sr}_{0.4}\text{CoO}_3$ on oxygen desorption, *J. Mater. Sci. Lett.* 8 (1989) 995–996. doi:10.1007/BF01730464.
- [102] J. Nowotny, M. Rekas, Defect Chemistry of $(\text{La},\text{Sr})\text{MnO}_3$, *J. Am. Ceram. Soc.* 81 (1998) 67–80. doi:10.1111/j.1151-2916.1998.tb02297.x.
- [103] A. Manthiram, J.H. Kim, Y.N. Kim, K.T. Lee, Crystal chemistry and properties of mixed ionic-electronic conductors, *J. Electroceramics.* 27 (2011) 93–107. doi:10.1007/s10832-011-9635-x.
- [104] A.R. Ruffa, Thermal expansion in insulating materials, *J. Mater. Sci.* 15 (1980) 2258–2267. doi:10.1007/BF00552315.
- [105] Y. Teraoka, H.M. Zhang, K. Okamoto, N. Yamazoe, Mixed ionic-electronic conductivity of $\text{La}_{1-x}\text{Sr}_x\text{Co}_{1-y}\text{Fe}_y\text{O}_{3-\delta}$ perovskite-type oxides, *Mater. Res. Bull.* 23 (1988) 51–58. doi:10.1016/0025-5408(88)90224-3.
- [106] S.J. Skinner, Recent advances in Perovskite-type materials for solid oxide fuel cell cathodes, *Int. J. Inorg. Mater.* 3 (2001) 113–121. doi:10.1016/S1466-6049(01)00004-6.
- [107] J.H. Khou, H.U. Anderson, D.M. Sparlin, Oxidation-Reduction Defect Structure, Behavior of Undoped and Sr-Doped LaMnO_3 : Electrical Conductivity and Thermoelectric Power, *J. Solid State Chem.* 87 (1990) 55–63. doi:10.1016/0022-4596(90)90064-5.
- [108] M. Petitjean, G. Caboche, E. Siebert, L. Dessemond, L.C. Dufour, $(\text{La}_{0.8}\text{Sr}_{0.2})(\text{Mn}_{1-y}\text{Fe}_y)\text{O}_{3\pm\delta}$ oxides for ITSOFC cathode materials? Electrical and ionic transport properties, *J. Eur. Ceram. Soc.* 25 (2005) 2651–2654. doi:10.1016/j.jeurceramsoc.2005.03.117.
- [109] J. Mizusaki, T. Matsuura, S. Yamauchi, K. Fueki, J. Tabuchi, Electrical conductivity and Seebeck coefficient of nonstoichiometric $\text{La}_{1-x}\text{Sr}_x\text{CoO}_{3-\delta}$, *J. Electrochem. Soc.* 136 (1989) 2082–2088. doi:10.1149/1.2097187.
- [110] I. Yasuda, K. Ogasawara, M. Hishinuma, T. Kawada, M. Dokiya, Oxygen tracer diffusion coefficient of $(\text{La}, \text{Sr})\text{MnO}_{3\pm\delta}$, *Solid State Ionics.* 86–88 (1996) 1197–1201. doi:10.1016/0167-2738(96)00287-1.
- [111] J. Mizusaki, H. Tagawa, K. Naraya, T. Sasamoto, Nonstoichiometry and thermochemical stability of the perovskite-type $\text{La}_{1-x}\text{Sr}_x\text{MnO}_{3-\delta}$, *Solid State Ionics.* 49 (1991) 111–118. doi:10.1016/0167-2738(91)90076-N.

- [112] J. Mizusaki, Nonstoichiometry, diffusion, and electrical properties of perovskite-type oxide electrode materials, *Solid State Ionics*. 52 (1992) 79–91. doi:10.1016/0167-2738(92)90093-5.
- [113] K. Hassmann, SOFC Power Plants, the Siemens-Westinghouse Approach, *Fuel Cells*. 1 (2001) 78–84. doi:10.1002/1615-6854(200105)1:1<78::AID-FUCE78>3.0.CO;2-Q.
- [114] M.C. Williams, J.P. Strakey, S.C. Singhal, U.S. distributed generation fuel cell program, *J. Power Sources*. 131 (2004) 79–85. doi:10.1016/j.jpowsour.2004.01.021.
- [115] P. Hjalmarrsson, M. Søgaaard, M. Mogensen, Defect structure, electronic conductivity and expansion of properties of $(\text{La}_{1-x}\text{Sr}_x)_s\text{Co}_{1-y}\text{Ni}_y\text{O}_{3-\delta}$, *J. Solid State Chem*. 183 (2010) 1853–1862. doi:10.1016/j.jssc.2010.04.044.
- [116] H.Y. Lee, K. Huang, J.B. Goodenough, Sr- and Ni-Doped LaCoO_3 and LaFeO_3 Perovskites, *J. Electrochem. Soc.* 145 (1998) 3220–3227. doi:10.1149/1.1838789.
- [117] J.-S. Zhou, J.B. Goodenough, A. Asamitsu, Y. Tokura, Pressure-Induced Polaronic to Itinerant Electronic Transition in $\text{La}_{1-x}\text{SrxMnO}_{3-\delta}$ Crystals, *Phys. Rev. Lett.* 79 (1997) 3234–3237. doi:10.1103/PhysRevLett.79.3234.
- [118] M.A. Señaris-Rodríguez, J.B. Goodenough, Magnetic and Transport Properties of the System $\text{La}_{1-x}\text{Sr}_x\text{CoO}_{3-\delta}$ ($0 < x \leq 0.50$), *J. Solid State Chem*. 118 (1995) 323–336. doi:10.1006/jssc.1995.1351.
- [119] L. Dieterle, P. Bockstaller, D. Gerthsen, J. Hayd, E. Ivers-Tiffée, U. Guntow, Microstructure of Nanoscaled $\text{La}_{0.6}\text{Sr}_{0.4}\text{CoO}_{3-\delta}$ Cathodes for Intermediate-Temperature Solid Oxide Fuel Cells, *Adv. Energy Mater.* 1 (2011) 249–258. doi:10.1002/aenm.201000036.
- [120] J. Hayd, L. Dieterle, U. Guntow, D. Gerthsen, E. Ivers-Tiffée, Nanoscaled $\text{La}_{0.6}\text{Sr}_{0.4}\text{CoO}_{3-\delta}$ as intermediate temperature solid oxide fuel cell cathode: Microstructure and electrochemical performance, *J. Power Sources*. 196 (2011) 7263–7270. doi:10.1016/j.jpowsour.2010.11.147.
- [121] J. Hayd, U. Guntow, E. Ivers-Tiffée, Electrochemical Performance of nano scaled $\text{La}_{0.6}\text{Sr}_{0.4}\text{CoO}_{3-\delta}$ as intermediate temperature SOFC cathode, *ECS Trans.* 28 (2010) 3–15. doi:10.1149/1.3495829.
- [122] J. Hayd, H. Yokokawa, E. Ivers-Tiffée, Hetero-Interfaces at Nanoscaled $(\text{La,Sr})\text{CoO}_{3-\delta}$ Thin-Film Cathodes Enhancing Oxygen Surface-Exchange Properties, *J. Electrochem. Soc.* 160 (2013) F351–F359. doi:10.1149/2.017304jes.
- [123] A. Leonide, B. Rürger, A. Weber, W.A. Meulenber, E. Ivers-Tiffée, Impedance Study of Alternative $(\text{La,Sr})\text{FeO}_{3-\delta}$ and $(\text{La,Sr})(\text{Co,Fe})\text{O}_{3-\delta}$ MIEC Cathode Compositions, *J. Electrochem. Soc.* 157 (2010) B234–B239. doi:10.1149/1.3265473.
- [124] J.M. Ralph, C. Rossignol, R. Kumar, Cathode Materials for Reduced-

Temperature SOFCs, *J. Electrochem. Soc.* 150 (2003) A1518.
doi:10.1149/1.1617300.

- [125] S.P. Simner, J.F. Bonnett, N.L. Canfield, K.D. Meinhardt, J.P. Shelton, V.L. Sprenkle, J.W. Stevenson, Development of lanthanum ferrite SOFC cathodes, *J. Power Sources*. 113 (2003) 1–10. doi:10.1016/S0378-7753(02)00455-X.
- [126] U.F. Vogt, P. Holtappels, J. Sfeir, J. Richter, S. Duval, D. Wiedenmann, A. Züttel, Influence of A-site variation and B-site substitution on the physical properties of (La,Sr)FeO₃ based perovskites, *Fuel Cells*. 9 (2009) 899–906. doi:10.1002/fuce.200800116.
- [127] S.P. Simner, J.P. Shelton, M.D. Anderson, J.W. Stevenson, Interaction between La(Sr)FeO₃ SOFC cathode and YSZ electrolyte, *Solid State Ionics*. 161 (2003) 11–18. doi:10.1016/S0167-2738(03)00158-9.
- [128] W. Wang, M.D. Gross, J.M. Vohs, R.J. Gorte, The Stability of LSF-YSZ Electrodes Prepared by Infiltration, *J. Electrochem. Soc.* 154 (2007) B439. doi:10.1149/1.2709510.
- [129] M.D. Anderson, J.W. Stevenson, S.P. Simner, Reactivity of lanthanide ferrite SOFC cathodes with YSZ electrolyte, *J. Power Sources*. 129 (2004) 188–192. doi:10.1016/j.jpowsour.2003.11.039.
- [130] A. Martinez-Amesti, A. Larranaga, L.M. Rodriguez-Martinez, A.T. Aguayo, J.L. Pizarro, M.L. No, A. Laresgoiti, M.I. Arriortua, Reactivity between La(Sr)FeO₃ cathode, doped CeO₂ interlayer and yttria-stabilized zirconia electrolyte for solid oxide fuel cell applications, *J. Power Sources*. 185 (2008) 401–410. doi:10.1016/j.jpowsour.2008.06.049.
- [131] T. Horita, Y. Xiong, H. Kishimoto, K. Yamaji, M.E. Brito, H. Yokokawa, Chromium Poisoning and Degradation at (La,Sr)MnO_{3-δ} and (La,Sr)FeO_{3-δ} Cathodes for Solid Oxide Fuel Cells, *J. Electrochem. Soc.* 157 (2010) B614. doi:10.1149/1.3322103.
- [132] L.W. Tai, M.M. Nasrallah, H.U. Anderson, D.M. Sparlin, S.R. Sehlin, Structure and electrical properties of La_{1-x}Sr_xCo_{1-y}Fe_yO₃. Part 2. The system La_{1-x}Sr_xCo_{0.2}Fe_{0.8}O₃, *Solid State Ionics*. 76 (1995) 273–283. doi:10.1016/0167-2738(94)00245-N.
- [133] F.S. Baumann, J. Fleig, H.U. Habermeier, J. Maier, Impedance spectroscopic study on well-defined (La,Sr)(Co,Fe)O_{3-δ} model electrodes, *Solid State Ionics*. 177 (2006) 1071–1081. doi:10.1016/j.ssi.2006.02.045.
- [134] N.J. Simrick, A. Bieberle-Hütter, T.M. Ryll, J.A. Kilner, A. Atkinson, J.L.M. Rupp, An investigation of the oxygen reduction reaction mechanism of La_{0.6}Sr_{0.4}Co_{0.2}Fe_{0.8}O₃ using patterned thin films, *Solid State Ionics*. 206 (2012) 7–16. doi:10.1016/j.ssi.2011.10.029.

Figure retrieved from

http://www.electrochem.mat.ethz.ch/publications/paper_31 (accessed on 23.06.2017)

- [135] H. Xiong, B.K. Lai, A.C. Johnson, S. Ramanathan, Low-temperature electrochemical characterization of dense ultra-thin lanthanum strontium cobalt ferrite ($\text{La}_{0.6}\text{Sr}_{0.4}\text{Co}_{0.8}\text{Fe}_{0.2}\text{O}_3$) cathodes synthesized by RF-sputtering on nanoporous alumina-supported Y-doped zirconia membranes, *J. Power Sources*. 193 (2009) 589–592. doi:10.1016/j.jpowsour.2009.04.024.
- [136] D. Marinha, J. Hayd, L. Dessemond, E. Ivers-Tiffée, E. Djurado, Performance of $(\text{La,Sr})(\text{Co,Fe})\text{O}_{3-\delta}$ double-layer cathode films for intermediate temperature solid oxide fuel cell, *J. Power Sources*. 196 (2011) 5084–5090. doi:10.1016/j.jpowsour.2011.01.063.
- [137] H. Ding, A. V. Virkar, M. Liu, F. Liu, Suppression of Sr surface segregation in $\text{La}_{1-x}\text{Sr}_x\text{Co}_{1-y}\text{Fe}_y\text{O}_{3-\delta}$: A first principles study, *Phys Chem Chem Phys*. 15 (2013) 489–496. doi:10.1039/c2cp43148c.
- [138] F.S. Baumann, J. Fleig, H. Habermeier, J. Maier, $\text{Ba}_{0.5}\text{Sr}_{0.5}\text{Co}_{0.8}\text{Fe}_{0.2}\text{O}_{3-\delta}$ thin film microelectrodes investigated by impedance spectroscopy, *Solid State Ionics*. 177 (2006) 3187–3191. doi:10.1016/j.ssi.2006.07.057.
- [139] Z. Shao, S.M. Haile, A high-performance cathode for the next generation of solid-oxide fuel cells, *Nature*. 431 (2004) 170–173. doi:10.1038/nature02863.
- [140] L. Wang, R. Merkle, J. Maier, T. Acartürk, U. Starke, Oxygen tracer diffusion in dense $(\text{Ba}_{0.5}\text{Sr}_{0.5})(\text{Co}_{0.8}\text{Fe}_{0.2})\text{O}_{3-\delta}$ films, *Appl. Phys. Lett.* 94 (2009) 2012–2015. doi:10.1063/1.3085969.
- [141] Y. He, L. Fan, M. Afzal, M. Singh, W. Zhang, Y. Zhao, J. Li, B. Zhu, Cobalt oxides coated commercial $\text{Ba}_{0.5}\text{Sr}_{0.5}\text{Co}_{0.8}\text{Fe}_{0.2}\text{O}_{3-\delta}$ as high performance cathode for low-temperature SOFCs, *Electrochim. Acta*. 191 (2016) 223–229. doi:10.1016/j.electacta.2016.01.090.
- [142] A. Yan, V. Maragou, A. Arico, M. Cheng, P. Tsiakaras, Investigation of a $\text{Ba}_{0.5}\text{Sr}_{0.5}\text{Co}_{0.8}\text{Fe}_{0.2}\text{O}_{3-\delta}$ based cathode SOFC. II. The effect of CO_2 on the chemical stability, *Appl. Catal. B Environ.* 76 (2007) 320–327. doi:10.1016/j.apcatb.2007.06.010.
- [143] Y.H. Lim, J. Lee, J.S. Yoon, C.E. Kim, H.J. Hwang, electrochemical performance of $\text{Ba}_{0.4}\text{Sr}_{0.5}\text{Co}_x\text{Fe}_{1-x}\text{O}_{3-\delta}$ ($x=0.2-0.8$) cathode on a ScSZ electrolyte for intermediate temperature SOFCs, *J. Power Sources*. 171 (2007) 79–85. doi:10.1016/j.jpowsour.2007.05.050.
- [144] S. Švarcová, K. Wiik, J. Tolchard, H.J.M. Bouwmeester, T. Grande, Structural instability of cubic perovskite $\text{Ba}_x\text{Sr}_{1-x}\text{Co}_{1-y}\text{Fe}_y\text{O}_{3-\delta}$, *Solid State Ionics*. 178 (2008) 1787–1791. doi:10.1016/j.ssi.2007.11.031.
- [145] A. Kushima, D. Parfitt, A. Chroneos, B. Yildiz, J.A. Kilner, R.W. Grimes, Interstitialcy diffusion of oxygen in tetragonal $\text{La}_2\text{CoO}_{4+\delta}$, *Phys. Chem. Chem. Phys.* 13 (2011) 2242–2249. doi:10.1039/C0CP01603A.
- [146] A. Tarancón, M. Burriel, J. Santiso, S.J. Skinner, J.A. Kilner, Advances in layered oxide cathodes for intermediate temperature solid oxide fuel cells, *J. Mater. Chem.* 20 (2010) 3799–3813. doi:10.1039/B922430K.

- [147] C. Munnings, S. Skinner, G. Amow, P. Whitfield, I. Davidson, Oxygen transport in the $\text{La}_2\text{Ni}_{1-x}\text{Co}_x\text{O}_{4+\delta}$ system, *Solid State Ionics*. 176 (2005) 1895–1901. doi:10.1016/j.ssi.2005.06.002.
- [148] T. Matsuura, J. Tabuchi, J. Mizusaki, S. Yamauchi, K. Fueki, Electrical properties of $\text{La}_{2-x}\text{Sr}_x\text{CoO}_{4-1}$: Structure, electrical conductivity, and Seebeck coefficient of single crystals ($x=0.0, 0.5, 1.0$ and 1.5), *J. Phys. Chem. Solids*. 49 (1988) 1403–1408. doi:10.1016/0022-3697(88)90112-6.
- [149] C. Tealdi, C. Ferrara, L. Malavasi, P. Mustarelli, C. Ritter, G. Chiodelli, Y.A. Diaz-Fernandez, High-temperature neutron diffraction study of $\text{La}_2\text{Sr}_{2-x}\text{CoO}_4$: Correlation between structure and transport properties, *Phys. Rev. B*. 82 (2010) 174118. doi:10.1103/PhysRevB.82.174118.
- [150] M. Al Daroukh, V. V. Vashook, H. Ullmann, F. Tietz, I. Arual Raj, Oxides of the AMO_3 and A_2MO_4 -type: Structural stability, electrical conductivity and thermal expansion, *Solid State Ionics*. 158 (2003) 141–150. doi:10.1016/S0167-2738(02)00773-7.
- [151] J.W. Han, B. Yildiz, Mechanism for enhanced oxygen reduction kinetics at the $(\text{La,Sr})\text{CoO}_{3-\delta}/(\text{La,Sr})_2\text{CoO}_{4+\delta}$ hetero-interface, *Energy Environ. Sci.* 5 (2012) 8598. doi:10.1039/c2ee03592h.
- [152] V. V. Vashook, H. Ullmann, O.P. Olshevskaya, V.P. Kulik, V.E. Lukashevich, L. V. Kokhanovskij, Composition and electrical conductivity of some cobaltates of the type $\text{La}_{2-x}\text{Sr}_x\text{CoO}_{4.5-x/2+\delta}$, *Solid State Ionics*. 138 (2000) 99–104. doi:10.1016/S0167-2738(00)00774-8.
- [153] M. Burriel, G. Garcia, J. Santiso, J.A. Kilner, R.J. Chater, S.J. Skinner, Anisotropic oxygen diffusion properties in epitaxial thin films of $\text{La}_2\text{NiO}_{4+\delta}$, *J. Mater. Chem.* 18 (2008) 416–422. doi:10.1039/b711341b.
- [154] J. Bassat, Anisotropic ionic transport properties in $\text{La}_2\text{NiO}_{4+\delta}$ single crystals, *Solid State Ionics*. 167 (2004) 341–347. doi:10.1016/j.ssi.2003.12.012.
- [155] Y. Hu, Y. Bouffanais, L. Almar, A. Morata, A. Tarancon, G. Dezaneeu, $\text{La}_{2-x}\text{Sr}_x\text{CoO}_{4-\delta}$ ($x=0.9, 1.0, 1.1$) Ruddlesden-Popper-type layered cobaltites as cathode materials for IT-SOFC application, *Int. J. Hydrogen Energy*. 38 (2013) 3064–3072. doi:10.1016/j.ijhydene.2012.12.047.
- [156] C. Laberty, F. Zhao, K.E. Swider-Lyons, A. V. Virkar, High-Performance Solid Oxide Fuel Cell Cathodes with Lanthanum-Nickelate-Based Composites, *Electrochem. Solid-State Lett.* 10 (2007) B170. doi:10.1149/1.2760188.
- [157] F. Mauvy, C. Lalanne, J.-M. Bassat, J.-C. Grenier, H. Zhao, L. Huo, P. Stevens, Electrode properties of $\text{Ln}_2\text{NiO}_{4+\delta}$ ($\text{Ln}=\text{La, Nd, Pr}$), *J. Electrochem. Soc.* 153 (2006) A1547. doi:10.1149/1.2207059.
- [158] N. Tsvetkov, Q. Lu, Y. Chen, B. Yildiz, Accelerated oxygen exchange kinetics on $\text{Nd}_2\text{NiO}_{4+\delta}$ thin films with tensile strain along c-axis., *ACS Nano*. 9 (2015) 1613–21. doi:10.1021/nm506279h.

- [159] C. Tealdi, C. Ferrara, P. Mustarelli, M.S. Islam, Vacancy and interstitial oxide ion migration in heavily doped $\text{La}_{2-x}\text{Sr}_x\text{CoO}_{4\pm\delta}$, *J. Mater. Chem.* 22 (2012) 8969. doi:10.1039/c2jm30769c.
- [160] T. Nitadori, M. Muramatsu, M. Misono, Valence control, reactivity of oxygen, and catalytic activity of $\text{La}_{2-x}\text{Sr}_x\text{CoO}_4$, *Chem. Mater.* 1 (1989) 215–220. doi:10.1021/cm00002a010.
- [161] J. Nielsen, J. Hjelm, Impedance of SOFC electrodes: A review and a comprehensive case study on the impedance of LSM:YSZ cathodes, *Electrochim. Acta.* 115 (2014) 31–45. doi:10.1016/j.electacta.2013.10.053.
- [162] Y. Ren, R. Küngas, R.J. Gorte, C. Deng, The effect of A-site cation (Ln=La, Pr, Sm) on the crystal structure, conductivity and oxygen reduction properties of Sr-doped ferrite perovskites, *Solid State Ionics.* 212 (2012) 47–54. doi:10.1016/j.ssi.2012.02.028.
- [163] X. Zhou, J.W. Templeton, Z. Nie, H. Chen, J.W. Stevenson, L.R. Pederson, Electrochemical performance and stability of the cathode for solid oxide fuel cells: V. High performance and stable Pr_2NiO_4 as the cathode for solid oxide fuel cells, *Electrochim. Acta.* 71 (2012) 44–49. doi:10.1016/j.electacta.2012.03.067.
- [164] D. Chen, C. Chen, F. Dong, Z. Shao, F. Ciucci, Cobalt-free polycrystalline $\text{Ba}_{0.95}\text{La}_{0.05}\text{FeO}_{3-\delta}$ thin films as cathodes for intermediate-temperature solid oxide fuel cells, *J. Power Sources.* 250 (2014) 188–195. doi:10.1016/j.jpowsour.2013.11.010.
- [165] A. Wedig, R. Merkle, J. Maier, Oxygen Exchange Kinetics of $(\text{Bi,Sr})(\text{Co,Fe})\text{O}_{3-\delta}$ Thin-Film Microelectrodes, *J. Electrochem. Soc.* 161 (2013) F23–F32. doi:10.1149/2.017401jes.
- [166] K. Yashiro, T. Nakamura, M. Sase, F. Hermes, K. Sato, T. Kawada, J. Mizusaki, Composite Cathode of Perovskite-Related Oxides, $(\text{La,Sr})\text{CoO}_{3-\delta}/(\text{La,Sr})_2\text{CoO}_{4-\delta}$, for Solid Oxide Fuel Cells, *Electrochem. Solid-State Lett.* 12 (2009) B135. doi:10.1149/1.3170903.
- [167] Y. Chen, Z. Cai, Y. Kuru, W. Ma, H.L. Tuller, B. Yildiz, Electronic activation of cathode superlattices at elevated temperatures—source of markedly accelerated oxygen reduction kinetics, *Adv. Energy Mater.* 3 (2013) 1221–1229. doi:10.1002/aenm.201300025.
- [168] Y. Kuru, H. Jalili, Z. Cai, B. Yildiz, H.L. Tuller, Direct probing of nanodimensioned oxide multilayers with the aid of focused ion beam milling, *Adv. Mater.* 23 (2011) 4543–4548. doi:10.1002/adma.201102401.
- [169] Y. Chen, Z. Cai, Y. Kuru, H.L. Tuller, B. Yildiz, Electronic Activation at Oxide Hetero-Structure at Elevated Temperatures – Source of Markedly Accelerated Oxygen Reduction Kinetics, *ECS Trans.* 57 (2013) 1781–1791. doi:10.1149/05701.1781ecst.

Figures retrieved from

http://web.mit.edu/yildizgroup/LEI/assets/pdfs/yan_ecst_2013.pdf (accessed

on 23.06.2017)

- [170] J.D. Verhoeven, *Fundamentals of Physical Metallurgy*, Wiley, New York, 1975.
- [171] J. Fleig, J. Maier, The polarization of mixed conducting SOFC cathodes: Effects of surface reaction coefficient, ionic conductivity and geometry, *J. Eur. Ceram. Soc.* 24 (2004) 1343–1347. doi:10.1016/S0955-2219(03)00561-2.
- [172] E. Borsoukov, J.R. Macdonald, *Impedance Spectroscopy, Theory, Experiment, Application*, John Wiley & Sons, NJ, 2005.
- [173] R. Merkle, J. Maier, How is oxygen incorporated into oxides? A comprehensive kinetic study of a simple solid-state reaction with SrTiO₃ as a model material, *Angew. Chemie - Int. Ed.* 47 (2008) 3874–3894. doi:10.1002/anie.200700987.
- [174] P.H. Bottelberghs, G.H.J. Broers, Interfacial impedance behaviour of polished and paint platinum electrodes at Na₂WO₄-Na₂MoO₄ solid electrolytes, *J. Electroanal. Chem.* 67 (1976) 155–167. doi:10.1016/S0022-0728(76)80332-4.
- [175] A. Le Mehaute, G. Crepy, Introduction to transfer and motion in fractal media: The geometry of kinetics, *Solid State Ionics.* 9–10 (1983) 17–30. doi:10.1016/0167-2738(83)90207-2.
- [176] B.A. Boukamp, H.J.M. Bouwmeester, Interpretation of the Gerischer impedance in solid state ionics, *Solid State Ionics.* 157 (2003) 29–33. doi:10.1016/S0167-2738(02)00185-6.
- [177] M. Kubicek, T.M. Huber, A. Welzl, A. Penn, G.M. Rupp, J. Bernardi, M. Stöger-pollach, H. Hutter, J. Fleig, Electrochemical properties of La_{0.6}Sr_{0.4}CoO_{3-δ} thin films investigated by complementary impedance spectroscopy and isotope exchange depth profiling, *Solid State Ionics.* 256 (2014) 38–44. doi:10.1016/j.ssi.2013.12.016.
- [178] C.R. Kreller, T.J. McDonald, S.B. Adler, E.J. Crumlin, E. Mutoro, S.J. Ahn, G.J. la O', Y. Shao-Horn, M.D. Biegalski, H.M. Christen, R.R. Chater, J.A. Kilner, Origin of Enhanced Chemical Capacitance in La_{0.8}Sr_{0.2}CoO_{3-δ} Thin Film Electrodes, *J. Electrochem. Soc.* 160 (2013) F931–F942. doi:10.1149/2.021309jes.
- [179] J.B. Allen, L.R. Faulkner, *Electrochemical Methods: Fundamentals and Applications*, Wiley, New York, 2001.
- [180] S.B. Adler, Limitations of charge-transfer models for mixed-conducting oxygen electrodes, *Solid State Ionics.* 135 (2000) 603–612. doi:10.1016/S0167-2738(00)00423-9.

Figure retrieved from

https://www.researchgate.net/publication/222872496_A_review_of_AC_impedance_modeling_and_validation_in_SOFC_diagnosis/figures (accessed on 23.06.2017)

- [181] M. Sase, J. Suzuki, K. Yashiro, T. Otake, A. Kaimai, T. Kawada, J. Mizusaki, H. Yugami, Electrode reaction and microstructure of $\text{La}_{0.6}\text{Sr}_{0.4}\text{CoO}_{3-\delta}$ thin films, *Solid State Ionics*. 177 (2006) 1961–1964. doi:10.1016/j.ssi.2006.01.018.
- [182] S.B. Adler, Mechanism and kinetics of oxygen reduction on porous $\text{La}_{1-x}\text{Sr}_x\text{CoO}_{3-\delta}$ electrodes, *Solid State Ionics*. 111 (1998) 125–134. doi:10.1016/S0167-2738(98)00179-9.
- [183] S.B. Adler, J.A. Lane, B.C.H. Steele, Electrode Kinetics of Porous Mixed-Conducting Oxygen Electrodes, *J. Electrochem. Soc.* 143 (1996) 3554. doi:10.1149/1.1837252.
- [184] T.J. McDonald, S.B. Adler, (Invited) Theory and Application of Nonlinear Electrochemical Impedance Spectroscopy, *ECS Trans.* 45 (2012) 429–439. doi:10.1149/1.3701334.
- [185] V. V. Sikolenko, E. V. Pomjakushina, S.Y. Istomin, Neutron diffraction studies of $\text{La}_{(1-x)}\text{Sr}_{(x)}\text{CoO}_3$ magnetic structure at $x=0.15$ and 0.3 , *J. Magn. Magn. Mater.* 258–259 (2003) 300–301. doi:10.1016/S0304-8853(02)01145-9.
- [186] M. Sánchez-Andújar, M.A. Señaris-Rodríguez, Synthesis, structure and microstructure of the layered compounds $\text{Ln}_{1-x}\text{Sr}_{1+x}\text{CoO}_4$ (Ln: La, Nd and Gd), *Solid State Sci.* 6 (2004) 21–27. doi:10.1016/j.solidstatesciences.2003.11.005.
- [187] G. Brauer, H. Gradinger, Über Heterotype Mischphasen Bei Seltenerdoxyden.I, *Zeitschrift Fur Anorg. Und Allg. Chemie.* 276 (1954) 209–226. doi:10.1002/zaac.19542760502.
- [188] L. Alexander, H.P. Klug, Determination of crystallite size with the x-ray spectrometer, *J. Appl. Phys.* 21 (1950) 137–142. doi:10.1063/1.1699612.
- [189] O. Demircan, Electrochemical Oxidation Kinetics of Hydrogen and Higher Hydrocarbon Fuels on Solid Oxide Fuel Cells, University of Maryland, 2007.
- [190] A.N. Petrov, O.F. Kononchuk, A. V. Andreev, V.A. Cherepanov, P. Kofstad, Crystal structure, electrical and magnetic properties of $\text{La}_{1-x}\text{Sr}_x\text{CoO}_{3-\delta}$, *Solid State Ionics*. 80 (1995) 189–199. doi:10.1016/0167-2738(95)00114-L.
- [191] H. Taguchi, K. Matsu-Ura, M. Takada, K. Hirota, Effect of the A-site cation on methane oxidation of perovskite-type $(\text{La}_{1-x}\text{M}_x)\text{CoO}_3$ (M=Ca, Sr, and Ba), *J. Solid State Chem.* 190 (2012) 157–161. doi:10.1016/j.jssc.2012.02.023.
- [192] Y. Ohno, S. Nagata, H. Sato, Properties of oxides for high temperature solid electrolyte fuel cell, *Solid State Ionics*. 9–10 (1983) 1001–1007. doi:10.1016/0167-2738(83)90122-4.
- [193] A.N. Petrov, V.I. Voronin, T. Norby, P. Kofstad, Crystal Structure of the Mixed Oxides $\text{La}_{0.7}\text{Sr}_{0.3}\text{Co}_{1-z}\text{Mn}_z\text{O}_{3\pm y}$ ($0 \leq z \leq 1$), *J. Solid State Chem.* 143 (1999) 52–57. doi:10.1006/jssc.1998.8073.

- [194] V. V. Efimov, E.A. Efimova, D.I. Kochubei, V. V. Kriventsov, A. Kuz'min, V. V. Sikolenko, V.G. Simkin, I.O. Troyanchuk, S.I. Tiutiunnikov, Study of $\text{La}_{1-x}\text{Sr}_x\text{CoO}_3$ ($x=0.0-0.5$) by X-Ray Absorption Spectroscopy and High-Resolution Neutron Diffraction Methods, *Surf. X-Ray, Synchrotron Neutron Res.* 6 (2006) 23–29.
- [195] J. Mizusaki, Y. Mima, S. Yamauchi, K. Fueki, Nonstoichiometry of the perovskite-type oxides $\text{La}_{1-x}\text{Sr}_x\text{CoO}_{3-\delta}$, *J. Solid State Chem.* 80 (1989) 102–111. doi:10.1016/0022-4596(89)90036-4.
- [196] S. Wang, T. Kobayashi, M. Dokiya, T. Hashimoto, Electrical and Ionic Conductivity of Gd-Doped Ceria, *J. Electrochem. Soc.* 147 (2000) 3606. doi:10.1149/1.1393946.
- [197] D. Sarı, Z.Ç. Torunoğlu, Y.E. Kalay, T. Öztürk, Preparation of $\text{La}_{0.8}\text{Sr}_{0.2}\text{CoO}_{3-\delta}$ Sputtering Targets Using a Deformable Compaction Die, (2017). Submitted to *Ceramics International*.
- [198] D. Sarı, M.Sc. Thesis, Middle East Technical University, 2017. in preparation.
- [199] J. Fleig, F.S. Baumann, V. Brichzin, H.R. Kim, J. Jamnik, G. Cristiani, H.U. Habermeier, J. Maier, Thin film microelectrodes in SOFC electrode research, *Fuel Cells.* 6 (2006) 284–292. doi:10.1002/fuce.200500209.